

# **Nanofluidic systems for individual and contact-free electrostatic trapping of charged objects**

**Inauguraldissertation**

zur  
Erlangung der Würde eines Doktors der Philosophie  
vorgelegt der  
Philosophisch-Naturwissenschaftlichen Fakultät  
der Universität Basel

von

**Michael Adrian Gerspach**  
**aus Freiburg im Breisgau, Deutschland**

Basel, 2017

Originaldokument gespeichert auf dem Dokumentenserver der Universität Basel  
edoc.unibas.ch

Genehmigt von der Philosophisch-Naturwissenschaftlichen Fakultät  
auf Antrag von:  
Prof. Dr. Roderick Lim  
Dr. Thomas Pfohl  
Dr. Thomas Braun

Basel, den 20.06.17

Prof. Dr. Martin Spiess  
Dekan

## Abstract

Contact-free trapping of nano-objects in solution is of broad interest for many applications, such as studying of polymer dynamics, detecting molecular reactions or investigating the structure and functionality of large biomolecules, to name a few. Although several trapping methods have been developed, stable and high-throughput trapping of individual nanometer-sized objects in a straightforward manner remain challenging. A powerful method of trapping charged objects smaller than 100 nm and without any external applied power is geometry-induced electrostatic (GIE) trapping. This method is based on altering the surface topography of nanofluidic channels that are charged when exposed to water. The topographically modified surfaces result in electrostatic potential wells, in which nano-objects can be trapped from milliseconds to several days, depending on the trap specification and the buffer solution. Various trapping geometries (e.g., circular pockets and rectangular slits or grids) can be realized using state-of-the-art nanofabrication tools.

This thesis explores the development and use of nanofluidic devices for electrostatic trapping and manipulation of nano-objects, such as gold nanoparticles (Au NPs) or DNA. For imaging the Au NPs, a home built interferometric scattering (iSCAT) detection system was used. iSCAT is a label free coherent optical microscopy technique that significantly increases the signal-to-noise ratio (SNR) in comparison to other imaging methods that are based on detecting only the signal scattered by a nano-object.

In detail, using standard silicon-based GIE trapping devices, Au NPs smaller than 60 nm become difficult to detect using iSCAT microscopy. To overcome this limitation, trapping devices made from glass substrate are introduced with a new developed fabrication process. These devices allow imaging of

Au NPs with an increased contrast and SNR of an order of magnitude using iSCAT detection, enabling the detection of relatively smaller nanoparticles and thereby allowing the study of their trapping behavior.

Further, the GIE trapping method is integrated into a microfluidic system that comes with the key benefits of reduced sample volume, *in situ* change of solutions, precise control of solution delivery, and the feasibility to trap nano-objects along a gradient of e.g. salt or other reactants. Using this high-throughput screening device, the performance has been quantitatively analyzed by screening the electrostatic potential along a salt gradient using 60 nm Au NPs as probes in a single experiment. Additionally, the critical salt concentration for the stability of the colloidal dispersion could be observed. The advancement of this method sets the ground for a variety of new experiments. As an example, having the possibility to insert and flush the device with different solutions, functionalization of the nanofluidic channel walls with positively charged polyelectrolytes was achieved resulting in a reversal of the walls net charge and thus allowing the trapping of positively charged Au NPs.

One drawback that makes the development and application of GIE trapping devices made from rigid  $\text{SiO}_x$  materials difficult, is the high cost and time-consuming nanofabrication in limiting infrastructures such as cleanroom facilities. Hence, new GIE trapping devices made from the soft material polydimethylsiloxane (PDMS) are introduced that are fabricated using a high-throughput and easy handling replica molding process. Stable trapping of Au NPs down to 60 nm in diameter is demonstrated and potential depths of up to  $Q \cong 24 k_B T$  of circular pockets are experimentally observed that provide stable trapping for many days. In addition, by taking advantage of the feature that PDMS is a flexible material, the PDMS devices are elastically compressed, which results in a reduction of the device channel height and thus active tuning of trapping strengths and residence times. With this capability, extremely deep potentials of up to  $Q \sim 200 k_B T$  are achieved, providing practically permanent contact-free trapping of individual nano-objects. Furthermore, the implementation of a 3D PDMS pneumatic valve system is demonstrated, which makes the devices capable of controlling the trap stiffnesses and residence times actively as well as trapping and releasing the nano-objects.

These devices will enable high-throughput trapping of nano-objects for studying their behavior and interactions in aqueous environment. The simple and low-cost fabrication process and the fact that the chip-based devices do not need externally applied fields or an elaborate build-up will make them equally available for research and commercial applications.



# Declaration

## Self-Citations

During the course of my PhD at the University of Basel and the Paul Scherrer Institut, four manuscripts were published and one paper is in preparation. All first author papers are fully implemented in this thesis.

### Chapter 3

This chapter is an implemented copy from *Glass-based geometry-induced electrostatic trapping devices for improved scattering contrast imaging of nano-objects*, M. A. Gerspach, N. Mojarad, T. Pfohl, and Y. Ekinici, *Microelectronic Engineering* **145**, 01679317 (2015).

### Chapter 4

This chapter is an implemented copy from *Nanofluidic lab-on-a-chip trapping devices for screening electrostatics in concentration gradients*, M. A. Gerspach, N. Mojarad, D. Sharma, T. Pfohl, and Y. Ekinici, *Microelectronic Engineering* **175**, 01679317 (2017)

### Chapter 5

This chapter is an implemented copy from *Soft electrostatic trapping in nanofluidics*, M. A. Gerspach, N. Mojarad, D. Sharma, T. Pfohl and Y. Ekinici, accepted in *Microsystems & Nanoengineering*.

### Chapter 6

This chapter is a manuscript in preparation *Pneumatic nanofluidic devices for controlled manipulation and contact-free trapping of nanoparticles*, M. A. Gerspach, N. Mojarad, D. Sharma, Y. Ekinici, and T. Pfohl.

### Individual contributions

**M. A. Gerspach** performed and designed experiments, analyzed and illustrated data, wrote thesis and manuscripts and co-authored one further manuscript.

**N. Mojarad, T. Pfohl, and Y. Ekinici** assisted in experimental designs, discussed results and co-authored publications.

**D. Sharma** provided COMSOL Multiphysics simulations and co-authored publications. Further, D. Sharma wrote the manuscript *Single Positively Charged Particle Trapping in Nanofluidic Systems*, D. Sharma, M. A. Gerspach, T. Pfohl, R. Y. H. Lim, and Y. Ekinici, *Microelectronic Engineering* **175**, 01679317 (2017), performed the experiments, analyzed and illustrated data related to that manuscript.

# Contents

<b>Abstract</b>	<b>iii</b>
<b>Declaration</b>	<b>v</b>
<b>Abbreviations</b>	<b>xi</b>
<b>1. Introduction</b>	<b>1</b>
<b>2. Trapping and tracking of single nano-objects</b>	<b>7</b>
2.1. Single particles in fluids . . . . .	7
2.2. Contact-free trapping of particles and molecules in fluids . . . . .	8
2.3. Theory of geometry-induced electrostatic trapping . . . . .	13
2.3.1. Electrostatic forces by induced surface charges . . . . .	13
2.3.2. Contact-free trapping by geometry-induced electrostatic potential wells . . . . .	16
2.4. Geometry-induced electrostatic trapping - developments and applications . . . . .	20
2.5. Tracking of particles and molecules in fluids . . . . .	21
2.6. Interferometric scattering (iSCAT) detection . . . . .	23
2.7. Two-dimensional sub-diffraction localization . . . . .	25
2.8. Diffusion in a harmonic potential . . . . .	27
2.9. Influential device parameters on the trap performance . . . . .	29

<b>3. Glass-based geometry-induced electrostatic trapping devices for improved scattering contrast imaging of nano-objects</b>	<b>33</b>
3.1. Introduction . . . . .	35
3.2. Theory . . . . .	37
3.3. Material and Methods . . . . .	39
3.3.1. Experimental setup . . . . .	39
3.3.2. Fabrication of silicon-based GIE trapping devices . . . . .	39
3.3.3. Fabrication of glass-based GIE trapping devices . . . . .	40
3.3.4. Sample preparation . . . . .	41
3.4. Results and Discussion . . . . .	41
3.4.1. Contrast and SNR comparison of silicon- and glass-based nanofluidic systems. . . . .	41
3.4.2. Trapping of gold nanoparticles in glass-based GIE trapping devices . . . . .	45
3.5. Conclusion . . . . .	45
3.6. Acknowledgments . . . . .	46
<b>4. Nanofluidic lab-on-a-chip trapping devices for screening electrostatics in concentration gradients</b>	<b>47</b>
4.1. Introduction . . . . .	49
4.2. Chip design and working principle . . . . .	51
4.3. Material and Methods . . . . .	52
4.3.1. Experimental setup . . . . .	52
4.3.2. Fabrication of the GIE trapping devices integrated into a microfluidic system . . . . .	53
4.3.3. Sample preparation . . . . .	55
4.4. Results and Discussion . . . . .	56
4.4.1. Screening the ionic strength . . . . .	56
4.4.2. Effect of solution ionic strength on residence time . . . . .	57
4.4.3. Instability of the colloidal dispersion at high salt concentrations . . . . .	58
4.5. Conclusion . . . . .	59
4.6. Acknowledgments . . . . .	59
<b>5. Soft electrostatic trapping in nanofluidics</b>	<b>61</b>
5.1. Introduction . . . . .	63
5.2. Materials and Methods . . . . .	65
5.2.1. Device design . . . . .	65
5.2.2. Device fabrication . . . . .	65
5.2.3. Sample solution preparation . . . . .	68
5.2.4. Experimental procedure . . . . .	69
5.2.5. Electron microscopy imaging and sample preparation . . . . .	69
5.2.6. Optical microscopy . . . . .	70

5.3. Results . . . . .	71
5.3.1. Device fabrication . . . . .	71
5.3.2. Electrostatic potential landscape . . . . .	71
5.3.3. Tunable trapping by elastic deformation . . . . .	77
5.4. Discussion . . . . .	79
5.5. Conclusion . . . . .	80
5.6. Acknowledgments . . . . .	81
5.7. Supplementary Information . . . . .	82
5.7.1. Sagging of PDMS nanochannels . . . . .	82
5.7.2. Device fabrication . . . . .	84
5.7.3. High contrast and SNR imaging using PDMS . . . . .	87
5.7.4. Reduction of axial movement of the particle at reduced nanofluidic channel heights . . . . .	89
5.7.5. Surface zeta potential measurement of activated glass and PDMS . . . . .	90
5.7.6. Simulation of the electrostatic potentials . . . . .	91
<b>6. Pneumatic nanofluidic devices for controlled manipulation and contact- free trapping of nanoparticles</b>	<b>93</b>
<b>7. Conclusions and Outlook</b>	<b>103</b>
7.1. Conclusions and further investigations . . . . .	103
7.1.1. Higher detection contrast using glass-based GIE trap- ping devices . . . . .	103
7.1.2. Integrating GIE trapping into a microfluidic system – fast screening of trapped objects . . . . .	104
7.1.3. Exploring the geometrical limits of glass-based devices and further biological investigations . . . . .	105
7.1.4. High-throughput, low-cost and simplified fabrication using PDMS-based devices . . . . .	106
7.1.5. Direct manipulation of trapped nanoparticles . . . . .	110
7.2. Further applications and considerations . . . . .	111
7.2.1. Large-scale patterning for nanolithography . . . . .	111
7.2.2. Exploring single biomolecules . . . . .	111
7.2.3. GIE trapping devices as sensors and diagnostic tools . . . . .	114
7.2.4. Direct observation of diffusive behavior . . . . .	114
<b>Bibliography</b>	<b>117</b>
<b>A. Optical detection system</b>	<b>141</b>
A.1. Optical setup . . . . .	141
A.2. Software and performance of the system . . . . .	143
A.3. Two-dimensional sub-diffraction localization . . . . .	144

<b>B. Nanofabrication protocols</b>	<b>149</b>
B.1. Silicon wafer properties . . . . .	149
B.2. Glass wafer properties . . . . .	149
B.3. Ormostamp glass wafer properties . . . . .	149
B.4. Silicon device fabrication . . . . .	150
B.5. Glass device fabrication . . . . .	153
B.6. Ormostamp <sup>®</sup> fabrication . . . . .	156
B.7. PDMS pneumatic silicon master fabrication . . . . .	156
<b>Publications</b>	<b>157</b>
<b>Acknowledgements</b>	<b>161</b>
<b>Curriculum Vitae</b>	<b>165</b>

## Abbreviations

ABEL	anti-Brownian electrokinetic trap
ac	alternating current
AODs	acousto-optic deflectors
Au NP	gold nanoparticle
BOE	buffered oxide etch
CMOS	complementary metal-oxide-semiconductor
dc	direct current
DEP	dielectrophoresis
DI	deionized
DNA	deoxyribonucleic acid
e-beam	electron beam
EDL	electric double layer
FRAP	fluorescence recovery after photobleaching
GIE	geometry induced electrostatic
iFCS	inverse-fluorescence correlation spectroscopy
IPA	isopropyl alcohol
iSCAT	interferometric scattering detection
MIBK	methyl isobutyl ketone
MSD	mean square displacement
NA	numerical aperture
ND	neutral-density
NP	nanoparticle

OD	optical density
PAPT	planar aqueous Paul trap
PBS	phosphate buffer saline
PDMS	polydimethylsiloxane
PMMA	poly(methyl methacrylate)
PPT	planar Paul trap
PSF	point spread function
QD	quantum dot
RIE	reactive ion etching
RNA	ribonucleic acid
sCMOS	scientific complementary metal-oxide-semiconductor
SEM	scanning electron microscopy
SFD	single file diffusion
SNOM	scanning near-field optical microscopy
SNR	signal-to-noise ratio
UV	ultraviolet
WD	working distance
XFEL	X-ray free-electron laser
1D	one dimensional
2D	two dimensional
3D	three dimensional



## Introduction

In the last decades, single particle and molecule experiments gave exciting new insights into the behavior, properties, and dynamics of individual nano-objects because of their ability to directly explore the smallest elements of nature. This led to fundamental understanding of biological reactions [1–3] and protein folding kinetics [4], dynamic structural conformation changes of molecules [5, 6] and to the analysis of single particles in colloid solutions [7]. In classical ‘bulk’ experiments, the properties and dynamics of many objects are measured at once and thus result in a mean value of the property measured as an average over a large molecular ensemble. Studying the fluctuations in single molecule temporal trajectories provide dynamic and statistical information, thereby distributions of values for a given property rather than its mean value [8–10]. As a result, intermediate reaction steps and properties far away from the average (extreme cases) become visible that are often hidden or impossible to capture using conventional methods. Thus, single particle and molecule experiments are allowing the scientific community to obtain detailed information about dynamic processes, binding energies, kinetics and kinematics of objects or object-object interaction in the physical, chemical, biological, and medical sciences.

The ability to explore these underlying mechanisms was only possible by the development of a number of novel biophysical methods that can be broadly separated into two classes: one that allows visualization and detection of real-time motions of single nano-objects, the other to immobilize and manipulate them [11, 12].

The development of novel observation methods, mainly in optical microscopy [11, 13–15], made the realization of single object measurements possible in the first place. But, observing a freely diffusing object in solution is limited by the time the object remains in the excitation volume, which is often in the range of milliseconds. Many biological reactions, however, happen on the time scale of several seconds, such as protein-protein interactions [16], the folding of proteins or the translation of mRNA by ribosomes [9]. As a consequence, the ability to immobilize nano-objects in fluid environments and thus achieve longer observation times of the object of interest gained great importance in various scientific and technology fields. Several trapping methods have been invented and improved in the last years and are introduced and discussed in Chapter 2. Each method has its advantages and limitations and depending on the scientific question and application needed, parameters such as trapping time, intact or contact-free immobilization, particle sizes that could be trapped, the ability to manipulate the trapped object or not, fabrication methods and costs, and required external power should be taken into account.

This thesis explores the development, characterization, and usage of nanofluidic devices for contact-free trapping and manipulation of charged nano-objects smaller than 100 nm. The approach relies on the electrostatic repulsion of nano-objects from charged walls in nanofluidic channels, called geometry induced electrostatic (GIE) trapping [17]. In these systems, the surface of the nanochannels are topographically altered resulting in electrostatic potential wells where the particles can be trapped from milliseconds up to several hours. For characterizing the performance of the devices and to obtain the electrostatic potential landscape of the traps, gold nanoparticles (Au NPs) are used as probes and a label-free optical microscopy system for visualizing their trajectories, called interferometric scattering detection (iSCAT) [18–20]. This imaging technique is based on the interference between the scattered light of a particle and a reference beam reflected from a material interface in the trapping device. It provides significant higher signal-to-noise ratio (SNR) in comparison to other imaging methods that are based on detecting only the signal scattered by the nano-object, thus allowing the detection and tracking of nano-objects with high speed and lateral precision.

The GIE trapping technology demonstrates great potential for trapping individual objects at nanometer dimensions and thus to analyze and investigate the building blocks of biological life at the ultimate molecular level. Analyzing and studying the properties, behavior and interactions of and between individual nano-objects is of significant interest and need, and will provide new insights on basic physical phenomenon and chemical reactions. Further, since many diseases originate from molecular entities, it is important

---

to understand and detect their malfunctions for both early diagnosis and new drug discovery and development. However, the high-throughput screening of individually trapped nano-objects in solutions in a straightforward manner remains a major challenge. Current nano-object trapping methods are often limited by a single trap only or by the lack of creating strong enough restoring forces to confine the nano-object in solution. Additionally they often require an elaborate build-up, which makes them difficult to use in commercial applications.

To approach these major objectives in this thesis, new developed GIE trapping devices are introduced and their performances are quantitatively explored using Au NPs. First, current silicon-based GIE trapping devices are investigated from the detection point of view using iSCAT microscopy. In this context novel devices made from glass substrate are developed that provide significant higher contrast and SNR imaging of Au NPs of an order of magnitude compared to old silicon-based devices. These new glass-based devices thus allow the detection and studying of smaller nano-objects in solution and lead to higher tracking accuracy. Then, the GIE trapping technology is integrated into a microfluidic system for precise control of sample and analyte solutions and high-throughput screening applications. The application potential is demonstrated by applying a salt gradient in the nanofluidic trapping channels, which enables to screen and quantitatively analyze the behavior of trapped Au NPs along the gradient. The chip-based devices provide a platform for single particle and molecule studies that can be used with little effort. However, time consuming and high-end nanofabrication processes to fabricate the glass- and silicon-based devices restricts the development and use of the technology. To overcome this limitation, GIE trapping devices made from soft-lithography replica molding processes are developed for low-cost, simplified and high-throughput fabrication. Potential depths of up to  $Q \sim 200 k_B T$  are achieved using these devices, which provide strong and stable contact-free trapping of the particles over many days. Finally, a pneumatic valve system is integrated into the chip that provides manipulation of the trapped object and the trapping parameters. This system can be used in the simplest case by a conventional syringe, available in every lab and thus allows to perform single particle experiments with low expenditure.

## **Thesis outline and overview**

Chapter 2 begins with an overview and background on techniques that are used for the immobilization and manipulation of nano-objects, including their state-of-the-art applications and limitations. Then, the main functional principal of GIE trapping is explained and new developments and applications that have been achieved with this method are introduced. In the context of

tracking particles in a fluid environment, the main principle of the iSCAT detection system is described and the advantages of label-free observation are discussed and why iSCAT is a good candidate for it. Further it is described, how particles are generally tracked in two dimensions and how a localization precision far beyond the diffraction limit can be obtained. In this context, the motion of a particle in a harmonic potential is described and its correlation to the trapping strength and mean residence time is explained. The chapter is completed by a discussion of the influential parameters of a GIE trap and how they are correlated to the trapping performance.

In Chapter 3, the theory of iSCAT detection for different fluidic systems is discussed. It is explained, why Au NPs smaller than 60 nm in diameter become difficult to detect using initial silicon-based GIE trapping devices and that devices made from glass substrate should lead to the imaging of Au NPs with significant higher contrast and SNR and thus allowing higher tracking precision. To confirm this assumption, new GIE trapping devices made from glass substrate are introduced and a quantitative comparison between particles in silicon- and glass-based devices is performed. To demonstrate the functionality of the glass-based devices, stable trapping of 60 nm Au NPs is demonstrated.

In Chapter 4 it is described how the GIE trapping method can be integrated into a standard microfluidic system. The advantages of such an integrated microfluidic system are discussed, such as reduced sample volume, increased control over the sample concentration, *in situ* exchange of sample and other solutions and the ability to create solution gradients of salt, pH or other reactants. These advantages are demonstrated with the ability to screen the ionic strength over a salt gradient by quantitatively analyzing the trapping behavior of Au NPs along this gradient.

In Chapter 5 a new generation of GIE trapping devices made from the soft material polydimethylsiloxane (PDMS) is introduced. The key benefits from the fabrication point of view of these devices are discussed, such as high-throughput, low cost and simplified production procedure. Then a quantitative analysis of the trap performance of the devices is experimentally performed and compared with numerical simulations. Taking advantage of the elasticity of the material, it is demonstrated how extremely deep potentials (e.g., more than  $200 k_B T$ ) and thus long trapping times can be achieved by mechanically manipulating the nanofluidic channel heights during the experiment.

---

In Chapter 6 the integration of a multilayer 3D-pneumatic PDMS system is introduced that can be used to rapidly and precisely tune the nanofluidic channel height using air pressure. Such an implemented feature enhances the PDMS devices to an entirely and straightforward fabricated chip-based system for individual trapping and manipulation of nano-objects. Using Au NPs as probes, the manipulation of the trapping strength over two orders of magnitude is achieved by varying the pneumatic chamber pressure. Furthermore by applying a fast and dynamic change in the pressure chamber, active release and catch of the Au NPs is demonstrated.

This thesis ends with Chapter 7, a short summary, discussion and outlook of potential applications and further directions and opportunities of the GIE trapping technique.



## Trapping and tracking of single nano-objects

### 2.1. Single particles in fluids

Monitoring the motion and interactions of single nano-objects in solutions provide the ultimate sensitivity in characterizing their properties and dynamics with nanometer dimensions in natural conditions [21]. Technologies and research based on single particle and molecule experiments provide novel information in areas spanning from chemistry, physics, material science, biology, biotechnology and medical sciences [12]. These investigations offer explicit information on local dynamics, kinematics and conformational changes in molecules with nanometer precision, present inter- and intra-molecular forces or provide analysis of net charges of molecules and colloidal particles. Such single nano-object dynamics and force measurements could be used, for instance, to study the folding and unfolding of proteins [4, 22–25], the step-by-step movement of kinesin motorproteins along microtubules [26–29], the DNA transcription by RNA polymerase [1, 30, 31], conformation changes in proteins [5, 32, 33], the analysis of net charges of biomolecules [34] or gold particles [7], binding kinetics of proteins [35–37], or the motion [38] and orientation [20, 39] of virus particles, to name a few.

Performing single particle and molecule experiments require experimental designs that allow the visualization of individual objects in the observation volume. This can be either achieved by performing experiments at very low concentrations of the objects of interest or by reducing the volume of the

reaction chamber so that only one or a few objects are in the observed volume. Nanofluidics, defined as the study in fluids of and around nanometer-sized structures with at least one characteristic dimension below 100 nm, provides such a platform that deals with pico- to femtoliter volumes. In nanofluidics, the governing forces scale different compared to those in the macroscopic world. The dynamics of particles at the nanometer length are affected by intermolecular forces such as van der Waals and electrostatic forces rather than gravitational and inertial [40]. Additionally, since the surface-to-volume ratio increases with decreasing dimensions it is high in nanofluidic channels. Electrostatic interactions of nano-objects with the surface of the channel can be thus not neglected, since the Debye length, the characteristic length scale of the electrostatic potential, is on the order of the channel dimension [41]. Additionally, the constant movement of particles in solution is the cumulative effect of countless collisions with thermal excited solution molecules, called Brownian motion [42]. It is the major transport process in chemical reactions and biological life at cellular and subcellular levels. Brownian motion, however, makes the studying of dynamics and structures of single nano-objects in fluids challenging. As an example, a particle with a diameter of 60 nm will on average travel a distance through a focused laser beam of 1  $\mu\text{m}$  within only 150 ms, which limits the observation time and tracking of its motion. One possibility to overcome this limit is to immobilize the object of interest to a surface. In such an approach, called tethered-particle motion assay, Schafer *et al.* measured the single movement of individual RNA polymerases along a DNA strand, by immobilizing the RNA polymerase to a glass surface and monitoring the motion of a 40 nm gold particle attached to the ends of DNA molecules being transcribed [1]. Such a chemical surface attachment, however, has to be carried out carefully to avoid denaturation and malfunction of the immobilized molecules [43].

### 2.2. Contact-free trapping of particles and molecules in fluids

Another approach is the contact-free trapping of a single object in solution by suppressing its Brownian motion with energy potential wells that are deeper than the thermal energy of the object. On average, every particle has an energy of  $1/2 k_{\text{B}}T$  along each translational dimension [42]. But, the instantaneous velocity of a particle follows a Maxwell-Boltzmann distribution [44–46], in which the energy of the particle can temporarily considerably exceed the average value. To compensate for these stochastic kicks, Ashkin *et al.* established a rule of thumb, that stable trapping requires a potential depth of around  $10 k_{\text{B}}T$  [47, 48]. To create such energy potentials for trapping micro- and nanometer-sized objects, several methods have been developed and improved over the last 30 years. These achievements were possible due



to the development of various new technologies such as nanofabrication, fast and sensitive electronics, optics, and new optical devices.

One of the most established trapping methods in solution are "optical tweezers" [49, 50]. In 1970, Ashkin reported on the acceleration of freely suspended dielectric particles by the forces generated due to the radiation pressure of a tightly focused laser beam [51]. This work led to the first optical trap in 1986 [47], where the trapping of particles larger (Mie regime) as well as smaller (Rayleigh regime) than the wavelength of the laser was demonstrated. The first three dimensional (3D) tracking of particles in an optical trap was shown by Bartlett *et al.* using a high-resolution back-focal-plane quadrant detector [52]. Several trap geometries, from a single trap to a double trap and multiple independently controllable trap lattices, were demonstrated using programmable diffraction optical elements (spatial light modulator) [53]. Since its first report, the optical tweezers method was extensively used in biological and medical applications, such as force sensing on DNA [54] and protein molecules [23, 31], refractive index measurements of single virus particles [55], and the analysis of power generation and motility efficiency of living parasites [56]. Beyond using optical tweezers as an analyzing method, it was applied as a manipulation tool to move and relocate trapped objects to a desired position. This feature was used to sort particles by refractive index and size in a flow device [57], pattern Au NPs on surfaces with high precision [58], assembling nanowires in water to build a photonic device [59], or to move living trypanosomes from fluidic channels into reaction chambers for drug measurements [60]. One major drawback of optical tweezers is that the restoring force  $F_{res} \propto \alpha |\nabla E|^2$  acting on the particle in the Rayleigh regime is proportional to the polarizability,  $\alpha$ , of the trapped objects, which scales with the third power of the object radius ( $R^3$ ). In addition,  $\alpha$  vanishes when the material properties of the object and its surrounding media are similar, which could be the case for many biological entities in water. Although the trapping of ever smaller objects down to 30 nm in diameter was demonstrated using optical tweezers [61], large field powers in the order of hundred mW are needed to create a strong field gradient, which might lead to photodamage of the specimens [62] or to local heating [63].

Another trapping method that relies on light field gradients uses nanostructures and is called "plasmonic tweezers" [48, 64]. In this approach, which was first predicted by Novotny *et al.* and Martin *et al.*, plasmonic nanostructures are designed that serve as antennas to efficiently couple propagating light and thus concentrate and enhance it into highly localized near-fields, much smaller than the diffraction limit [65, 66]. As a result, using moderate illumination powers, such structures generate much higher gradient forces and thus deeper potential wells compared to far-field methods like conventional

optical tweezers. In one of the first experimental implementations, Righini *et al.* demonstrated the trapping of micrometer sized polystyrene beads by circular gold micro-discs fabricated on a glass slide using a non-focused laser illumination [67, 68]. They reported that the incident laser intensity needed to trap the beads was around two orders of magnitude smaller than that required to trap the same beads using conventional optical tweezers. Additionally, since the gold structures were significantly smaller than the illumination field, parallel trapping of several beads were shown on a predefined pattern of structures. By combining plasmonic and optical tweezers, using gold dimer-disc structures and a tightly focused laser beam, Grigorenko *et al.* enhanced the trapping to subwavelength sized particles (200 nm polystyrene beads) in the gap of the dimers and demonstrated additionally the ability to move the particles between gaps of several fabricated dimer patterns [69]. In the last few years, further new advanced designs of nanostructures extended the capability to trap ever smaller nanoparticles down to 10 nm in diameter [70] and to manipulate and move the particles by changing the wavelength or polarization of the excitation source [71, 72] or the gaps between the nanostructures [73]. However, as for conventional optical tweezers, the restoring force decreases with the third power of the particle size making the trapping of molecules difficult. Additionally, although significantly less incident illumination powers are needed, the coupling of the light by the plasmonic structures creates strong field gradients and large local intensities that lead to local heating of the metallic structures and heat dissipation into the surrounding water, resulting in thermally induced forces or damage of the trapped objects [48, 74]. One concept to overcome this drawback, is the fabrication of plasmonic tweezers with integrated heat sink structures [75].

Besides optical trapping, another approach is the possibility to use magnetic field gradients to trap or exert forces on paramagnetic particles. In an early work, Smith *et al.* achieved measurements of the elasticity of single DNA molecules by attaching one end of the DNA to a glass surface while monitoring the motion of a micrometer sized magnetic bead attached to the other end of the DNA [76]. By exerting magnetic or hydrodynamic forces on the bead using movable permanent magnets and applied flows in a microfluidic chamber, the DNA stretching behavior was analyzed. Permanent [77] or electro-magnets [78] outside the reaction chamber are generally used to measure the stretching or rotational forces of DNA [77, 78] and RNA [79] molecules or proteins that act on DNA [80]. A different chip based approach was developed by Vries *et al.*, fabricating micrometer sized magnetic structures onto a glass substrate directly in a reaction chamber [81]. Due to large controllable forces generated by the device, they demonstrated the direct manipulation of paramagnetic beads with a diameter of 350 nm inside a living cell [82].

Variations of electric fields are further physical means that can be used for stable trapping of charged or dielectric objects. The planar aqueous Paul trap (PAPT), for instant, uses radio frequency alternating current (ac) voltages generated by four electrodes in two orthogonal directions to create potential wells [83]. With such devices, produced by conventional microfabrication methods, single polystyrene beads with negative surface charges and a diameter of about 500 nm [83] or 100 nm [84] were stably trapped in solution. The particle fluctuations could be manipulated by adjusting the voltages and frequencies. A key benefit of PAPT is that the restoring force scales with the net surface charge (proportional to  $R^2$ ) and mass of the trapped object rather than with the volume ( $R^3$ ). However, low solution conductivity (low ionic strength) is preferred for the ac electrophoretic effect in the PAPT to create sufficiently deep potentials for stable trapping which could make the trapping of biological entities difficult [83]. Alternatively, dielectrophoresis (DEP) uses non-uniform electric fields to trap and manipulate dielectric particles in solution. The electric fields in DEP can be applied by nanofabricated electrodes on a device surface itself [85] or by photoconductive materials that are excited with an external light source [86]. Using DEP, Mernier *et al.* developed a microfluidic device for sorting living from dead yeast cells [87]. Other single particle applications showed the trapping of silicon nanowires [86] or even proteins [85]. Similar to optical trapping methods, the restoring force  $F_{res}$  in DEP methods are proportional to the square field gradient and volume of the particle. A third trap mechanism which relies on an applied electric field is called the anti-Brownian electrokinetic (ABEL) trap developed by Cohen and Moerner. In comparison to all other methods introduced so far, the ABEL trap uses a feedback loop system. The Brownian motion of trapped fluorescence labeled objects is monitored and analyzed in real time and a direct current (dc) feedback voltage is applied by four electrodes so that the electrophoretic drift exactly cancels the Brownian motion [88, 89]. There are several benefits of this method: (i) it was shown that the trapped particles can not only be held in place but as well were positioned with nanoscale resolution in the trap area [88], (ii) since a feedback voltage is applied after each analyzed frame relative to the position of the trapped object, a pseudo-free trajectory of the particle can be calculated [89], (iii) the restoring force  $F_{res}$  scales with the net charge of the particle and the stiffness of the trap is dependent on the feedback loop and thus on the diffusion, which is proportional to the radius  $R$  of the particle and the viscosity of the medium [88]. Thus the ABEL trap is an example method that could benefit from fast electronics and thus fast feedback cycles. Several single nano-objects were stably trapped using the ABEL trap, such as 20 nm polystyrene beads [88], viruses, vesicles and proteins [90]. Further, the method was used to analyze enzymatic [91] properties of proteins or to determine the diffusion coefficient and electrokinetic mobility

of proteins in solution [92].

There are several other methods that are used for stable trapping of single objects. Acoustic tweezers for instance, using sound waves to create potential wells, are most commonly used to trap and manipulate micrometer sized objects [93]. The trapping of red blood cells [94], entire organisms [95] or Zebrafish eggs [96] were demonstrated and found e.g. application in tissue imaging. Acoustic tweezers are considered as a non-invasive trapping method for micrometer sized biological entities such as cells or tissues, since the power density used, were significant smaller than compared to optical tweezers [95]. However, trapping of nanometer sized objects has not been shown to date.

A trapping method that is independent of the physical and chemical properties of the trapped object is microfluidic-based hydrodynamic trapping [97, 98]. Such a trap is solely based on hydrodynamic fluid flow in a microfluidic device with two perpendicular channels. Opposing laminar flow streams converge in the junction of the channels, which result in a planar extensional flow profile with a fluid stagnation point in the middle where the velocity is canceled out. Perkins *et al.* used the elongation flow profile to explore the coil-stretch dynamics of individual DNA molecules [97]. Due to the fluid stagnation point, long observations of several seconds could be achieved of individual DNA molecules. Using a feedback control algorithm that actively adjusts the fluid flow of the two opposing flow streams based on real time image acquisition and tracking of the trapped object, Johnson-Chavarria *et al.* demonstrated trapping of 100 nm to 2.2  $\mu\text{m}$  fluorescent polystyrene beads for several minutes in the stagnation point [98].

As a last example, the trapping and manipulation of objects by controlled temperature fields is another method that might seem counter intuitive at the first sight. Although temperature is the driving force of the Brownian motion and higher temperatures would make the trapping in all other introduced methods more difficult, applied temperature gradients can be used to move objects in solutions. This method is called thermophoresis [99, 100]. By smart designs, potential wells were created by temperature gradients using micrometer-sized electric thermal heater [101] or plasmonic heat structures [102]. Successful trapping of cells, polystyrene beads down to 500 nm and single DNA molecules was demonstrated [101, 102].

As introduced, there are various methods for single particle trapping and depending on the desired object to trap and scientific question to answer, some are more suitable than others. As a result, before selecting a trapping method several questions should be answered as for instance: What are the material properties and size ranges of the trapped objects? Is a single trap or

multiple trap desired? How long should the objects be confined? Should there be the possibility of actively manipulating the object or only trap it. Is there an increased likelihood of heat- or photodamage on the confined particle? How much external power is needed and how complicated is the build-around to concentrate the power in the reaction chamber? How much are the material and fabrication costs to build a trap or devices with integrated traps?

## 2.3. Theory of geometry-induced electrostatic trapping

This work focuses on devices, that are capable of primarily trapping individual objects smaller than 100 nm in solutions without the need of any externally applied fields. The mechanism is based on the electrostatic repulsion between charged particles and surfaces of nanofluidic channels. This method, called geometry induced electrostatic (GIE) trapping, was first reported by Krishnan *et al.* in 2010 [17], and over the years, was demonstrated in different variants [103, 104] and for applications [34, 105] that will be discussed in more detail in Section 2.4.

### 2.3.1. Electrostatic forces by induced surface charges

The main driving force for confining objects in GIE trapping devices is based on electrostatic forces that are generated by induced surface charges in solution on both the device and object surfaces. Electrostatic forces are classified as long-range forces. Compared to shorter-range van der Waals forces that are always attractive between similar objects, electrostatic forces can be repulsive or attractive, depending on the surface net charge of the particles and device surface. The charges of such a surface in a fluid can arrive from either ionization or dissociation of surface groups, or by the adsorption or binding of charged molecules from solution [40]. The GIE trapping devices are primarily made from SiO<sub>2</sub> substrates such as glass or thermally grown SiO<sub>2</sub> from bare silicon. Typically, at the surface of SiO<sub>2</sub>-based materials, covalent Si–O–Si and silanol groups Si–OH are present as shown in Fig. 2.1A [40, 106, 107]. In contact with water, a fraction of the silanol groups are ionized by the dissociation of H<sup>+</sup> ions following the equilibrium [108]



The resulting surface charge density ( $\sigma_s$ ) is given by

$$\sigma_s = \sum_i q_i / A \quad (2.2)$$

where  $q_i$  is the net charge of the ion, given by the product of the valency  $z_i$  of the ion and the electron charge  $e$  ( $q_i = z_i e$ ), and  $A$  is the surface area. For

the silanol groups in aqueous solution with a surface concentration of  $\Gamma_{\text{SiO}^-}$  of the dissociated head groups, the surface charge density can be written as

$$\sigma_s = -e \Gamma_{\text{SiO}^-} . \quad (2.3)$$

The amount of dissociated head groups  $\Gamma_{\text{SiO}^-}$  is dependent on the crystalline structure of the  $\text{SiO}_2$  material as well as on the equilibrium between the ions at the surface and the free counter ions in the bulk solution and thus depends on the pH and the ionic strength of the solution. For glass in aqueous solution,  $\sigma_s$  can vary from  $-0.5 \text{ mC/m}^2$  at  $\text{pH} = 3$  up  $-50 \text{ mC/m}^2$  at  $\text{pH} = 9.5$  at a monovalent ionic concentration of the bulk solution of  $c_0 = 1 \text{ mM}$  [107]. However, for the majority of the experiments performed in this work at pH around 6 and at an ionic concentration of about  $c_0 = 0.1 \text{ mM}$ ,  $\sigma_s$  is in the order of  $-1 \text{ mC/m}^2$ .

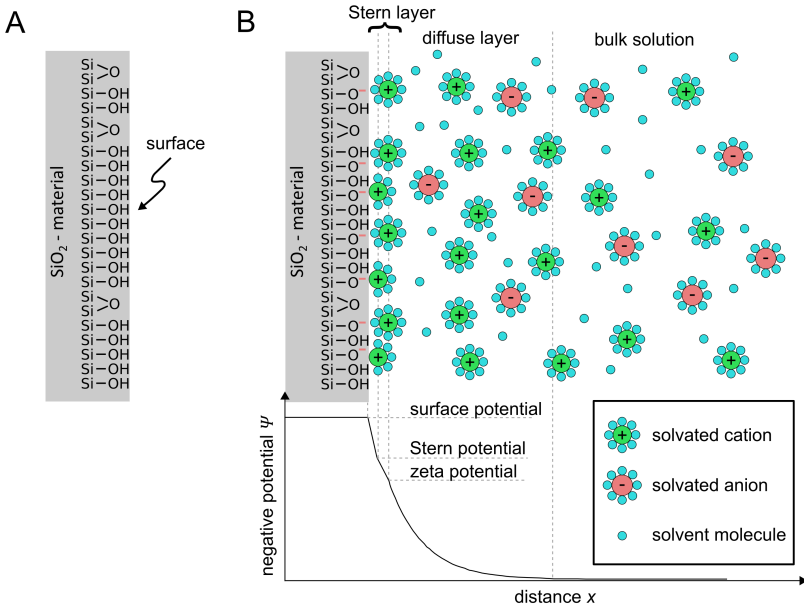


**Figure 2.1.:** Schematic of a  $\text{SiO}_2$  surface. B) Structure of the EDL at a negative charged  $\text{SiO}_2$  surface in contact with a polar solvent.

Such induced surface charges are then balanced by an equal amount of counterions (ions with opposite charge) that surround the surface. These

counterions typically remain mobile close to the surface and are referred to as the electric double layer (EDL) as shown in Fig. 2.1B. In the EDL, some of the counterions are in contact to the surface and form a compact layer at the surface interface called the "Stern layer" [109]. Others are not rigidly held, but diffuse around the surface and into the bulk solution due to thermal motion, forming the so called "counterion diffuse layer" known as the Gouy-Chapman model [110, 111]. Beyond this layer, in the bulk solution, the concentration of counterions and coions is equal. Taking a planar charged surface in  $yz$ -plane, in equilibrium, the ion distribution (number density of ions) beyond the Stern layer can be described according to the Boltzmann distribution [40]

$$c(\Psi) = c_0 e^{-ze\Psi/k_B T}, \quad (2.4)$$

where  $c_0$  is the bulk number density of ions,  $z$  the valency of the ions (including the charge sign),  $e$  the elementary charge and  $\Psi$  the position dependent electrostatic potential. Combined with the Poisson equation

$$z e c(\Psi) = -\epsilon (d^2\Psi/d^2x), \quad (2.5)$$

which relates the potential with the charge density, results in the nonlinear Poisson-Boltzmann (PB) equation

$$\frac{d^2\Psi}{d^2x} = -\frac{z e c_0}{\epsilon} e^{-ze\Psi/k_B T}, \quad (2.6)$$

describing the charge distribution and electrostatic potentials at any point of  $x$ . Here  $\epsilon$  is the dielectric permittivity of the solution.

In other words, the net charge density of the counterions is the highest at the surface and drops with the distance  $x$  as seen in Fig. 2.1B. At a certain distance away from the surface, the net charge asymptotically reaches 0, which describes the bulk solution with equally distributed co- and counterions. For moderate ionic concentration and small potentials, the PB equation can be linearized with the Debye-Hückel approximation which describes the electrostatic potential  $\Psi$  as an exponential decay from the surface as [40]

$$\Psi = \Psi_0 e^{-\kappa x}, \quad (2.7)$$

where  $\kappa^{-1}$  is the characteristic length scale of the potential, called the "Debye length", describing the length where the potential has dropped  $e^{-1}$  of the original value and  $\Psi_0$  the surface potential at  $x = 0$ . According to the Grahame equation [40, 112]  $\Psi_0$  is proportional to the surface charge density  $\sigma_s$  and the Debye length  $\kappa^{-1}$  as

$$\Psi_0 = \frac{\sigma_s \kappa^{-1}}{\epsilon}. \quad (2.8)$$

where

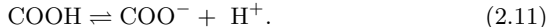
$$\kappa = \left( \sum_i \frac{c_{0,i} e^2 z_i^2}{\epsilon k_B T} \right)^{1/2} \text{ m}^{-1}. \quad (2.9)$$

with  $c_{0,i}$  the ionic concentration of ions  $i$  in the bulk solution. Assuming a monovalent electrolyte ( $z = 1$ ) at 25°C, such as NaCl in solution, the Debye length is given by [40]

$$\kappa^{-1} = \frac{0.304}{\sqrt{c_0}} \text{ nm}, \quad (2.10)$$

where  $\kappa^{-1}$  is in the units of nanometers and  $c_0$  is in molar, M.

Similar to the planar surface, nanoparticles or molecules in water can as well carry a surface charge by the ionization or dissociation of surface groups. Negatively charged Au NPs that were primarily used in the experiments of this work are coated with carboxylic groups that dissociate  $\text{H}^+$  according to the following equilibrium



The resultant electrostatic potential, and thus the electrostatic repulsion between the particles in a colloidal solution prevent the particles from forming aggregations.

### 2.3.2. Contact-free trapping by geometry-induced electrostatic potential wells

A 3D graphic of a basic GIE trapping device is shown in Fig. 2.2. It consists of a  $\text{SiO}_2$  material (e.g. a  $\text{SiO}_2$ -layer grown on a Si surface as shown in the figure or an amorphous glass) with a structured surface topography and a covalently bound cover slip glass [17, 105]. The structured  $\text{SiO}_2$  material is fabricated by etching nanofluidic channels into the surface using state-of-the-art nanofabrication tools such as electron beam (e-beam) lithography and anisotropic reactive ion etching (RIE). The nanofluidic channels are further tailored with finer indentations, i.e. the nanotraps. Using e-beam lithography various trap designs and sizes such as circular pockets, rectangular slits, or grids, can be realized as shown in the 3D graphic of Fig. 2.2. The structured chips are finally bonded to a cover glass to seal the devices and provide optical access from underneath. When exposed to water, the walls of the nanofluidic channels become negatively charged as described earlier. Introduced negatively charged nano-objects become stably confined in the integrated traps without surface contact and in the absence of any externally applied power by electrostatic repulsion from the nanofluidic walls.



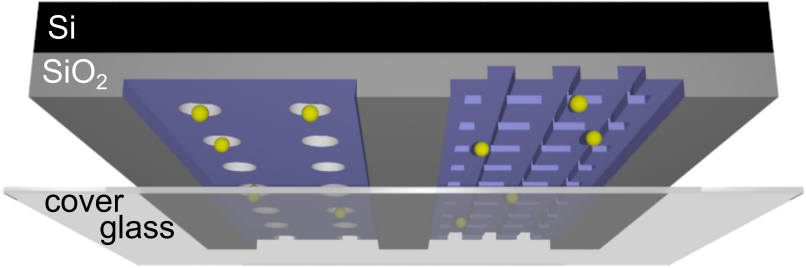


**Figure 2.2.:** Schematic of a GIE trapping device made from a Si-substrate. Nano-objects are trapped by the fine structures etched into the nanofluidic channels in the  $\text{SiO}_2$  layer. The cover glass in the schematic is cut half open for better visualization.

A cross section sketch of a GIE trapping device with the used dimension range is shown in Fig. 2.3A. The nanofluidic channels have a width of  $w_c = 10 - 30 \mu\text{m}$ , a height of  $h_c = 50 - 200 \text{ nm}$  and a length  $L$  of several millimeters, depending on the trapped objects. The finer indentations had a height of  $h_p = 25 - 100 \text{ nm}$  and a width of  $w_p = 100 - 500 \text{ nm}$ . The influence of the geometric dimensions of the device as well as the ionic concentration of the solution and the surface charge density of the device and the particle are discussed later in Section 2.9. The working principle of a GIE trapping device can be best explained by the simplified model of two negatively charged parallel surfaces placed next to each other as shown in Fig. 2.3B [105]. The negative electrostatic potential of each surface in water has an exponential decay as described by Eq. 2.7. If the two plates are placed far from each other (case I in Fig. 2.3B), the negative electrostatic potential of each plate decreases from  $\Psi_0$  at the surface to an asymptotic value of 0 in the midplane of the two plates. Thus, the experienced electrostatic potential in the middle of the gap between the two surfaces vanishes. However, if the two plates are set closer to each other (case II), the two electrostatic potentials start to overlap. This results in the sum of both exponential functions, forming a local minimum in the midplane larger than the negative electrostatic potential of the midplane of case I [41, 113–115]. In GIE trapping, both discussed cases are integrated into one device as highlighted in Fig. 2.3A. In the nanofluidic channels, where no traps are implemented, the close top surface of the chip and bottom surface of the cover glass matches case II. In the area with a trap, however, both surfaces are further apart from each other, similar to case I, forming a local energy potential well. As a result, negatively charged nano-objects in the nanofluidic channel experience a higher repulsion from

the walls all over the channel (case II) than within the smaller traps (case I). The nano-objects are thus pushed into these potential wells and trapped for several milliseconds to days depending on the depth of the created potential well.

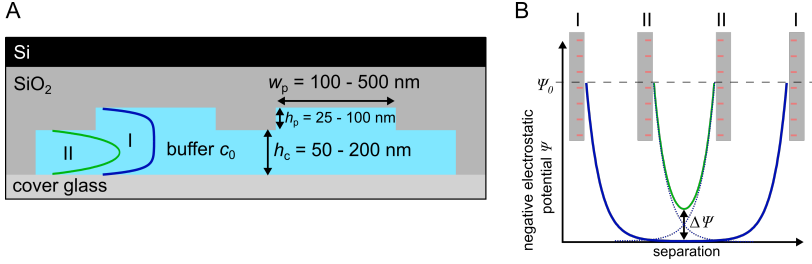


**Figure 2.3.:** A) Cross section sketch of a GIE trapping device through two cylindrical pockets with the typical dimensions used. B) Simplified model explaining the GIE trapping working principle with two surfaces separated far from each other (case I, non overlapping potentials) and two surfaces placed closer to each other (case II, superposition of the two potentials). Both cases are present in the GIE trapping device, which results in potential wells of depth  $\Delta\Psi$ .

As an example to demonstrate the geometry induced creation of potential wells inside the device, the electrostatic potential energy landscape  $\Psi$  per elementary charge, obtained by solving the nonlinear Poisson-Boltzmann equation numerically [17] (COMSOL Multiphysics 4.2) of a sample device with  $h_c = 160$  nm,  $w_p = 500$  nm and  $h_p = 100$  nm, is shown in Fig. 2.4A. For the simulations, a surface charge density of about  $\sigma_s \sim 3 \cdot 10^{-3} e \text{ nm}^{-2}$  [107] at a monovalent salt concentration of  $c_0 = 0.1$  mM according to experimental data. The extraction of the energy potential of a point charge along the  $z$ -axis at the middle of the trap at the position  $r = 0$  nm (blue) and outside the trap at  $r = 400$  nm (green) is shown in Fig. 2.4B. This extraction is equivalent to the simplified model demonstrated in Fig. 2.3. The corresponding extraction of the electrostatic potential energy of a point charge of  $-1 e$  as a function of  $r$  along the axial energy minimum (black dashed line in Fig. 2.4A) is shown in Fig. 2.4C. Here, the energy difference between the midplane of the nanofluidic channel outside the pocket at  $r = 400$  nm (light red) and the minimum potential at the center  $r = 0$  nm of the pocket (dark red) reaches a value of  $\Delta\Psi = \Psi_{r=400, \min} - \Psi_{r=0, \min} = 0.095 k_B T$ . As a result, assuming a 80 nm Au NP as a point charge inside the trap, carrying a net charge of  $q \sim -168 e$  (experimental data), potential depths of  $\Delta Q = q \Delta\Psi \sim 16 k_B T$  can be achieved as seen in Fig. 2.4D, which is sufficiently larger than the

average thermal energy of a particle of  $1/2 k_B T$  in one dimensional translation and higher than the required  $10 k_B T$  suggested by Ashkin *et al.* for stable trapping [47].

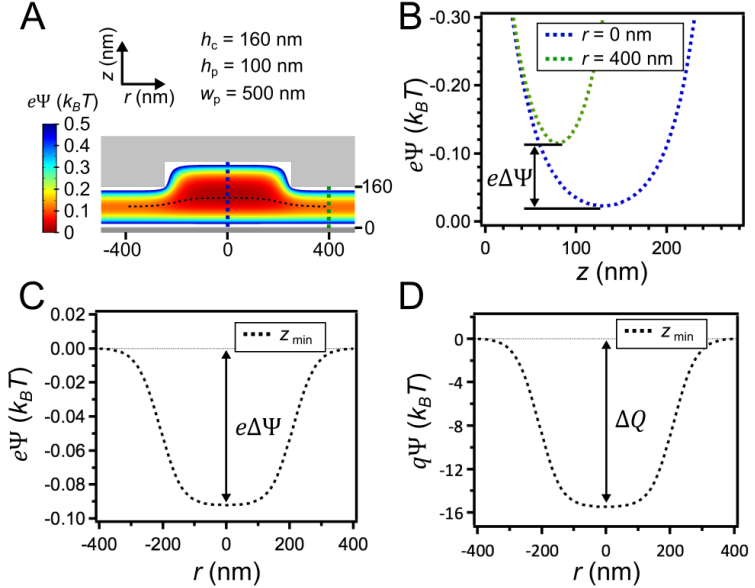


**Figure 2.4.:** A) 2D electrostatic energy landscape of a circular trap  $\Psi$  per elementary charge  $e$  with the dimensions of  $h_c = 160$  nm,  $w_p = 500$  nm and  $h_p = 100$  nm obtained by numerically solving the nonlinear Poisson-Boltzmann equation. B) Extraction of the energy potential from A) along  $z$  at the middle of the trap at the position  $r = 0$  nm (blue) and outside the trap at  $r = 400$  nm (green). C) Extraction of the energy potential from A) along  $r$  at  $z_{\min}$ . D) Energy potential along  $r$  at  $z_{\min}$  multiplied with a point charge of  $q \sim -168 e$  (equivalent to a Au NP with diameter 80 nm) results in a potential well with a depth of  $\Delta Q = q\Delta\Psi \sim 16 k_B T$ .

The simplified model with the two plates explaining the GIE trapping principle and assuming a point charge for the particle to simulate the electrostatic potential energy landscape gives a good estimate of the potential depth for the case that the diameter  $d$  of the particle is substantially smaller than the nanofluidic channel height  $h_c$ . However, for larger particles or smaller channel heights, the finite particle size has to be taken into account to fully understand the characteristics of the trap. Krishnan introduced a model for simulating the electrostatic free energy  $F_{e1}$  of the total system including the

particle as [116]

$$F_{\text{el}} = U_{\text{el}} - T\Delta S \quad , \quad (2.12)$$

where  $U_{\text{el}}$  is the sum of all electrostatic field energies (including the particle) in the system and  $\Delta S$  is the change in entropy of mixing a dilute solution of charges. The corresponding potential depths were obtained by sweeping the particle from the center to the outside of the trap and calculating the total free energy of the system for each position. Using this model, the importance of the counterion entropy and particle size was demonstrated by simulating that even uncharged particles might be trapped within potential depths  $> 10 k_{\text{B}}T$ , if the normalized particle diameter  $d/h_c$  is larger than about 0.6. [116] This phenomenon was explained by the repelling of the particle from the nanofluidic channel into the trap caused by the counterion entropy of the nanofluidic channel walls. This so called "entropic trap" was used by Reisner *et al.* to study the diffusive behavior and correlated fluctuations of DNA molecules between two or more nanofluidic traps at higher salt concentrations [117–119].

## 2.4. Geometry-induced electrostatic trapping - developments and applications

GIE trapping has evolved to be used for stable trapping of single Au NPs [7, 17, 120], polystyrene beads [17], lipid vesicles [17], as well as for angular dependent trapping of silver nanorods in slit like trap geometries [121]. Using these nanorods, binary switching was demonstrated in T-shaped traps with the help of an external applied electric or optical field, which might mark the first step towards digital colloidal information storage applications [122]. Furthermore, by combining experimental data with numerical simulations, Mojarad *et al.* determined the charge and size of single gold nanoparticles in solution by studying the motion and contrast fluctuations of the particles in the traps [7]. Analyzing trapping and escaping events of individual proteins and short DNA molecules, Ruggeri *et al.* measured the net charge of the molecules, which demonstrated a first biological application using GIE trapping [34]. Using single trapped silica particles Kokot *et al.* measured the electrical charge of  $\text{SiO}_2$  surfaces in different polar and nonpolar solvents. They found that even in nonpolar media, electrostatic trapping is achievable. Beside the chip-based realization, electrostatic trapping was further developed as a tweezer equivalent, called scanning-aperture trapping, using a nanopipette approaching close to a glass surface to form an electrostatic potential well [103]. The key advantage of this method is the 3D scanning capability and thus the possibility of altering the trap potential depth during the experiment by approaching or releasing the nanopipette closer to or further away from the glass surface. However, this approach is limited to a single trap only and a more complex experimental setup. The ability to manipulate and tune the

nanofluidic channel height during the experiment in a chip-based approach can be realized with flexible materials as explained in Chapter 5. Combining the GIE trapping method with integrated microfluidic systems (see Chapter 4) led to the trapping and screening of Au NPs along a salt gradient, which might be used for sensing ionic solutions or high-throughput screening over a range of reactant concentrations on trapped particles or biomolecules [124]. With these integrated microfluidic systems, charge-reversal of the nanofluidic channel and trap walls was realized by coating the channels with positively charged polyelectrolytes, resulting in the trapping of positively charged gold nanoparticles down to 60 nm in diameter [125].

## 2.5. Tracking of particles and molecules in fluids

The tracking of lateral and spatial movements of objects such as particles, molecules or viruses through cells, along and across membranes or polymer filaments such as DNA or microtubules can be obtained by detecting the position of the object in each acquired image frame. Such single particle tracking measurements were realized with nanometer localization far below the diffraction limit of the microscope by fitting the intensity distribution that appears for a spherical imaged object as the point spread function (PSF) (see Section 2.7).

Fluorescence microscopy is a standard way of real-time single object tracking where the object of interest is labeled with a single or multiple chemical fluorophore(s) [11]. The red-shifted emission of the fluorophore is filtered from the incident light which provides high SNR detection. One of the first works on imaging single fluorescent molecules in aqueous solution was demonstrated by Funatsu *et al.*, observing ATP turnovers of a single fluorescent labeled molecular motor protein, myosin, or tracking the movement of single kinesin molecules along a microtubule [126, 127]. Nowadays, several fluorescence-based techniques such as confocal fluorescence microscopy, total internal reflection fluorescence microscopy, fluorescence correlation spectroscopy, or super resolution microscopy are available and have their advantages and limitations based on their experimental applications like time resolution, observation volume or SNR [14, 128]. However, despite achievements in fluorescence dyes and antifadent solutions (solutions, that reduce the photobleaching of fluorescence dyes), the observation based on fluorescent labeled objects has its own limitations such as photobleaching, temporary fluorescence blinking at fast acquisition rates or unwanted autofluorescence of background specimens [11, 128, 129]. The ability to only view the fluorescent labeled object could be another limitation depending on the scientific question when other background objects are of interest.

Fluorescence recovery after photobleaching (FRAP) provides an alternative approach by recording the recovery of fluorescence intensity of fluorescent labeled objects diffusing into an area that was previously photobleached with high intensity light. Although in most studies FRAP was so far not used as a single molecule detection method, Mudumbi *et al.* demonstrated the determination of distribution and translocation rates of single nuclear envelope transmembrane proteins in the nuclear envelope using a single-point FRAP microscopy technique [130]. The limit of photobleaching and photoblinking of single fluorophore labeled objects can be further bypassed by analysing unlabeled objects in a fluorescent surrounding media, called inverse-fluorescence correlation spectroscopy (iFCS) [131]. Using iFCS and apertures of 100 nm diameter etched into a thin gold film that result in zeptoliter observation chambers, the volume, concentration and mobility analysis of single label-free protein molecules and nanoparticles was demonstrated [132].

Apart from fluorescence-based microscopy techniques, methods based on elastic light scattering have the advantage of directly observing label-free nano-objects. For nano-objects that are small compared to the wavelength ( $d \ll \lambda$ ) of the incident light field  $E_i$ , the scattered field  $E_s$  at the detector is given by  $E_s = sE_i$ , where  $s = |s|e^{i\varphi}$  scales with the polarizability  $\alpha$  of the particle [15, 18],

$$s(\lambda) = \eta\alpha(\lambda) = \eta\epsilon_m(\lambda) \frac{\pi d^3}{2} \frac{\epsilon_p(\lambda) - \epsilon_m(\lambda)}{\epsilon_p(\lambda) + 2\epsilon_m(\lambda)} \quad (2.13)$$

with the complex dielectric constants of the particle  $\epsilon_p(\lambda)$  and the medium  $\epsilon_m(\lambda)$ , the constant  $\eta$  that takes the detection efficiency of the experimental setup into account and  $\varphi$  the scattering phase. The measured intensity at the detector is thus given by [15]

$$I_{\text{det}} = |E_b + E_s|^2 = |E_i|^2 \{b^2 + |s|^2 - 2b|s| \sin \varphi\} \quad (2.14)$$

with the background field  $E_b = bE_i$  and the background intensity  $|E_b|^2$ . Methods based on elastic light scattering normally try to cancel the background  $b$  as much as possible to obtain a purely scattered signal of the nano-object at the detector described by the term in Eq. 2.14 of  $|E_i|^2 |s|^2$ . This can be achieved by experimental setups such as scanning near-field optical microscopy (SNOM), dark-field microscopy or total internal reflection microscopy. Imaging nanometer-sized objects using light scattering was demonstrated mainly for metallic particles. Sugiura *et al.*, e.g., reported on the detection of 40 nm Au NPs attached to a cover glass using a SNOM approach [133] whereas Sönnichsen *et al.* reported on the detection of 68 nm gold disc fabricated on a glass substrate using total internal reflection microscopy [134]. Since metallic nanoparticles do not photobleach, Schultz *et al.* suggested using

them as biomarkers and thus replace or complement the methods based on fluorescence labeled biomolecules [135]. They demonstrated the detection of antibody coated silver nanoparticles using a dark-field microscopy on chicken muscles. Additionally they found different detected colors of the nanoparticles depending on their size and shape due to different plasmon resonances. However since the pure scattering signal scales with  $d^6$  (see Eq. 2.13 and 2.14), the fast and precise tracking and detection of nano-objects smaller than 40 nm remains challenging since the scattered signal quickly vanishes in the noise of the background intensity if the object size decreases [15].

## 2.6. Interferometric scattering (iSCAT) detection

To overcome this limit, a new method was introduced using a focused laser beam and an interferometric detection scheme, called interferometric scattering detection (iSCAT) [15, 18–20]. This technique takes advantage of the background field  $E_b$  rather than eliminating it. The basic principle is seen in Fig. 2.5A. It is based on the interference between the scattered light of the object  $E_s = sE_i$  and a reference beam  $E_r = rE_i$  that is partially reflected at the glass/water interface from the incident beam. The total field at the detector  $E_{\text{det}}$  is given by the sum of the scattered and reflected fields,  $E_{\text{det}} = E_r + E_s$ . The corresponding intensity  $I_{\text{det}}$  can be written as [18]

$$I_{\text{det}} \propto |E_r + E_s|^2 = |E_i|^2 \{r^2 + |s|^2 - 2r|s| \sin \varphi\}. \quad (2.15)$$

Here, the first term proportional to  $r^2$ , represents the background intensity, which, in the case of a Au NP on the glass surface, originates mainly from the reflected beam at the glass/water interface. For the case of an Au NP in a GIE trapping device see Chapter 3. The second term in Eq. 2.15, proportional to  $|s|^2$ , is the pure scattering which drops by  $d^6$ . The last term however,  $2r|s| \sin \varphi$ , represents the interference of the reflected and the scattered field and decreases with  $d^3$ . Since the reflected field at the glass/water interface is constant for a fixed illumination, the contrast  $K$  can be defined as

$$K_{\text{det}} = |E_{\text{det}}/E_r|^2, \quad (2.16)$$

which, combined with Eq. 2.15, leads to

$$K_{\text{det}} = \frac{|E_i|^2 \{r^2 + |s|^2 - 2r|s| \sin \varphi\}}{|E_i|^2 r^2} = 1 + \frac{|s|^2}{r^2} - \frac{2r|s| \sin \varphi}{r^2}. \quad (2.17)$$

For large particles, or strong scatterers, the scatter and interference terms compete and with increasing particle diameter, the pure scattering signal dominates. However, for small particles, assuming  $r \gg s$ , the pure scattering

term can be neglected, which results in a pure interferometric detection as [15]

$$K_{\text{det}} = 1 - \frac{2r |s| \sin \varphi}{r^2}. \quad (2.18)$$

When decreasing the object size, the interferometric term decays much slower ( $d^3$ ) as opposed for the pure scattering term ( $d^6$ ) thus providing the advantage of detecting and tracking very small particles using iSCAT. An example iSCAT image of 60 nm Au NPs trapped in  $w_p = 100$  nm pockets is shown in Fig. 2.5B.

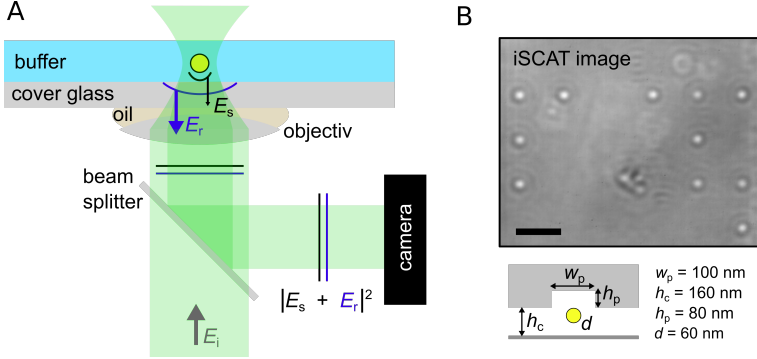


**Figure 2.5.:** A) Schematic of a particle detected by iSCAT at a glass/water interface showing the path of the incident beam  $E_i$  and the two competing fields scattered from the nano-object  $E_s$  and reflected at the glass/water interface  $E_r$ . B) Example iSCAT image of 60 nm Au NPs trapped in  $w_p = 100$  nm pockets. Scale bar:  $3 \mu\text{m}$ .

iSCAT detection was frequently used in the last years to detect label-free metallic nanoparticles and even biomaterials. In a first work, Lindfors *et al.* detected fixed 5 nm Au NPs on a glass substrate at a glass/oil interface using a supercontinuum white light source [18]. Jacobsen *et al.* extended this work by demonstrating the detection of fixed Au NPs at a glass/water interface down to 5 nm using confocal scanning iSCAT. Krishnan *et al.* implemented a laser scanning system based on acousto-optic deflectors (AODs) which provided high acquisition rates of up to 1kHz [17]. They used the system to track 80 nm and 100 nm Au NPs in GIE trapping devices. Because of the additional high sensitivity of iSCAT in the phase difference between the reference and scattered beam and the consequential contrast change in axial movements of the particles they demonstrated 3D tracking with less than 5 nm localization accuracy [17, 120]. The high speed imaging and localization precision resulted in the application of measuring the net charge and size of 100 nm gold particles in electrostatic traps [7]. Furthermore, Tae Kim *et al.* demonstrated the tracking of Au NPs down to 10 nm as well contact-less



confined in an electrostatic trap [103]. By taking advantage of the high axial sensitivity, Fringes *et al.* used iSCAT to measure the confinement gap distance between two surfaces with nanometer accuracy and simultaneously studied the confinement dependent behavior and diffusion of nanoparticles [104, 136]. The first concrete biological application of iSCAT for single molecule tracking was shown by Kukura *et al.* [20]. They used a combination of iSCAT and fluorescence microscopy and thereby could simultaneously detect the fluorescence signal of a quantum-dot labeled to one position of the virus and its center of mass by iSCAT. In this way it was possible to track the position and orientation of the virus moving along a lipid bilayer. Further single biomolecule detections using iSCAT were demonstrated by Andrecka *et al.* by directly observing label-free single microtubules and tracking their stepwise 8 nm motion driven by surface-bound kinesin molecules [29]. More recently, Ortega Arroyo *et al.* imaged individual unlabeled actin filaments and single unlabeled myosin molecules traveling along the actin filaments [137]. By tracking the motion of the single myosin molecules the velocities were analyzed depending on the ATP concentration in the solution.

These studies show the tremendous potential of iSCAT for high sensitivity detection and fast imaging with high localization precision of metallic nanoparticles as well as direct label-free detection of biological entities. In this work, mainly iSCAT detection equipped with a  $\lambda = 532$  nm solid state laser and Au NPs as probes are used to characterize the performance of the GIE trapping devices (see Appendix A for details of our system). Au NPs are the prime choice for analyzing the trap performance. They provide high scattering signals due to the strong plasmon resonance peak in the wavelength range of  $\lambda = 530 - 550$  nm, they are photochemically stable and commercially available in sizes ranging from 2 nm to several hundred nanometers (BBI Solutions, UK). Further, Au NPs can be functionalized with different coatings resulting in positive or negative surface charges and are available in polar and non-polar media. In this study, negatively charged Au NPs carry carboxylic groups ( $\text{COOH} \rightleftharpoons \text{COO}^- + \text{H}^+$ ) whereas positively charged Au NPs are functionalized with branched polyethyleneimine ( $\text{NH}_2 + \text{H}_2\text{O} \rightleftharpoons \text{NH}_3^+ + \text{OH}^-$ ).

## 2.7. Two-dimensional sub-diffraction localization

In conventional optical microscopy, the spatial resolution is limited by the diffraction. The intensity distribution of a spherical object smaller than that limit thus appears as a point spread function (PSF), which has an Airy disc shape as seen in Fig. 2.6A [11, 138]. The width of the PSF can be approximated as  $\lambda/[2(\text{NA})]$ , with the wavelength  $\lambda$  and the numerical aperture NA of the objective [11]. For the setup used in this work, with a

laser wavelength of  $\lambda = 532$  nm and a NA of the oil objective of 1.3, this width is about 200 nm. Two objects separated less than this distance are thus not resolvable. However, for objects that are separated larger than this distance, sub-diffraction localization can be realized by finding the center of the PSF [139]. The central maximum of the PSF contains 85% of the signal as seen in Fig. 2.6A [11] and can be thus fitted with a Gaussian function which turned out to be a good algorithm in terms of both accuracy and precision, as [140]

$$I(x, y) = I_{\text{bg}} + I_a \exp \left\{ -\frac{1}{2} \left[ \left( \frac{x - x_0}{\sigma_x} \right)^2 + \left( \frac{y - y_0}{\sigma_y} \right)^2 \right] \right\} \quad (2.19)$$

with the background Intensity  $I_{\text{bg}}$ , the amplitude  $I_a$  and the widths in both directions  $\sigma_x$  and  $\sigma_y$  of the Gaussian function.  $x_0$  and  $y_0$  define the Gaussian center and thus result in the local position of the imaged objects.

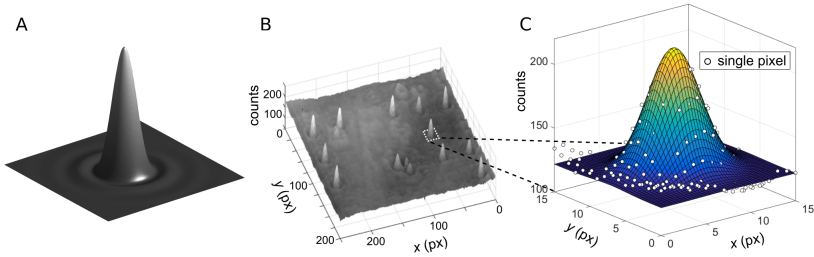


**Figure 2.6.:** A) Calculated two dimensional Airy pattern of a diffraction-limited object. The first ring of the Airy disc is already difficult to observe. B) 3D representation of the iSCAT image in Fig. 2.5B highlighting the point spread function (PSF) of the 60 nm Au NPs as sharp peaks. C) 2D Gaussian fit of one particle to obtain the center of the PSF for sub-diffraction localization.

The PSF on the image detector however, does not appear as perfect as in Fig. 2.6A. In reality, the intensity signal of the object is distributed over separated pixels and overlaid with the background noise of the system. Such a real image and the corresponding Gaussian fit can be seen in Fig. 2.6B and C. The localization accuracy  $\delta x_0$  and  $\delta y_0$  for a Gaussian fit on images with a pixel size  $a$ , a total number  $N$  of collected photons in the PSF and an estimated r.m.s noise  $b$ , was derived by Thompson *et al.* as [139]

$$\delta x_0 = \sqrt{\left( \frac{\sigma_x^2}{N} + \frac{a^2}{12N} + \frac{8\pi\sigma_x^4 b^2}{a^2 N^2} \right)}. \quad (2.20)$$

This equations points out that the localization accuracy highly depends on the SNR of the system and that a high SNR is required for precise tracking. The SNR for the GIE trapping systems combined with iSCAT detection is depended on the particles size and the material used to fabricate the devices (see Chapter 3 and 5). The localization accuracy for the different systems and particle sizes were analyzed and can be found in Appendix A.

## 2.8. Diffusion in a harmonic potential

To characterize the performance of the devices such as trapping strength, trapping time and potential depth, the motion of the particles in two dimensions is tracked between each acquired frame, which results in the trajectories of the particles. The diffusive motion of an object in solution is described by the mean-square displacement (MSD)  $\langle [\Delta x(\Delta t)]^2 \rangle$  in each direction  $x$ ,  $y$  and  $z$ . For a freely diffusing object, the MSD is linearly proportional to the lag time  $\Delta t$  and the diffusion coefficient  $D$  and e.g. in direction  $x$  ( $\text{MSD}_x$ ) is defined as

$$\langle [\Delta x(\Delta t)]^2 \rangle = 2D\Delta t \quad (2.21)$$

and for the two dimensional case ( $\text{MSD}_r$ )

$$\langle [\Delta r(\Delta t)]^2 \rangle = \langle [\Delta x(\Delta t)]^2 \rangle + \langle [\Delta y(\Delta t)]^2 \rangle = 4D\Delta t. \quad (2.22)$$

The diffusion coefficient  $D$  describes the mobility of the object and is specific for its size and shape and surrounding media. It is defined for a spherical particle in liquid by the Stokes-Einstein-equation as [42]

$$D = \frac{k_B T}{3\pi\eta d}, \quad (2.23)$$

where  $\eta$  is the dynamic viscosity of the liquid and  $d$  the diameter of the particle. For a confined particle in a trap however, the diffusion is restricted to an area defining the edges of the confinement. The  $\text{MSD}_r$  thus reaches a plateau  $\langle [\Delta r]_p^2 \rangle$  for large lag times which can be modeled as [141]

$$\langle [\Delta r(\Delta t)]^2 \rangle = \langle [\Delta r]_p^2 \rangle \left( 1 - A_1 \exp \left[ -A_2 \frac{4D\Delta t}{\langle [\Delta r]_p^2 \rangle} \right] \right), \quad (2.24)$$

with the fit parameters  $A_1$  and  $A_2$ . In a harmonic potential, such as induced by traps realized in this project, this plateau of the  $\text{MSD}_r$  is correlated to the radial stiffness  $k_r$  (the strength of particle confinement) of the trap given by:

$$\langle [\Delta r]_p^2 \rangle = \frac{4 k_B T}{k_r}. \quad (2.25)$$

The analysis of the trap stiffness  $k_r$  provides an important value of understanding the lateral trap behavior of the devices. It is dependent on key

parameters such as ionic strength of the solution, particle and surface charge density and of the trap and nanofluidic geometries.

In addition to the stiffness  $k_r$ , two more parameters are important in describing the potential landscape of the traps: (i) the mean residence time  $\bar{\tau}_K$ , known as the Kramers time and defined as the average time a particle dwells inside a trap before escaping and (ii) the potential depth  $Q$  of the trap. For a harmonic potential, the Kramers time and the potential depth are related as [142, 143]

$$\bar{\tau}_K \cong \tau_R e^{\frac{Q}{k_B T}} \quad (2.26)$$

where  $\tau_R$  is the relaxation time in the potential well (the time a non-trapped particle would take to freely diffuse across a distance corresponding to the width of the potential well). The Kramers time  $\bar{\tau}_K$  can be determined by recording the trapping and escaping events of many particles which results in a residence time probability distribution as a function of residence time  $\tau$  of the form

$$p(\tau) = A e^{\frac{-\tau}{\bar{\tau}_K}}. \quad (2.27)$$

The relaxation time  $\tau_R$  in a harmonic potential is related to the trap stiffness  $k_r$  and the diffusion coefficients  $D$  of the particles as [7, 144]

$$\tau_R = \frac{k_B T}{D k_r}. \quad (2.28)$$

To obtain the potential depths  $Q$  of the traps and thus answer the question of stable trapping ( $Q > k_B T$ ), both  $k_r$  and  $\bar{\tau}_K$  are needed which can be experimentally measured.

## 2.9. Influential device parameters on the trap performance

The trapping stiffness and residence time of the object depend on key parameters such as the ionic concentration of the buffer solution  $c_0$ , the surface charge density of the nanofluidic walls  $\sigma_s$  and object  $\sigma_p$ , the size of the object  $d$ , the nanofluidic channel height  $h_c$ , and the width  $w_p$  and depth  $h_p$  of the trap. These parameters can be tuned to obtain an optimized trapping behavior for a known object property or pushed to the limits for trapping ever smaller objects. However, if these parameters are known and kept constant in the system, the GIE trapping devices can be used as sensitive sensors to examine unknown parameters such as the size and charge of the trapped objects [7, 34], the ionic concentration of the buffer solution or the electric charge of the device surface or object [123]. This can be either achieved with the help of numerical simulations or by fully testing the benchmarks of the system with known parameters in advance.

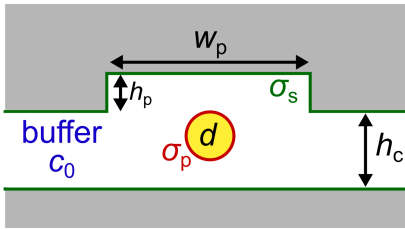


**Figure 2.7.:** Schematic of the parameters that influence the trap performance. The ionic concentration of the buffer solution  $c_0$ , the surface charge density of the nanofluidic walls  $\sigma_s$  and object  $\sigma_p$ , the size of the object  $d$ , the nanofluidic channel height  $h_c$  and the width  $w_p$  and depth  $h_p$  of the trap.

### Ionic concentration of the buffer solution

The electrostatic potential near the charged device and object surface in solution decays exponentially with the Debye length (see Eq. 2.8). The Debye length is proportional to the ionic concentration of the buffer solution as  $1/\sqrt{c_0}$  (see Eq. 2.9). Thus, increasing the concentration of ions in the solution leads to a screening of the surface charges, which weakens the trap stiffness and reduces the trapping time of the particles. The calculated Debye length (where the electrostatic potential has dropped  $e^{-1}$  of the original value) for different concentrations of monovalent salt solutions is presented in Tab. 2.1. For a 0.1 mM monovalent salt concentration, which was mainly used in this work, the Debye length is on the order of 30 nm. At this concentration, strong and stable trapping was observed. However, biological conditions start at a salt concentration of about 30 mM where the Debye length has dropped to only about 2 nm. Achieving stable trapping at these conditions requires devices with low nanofluidic channels heights  $h_c$  or an increased surface charge

density  $\sigma_s$ . The influence of different ionic strength solutions on the trapping stiffness and trapping time is demonstrated in Chapter 4. New GIE trapping devices with a tunable channel height that could be used to trap in higher salt concentrations are introduced in Chapter 5.

$c_0$	$\kappa^{-1}$
100 $\mu\text{M}$	30 nm
1 mM	10 nm
10 mM	3 nm
30 mM	1.8 nm
100 mM	1 nm
1 M	0.3 nm

**Table 2.1.:** Debye length for different monovalent salt concentrations

### Surface charge density of the nanofluidic walls

According to the Debye-Hückel (Eq. 2.7) and Grahame equation (Eq. 2.8), the electrostatic potential is linearly proportional to the surface charge density  $\sigma_s$ . Hence, increasing  $\sigma_s$  of the nanofluidic channels leads to a stronger trapping and longer residence times of the trapped objects. This can be achieved by treating the surface chemically using NaOH and HCl solution [106] or by the adsorption of multilayer of charged molecules such as polyelectrolytes [145–148]. Further, modifying the surface with only one positive layer leads to a charge reversal and thus the ability to trap positively charged objects [125].

### Size and surface charge density of the object

Similar to  $\sigma_s$ , an increased surface charge density of the trapped object  $\sigma_p$  results in a higher net charge of the object and thus stronger trapping and longer trapping times. If  $\sigma_p$  of an object is constant, larger objects are trapped stronger and longer due to a higher net charge and closer distance to the nanofluidic channel walls which leads to a higher repulsion of the walls of the channel and thus deeper potential. This behavior is demonstrated and discussed in Chapter 5.

### Nanofluidic channel height

The nanofluidic channel height  $h_c$  is the prime geometrical design parameter to tune the trapping strength for smaller particles and, if changeable, to manipulate the device performance during the experiment [103]. As demonstrated in the model of two separated surfaces in Fig. 2.3, decreasing  $h_c$  results in deeper potential wells  $Q$  and thus longer residence times according

to Eq. 2.26. Further, it renders the trap to a narrower potential and thus confines the particle stronger as will be described and discussed in Chapter 5 and 6.

### Trap geometry

The width  $w_p$  and depth  $h_p$  of the trap are parameters that are set during the fabrication of the devices and can not be changed during the experiment. However, since in the chip-based approach of electrostatic trapping several millimeter long nanofluidic channels are typically implemented, lattices of thousands different trap designs, especially different trap widths, can be fabricated within one device. For a circular trap design, increasing  $w_p$  leads to a deeper potential, up to a certain limit of  $w_p \sim h_c$  where a plateau of the potential is reached (see Chapter 5), and thus longer trapping times of the object. On the other hand, a larger width weakens the trap stiffness, which confines the object less and increases the probability that multiple objects enter the trap. A key benefit of chip-based GIE trapping devices is that the shape of the trap is not limited to circular pockets. Instead, rectangular shapes are possible, which leads to the angular trapping and manipulation of nanorods [121], or long slits or grids, which can be interesting for the direct observation of particle diffusion in 1D and 2D systems (see Chapter 7).

The trap depth  $h_p$  is another important trap parameter to set. Increasing the  $h_p$  results in deeper potentials and thus longer trapping times as well as stronger confinement of the objects. However, there is an upper limit of roughly  $h_p \sim w_p$ , where a deeper trap does not significantly influence the potential landscape anymore. Even if the trap would have an open end as described by Tae Kim *et al.*, which used a nanopipette as trap, the potential depth would remain static at about this limit [103]. As a result,  $h_p$  is often a trade-off between the different shapes and widths of the fabricated traps, since it is set during the RIE etching process and thus for each chip uniform indifferent of the trap type. As a rule of thumb, a trap depth of  $h_p = h_c/2$  was found to give the best trapping results for many trap shapes and sizes.





## **Glass-based geometry-induced electrostatic trapping devices for improved scattering contrast imaging of nano-objects**

*The following section has been published in:*

Microelectronic Engineering, Volume 145, 43-48, 2015  
<http://dx.doi.org/10.1016/j.mee.2015.02.035>

### **Glass-based geometry-induced electrostatic trapping devices for improved scattering contrast imaging of nano-objects**

**Michael Adrian Gerspach<sup>a,b,c,\*</sup>, Nassir Mojarad<sup>b,d</sup>, Thomas Pfohl<sup>a,c</sup>, Yasin Ekinici<sup>a,b</sup>**

<sup>a</sup> *Swiss Nanoscience Institute, 4056 Basel, Switzerland*

<sup>b</sup> *Laboratory for Micro- and Nanotechnology, Paul Scherrer Institut, 5232 Villigen, Switzerland*

<sup>c</sup> *Department of Chemistry, University of Basel, 4056 Basel, Switzerland*

<sup>d</sup> *Nanotechnology Group, ETH Zurich, 8803 Rüschlikon, Switzerland*

\* Correspondence: [michael.gerspach@unibas.ch](mailto:michael.gerspach@unibas.ch)

**Keywords:** Geometry-induced electrostatic trapping, Interferometric scattering detection (iSCAT), Nanofluidic systems, Nano object trapping, Glass-glass bonding, Glass-based GIE trapping devices

**Abstract**

Trapping of micro- and nano-objects in solution is of great scientific interest in various fields. One method of trapping and detecting objects smaller than 100 nm is the combination of geometry-induced electrostatic (GIE) trapping devices and interferometric scattering detection (iSCAT). In GIE trapping, charged nano-objects are confined in a nanofluidic system that hosts topographically modified surfaces, resulting in electrostatic potential wells. We observe optical limits of detecting gold nanoparticles smaller than 60 nm because of the high reflection of the strong background signal in current silicon-based GIE trapping chips. The high reflection rapidly leads to overexposure of the camera detector and thus limits the incident laser power. In this work, we introduce new functional geometry-induced electrostatic devices fabricated from glass substrates. Due to the reduced reflection at the water-glass interface compared to the silicon-based devices, higher incident laser power can be used to image the nano-objects resulting in higher contrast as well as signal-to-noise ratios (SNR) of the gold nanoparticles. Using glass-based GIE trapping devices, significant SNR increases are achieved in comparison to that of silicon-based devices. These improvements enable the detection of much smaller nanoparticles and thereby studies on their trapping, as well as further investigation in nanofluidic systems.

### 3.1. Introduction

Contact-free trapping of nano-objects is of broad interest for a range of disciplines such as biotechnology, biophysics and material science. Methods such as optical- [49, 50, 56], magnetic- [82], and acoustic- [95] tweezers or electro- and dielectrophoresis [86] are successful methods that have been demonstrated. However, these methods come with the limit of the restoring force,  $F_{\text{res}} \propto \alpha |\nabla E|^2$ , where  $|\nabla E|$  is the field gradient, and  $\alpha$  is the polarizability of the trapped object.  $\alpha$  vanishes in the limit of small particles or when the material properties are similar to the surrounding media. Moreover, to get a stable trapping of small nano-objects, large gradients and fields have to be applied. In addition to often demanding setups, large fields might damage the object of interest. A promising candidate for trapping objects smaller than 100 nm in fluid without any externally applied fields is geometry-induced electrostatic (GIE) trapping [7, 17, 103, 121]. Contrary to the mentioned trapping methods,  $F_{\text{res}}$  in electrostatic trapping is proportional to the object charge rather than to the size and mass. Therefore, this method has a great potential in polymer physics [149, 150], protein and DNA analysis [151], and as a sample environment for single protein free electron laser (FEL) experiments. Altering surface topology of nanochannels in silicon-based chips was used in a first realization of GIE traps [17]. It was shown that by creating localized three-dimensional potential wells, negatively charged nano-objects can be trapped by pockets or be confined to small grooves due to the suppression of their Brownian motion. Gold nanoparticles (NPs) down to 80 nm [7] and fluorescently labeled vesicles in suspension could be confined in electrostatic traps by falling into local potential wells for a time period of several seconds to hours [17, 120]. By analyzing the motion of the trapped gold NPs, the size of single gold NPs could be determined in nanometer precision as well as their net carrying charge [120]. Furthermore, orientation-dependent trapping of silver rods could be achieved using this method [121]. A major advantage of GIE trapping is that the potential depth depends only on the charge but not on the mass or size of the nano-object. The electrostatic potential depth can be adjusted by altering the geometry of the chip or by changing the concentration of the buffer solution. A modification of this method is scanning-aperture trapping [103], a tweezing equivalent of GIE traps. This method has the advantage of altering the trap potential depth by approaching or releasing the aperture during the experiment and having the option of  $x$ -,  $y$ -position scanning, while it is limited to a single trap and a more complex experimental setup.

In most of these studies, charged gold NPs are the prime approach used for characterizing the performance of the electrostatic traps. In contrast to fluorescence labeled molecules, quantum dots (QD) or silver NPs, gold NPs

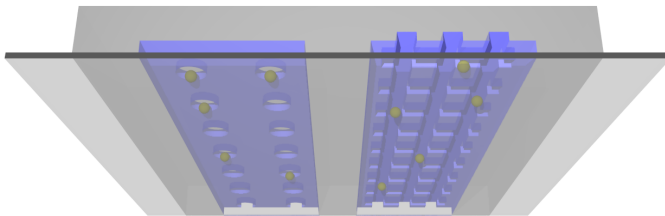


**Figure 3.1.:** Schematic of a glass-based geometry-induced electrostatic trapping device. Nano-objects are trapped by the fine structures in the microchannel.

are not limited by photobleaching over time or oxidization and are not limited in time resolution for tracking particles by optical saturation and photoblinking [11]. Due to the strong plasmon resonance peak of gold NPs in the water, in the wavelength range of  $\lambda = 530 - 550$  nm, they exhibit a high scattering signal. However, the detection of gold NPs becomes increasingly difficult with decreasing particle diameter  $D$ , since the scattering intensity scales with  $D^6$  [152]. To overcome this drawback, a new method was introduced using coherent light illumination with an interferometric detection scheme [15, 18–20]. This technique, called interferometric scattering detection (iSCAT), is based on the interference between the scattered light of the particle and a reference beam. Very small objects can be imaged by iSCAT at high speeds and with nanometer precision, since the detected signal of objects scales  $D^3$  [18–20]. Using this method, fixed gold NPs of 5 nm size at a glass-oil interface using supercontinuum white light [18] and at a glass-water interface using confocal scanning iSCAT were detected [19]. Due to its high sensitivity in the phase difference between the reference and scattered beam and the consequential contrast change in axial movements of the particles, iSCAT was used to track 80 nm and 100 nm gold particles with less than 5 nm localization precision in three dimensions at an acquisition rate of 1 kHz [17, 120]. The first concrete application of iSCAT for single biomolecule tracking was shown by Kukura et al. [20]. By simultaneously detecting the fluorescence signal of a quantum-dot labeled virus and its center of mass by iSCAT, it was possible to track the position and orientation of the virus moving along a lipid bilayer [20]. These studies show the tremendous potential of iSCAT for detection with high sensitivity and for fast imaging with high localization precision.

In this work, we introduce an improved nanofluidic GIE trapping device for better detection of small particles. We focus on the optical detection of these small objects and show the detection of gold NPs down to 40 nm. In this regard, we modify the nanofluidic system to suppress the high reflections

and thus limited incident laser beams occurring in silicon-based GIE trapping devices using glass-based chips (see Fig. 3.1).

### 3.2. Theory

The basic principal of iSCAT for the detection of small objects at the water-glass interface is illustrated in Fig. 3.2A. The incident beam  $E_i$ , focused to the location of the sample, is reflected at the water-glass interface with the reflected beam  $E_{r1}$  and scattered from the particle with the scattered field  $E_s$ . The scattered field at the detector is described as  $E_s = s E_i$  where  $s = |s| e^{i\varphi}$  scales with the polarizability  $\alpha$  of the particle [18],

$$s(\lambda) = \eta \alpha(\lambda) = \eta \epsilon_m(\lambda) \frac{\pi D^3}{2} \frac{\epsilon_p(\lambda) - \epsilon_m(\lambda)}{\epsilon_p(\lambda) + 2 \epsilon_m(\lambda)} \quad (3.1)$$

with the complex dielectric constants of the particle  $\epsilon_p(\lambda)$  and the medium  $\epsilon_m(\lambda)$  and the proportionality constant  $\eta$ . The total field at the detector  $E_{\text{det}}$  is given by the sum of the scattered and reflected fields,  $E_{\text{det}} = E_{r1} + E_s$ . The corresponding intensity  $I_{\text{det}}$  can be written as [15, 17–20],

$$I_{\text{det}} = |E_r + E_s|^2 = |E_i|^2 \{r^2 + |s|^2 - 2r|s| \sin \varphi\} \quad (3.2)$$

where the first term scales with the reflected field  $r^2$ . This term represents the background intensity, which arises in the case of the gold NP on the glass surface, from the reflected beam at the glass-water interface,  $E_{r1}$ , depicted in Fig. 3.2A. The second term, proportional to  $|s|^2$ , represents the purely scattering signal, which scales with  $D^6$  and thus becomes smaller than the noise of the field reflectivity for very small particles. The last term  $2r|s| \sin \varphi$  is the interference of the reflected and the scattered field and scales with  $D^3$ . For very small particles, this term dominates the pure scattering signal, since it is multiplied by the reflected field  $r$ . A significant advantage of iSCAT compared to, e.g., fluorescence microscopy is that at low intensities the incident beam power can be simply increased since the scattered field of the particle increases with the incident beam. Fluorescence microscopy is here limited by the fluorescence saturation of the dye and thus longer integration times.

The above argument is true for particles sitting on a glass surface (Fig. 3.2A) due to the low reflectivity of the glass-water interface. Here, the background intensity,  $E_r$ , originates from the reflected field at the glass-water interface  $E_{r1}$ , that according to Fresnel's law, has a low reflectivity of  $R = 0.2\%^1$ . For current silicon-based GIE trapping devices (Fig. 3.2B), on the other hand,

<sup>1</sup>Using Fresnel's law for an incident light angle of  $90^\circ$ ,  $R = \frac{n_2 - n_1}{n_2 + n_1}$ , and the refractive indices of  $n_{\text{H}_2\text{O}} = 1.33$ ,  $n_{\text{borfloat}} = 1.47$ ,  $n_{\text{SiO}_2} = 1.55$  and  $n_{\text{Si}} = 4.15$

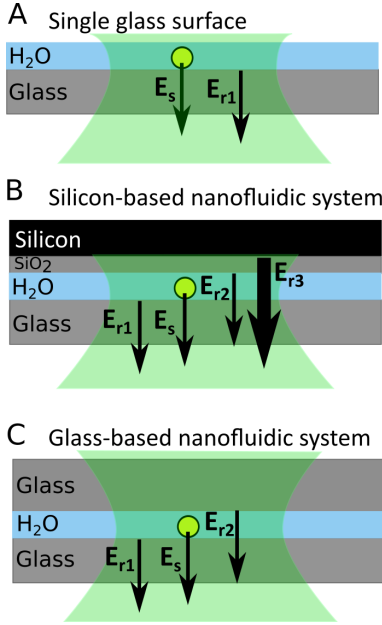


**Figure 3.2.:** Schematics of the three nanofluidic devices showing the path of the incident beam, the field scattered from the nano-object and reflected beam at the different interfaces. A) Nano-object on a single wetted glass surface, B) current silicon-based nanofluidic systems with a high reflection at the Si-SiO<sub>2</sub> interface, C) new glass-based nanofluidic systems for GIE trapping with reduced reflection of the incident beam.

this is not valid since the background intensity results from the sum of the reflected fields from the glass-water interface  $E_{r1}$ , the water-SiO<sub>2</sub> interface  $E_{r2}$  and the SiO<sub>2</sub>-Si interface  $E_{r3}$  with a reflectivity of  $R_1 = 0.2\%$ ,  $R_2 = 0.5\%$ , and  $R_3 = 21\%$  respectively. In this configuration, the incident light power cannot be increased arbitrarily since the detector quickly saturates due to the highly reflecting SiO<sub>2</sub>-Si interface. For very small particles, the background intensity term in Eq. 3.2 overwhelms the pure scattering signal and even the interferometric term due to the 100-fold increase compared to the glass-water interface. To overcome these constraints, we have developed glass-based GIE trapping devices, schematically shown in Fig. 3.2C. Here, the background intensity results mainly from the glass-water and water-glass interfaces. In addition to the removal of the highly reflecting SiO<sub>2</sub>-Si interface, the reflected field  $E_{r2}$  could be decreased from 0.5% (water-SiO<sub>2</sub> interface) in silicon-based devices to 0.2% (water-glass interface) in the glass-based devices. The reflected field at the glass-air interface (Fig. 3.2C) can be equally neglected in the glass-based devices, as the reflected field at the water-air interface of the single glass (Fig. 3.2A) because of the highly diverged incident beam of the high NA objective of 1.3: These interfaces are large distances away from the focused beam (several 100  $\mu\text{m}$ ).

### 3.3. Material and Methods

#### 3.3.1. Experimental setup

The iSCAT setup was built using a 300 mW diode-pumped solid-state laser (MGL-III-532, CNILaser) with  $\lambda = 532$  nm, which is near the plasmon resonance peak of the gold NPs. The beam was scanned over the sample using an  $x$ -,  $y$ -mirror deflection system (GVS002, Thorlabs Inc.) running at 1 kHz and focused by a  $100\times$ , 1.3 NA oil-immersion objective and an additional  $1.5\times$  tube lens (Leica). The collected scattered and reflected beams were imaged on a CMOS camera (MV-D1024-160-CL-12, Photon Focus) at an exposure time of 10 ms and an acquisition frequency of 85 Hz.

#### 3.3.2. Fabrication of silicon-based GIE trapping devices

The GIE trapping devices were produced from silicon substrate as sketched in Fig. 3.3A. The chips were fabricated using electron beam lithography (Vistec EBPG 5000 Plus) and reactive ion etching (RIE) (Oxford 100, Ar 38 sccm, CHF<sub>4</sub> 12 sccm, 100W) starting from a 400-nm-thick grown silicon dioxide layer on a 525- $\mu$ m-thick p-typed silicon wafer. As a first step, 25 nm of chromium was evaporated on the silicon dioxide, which functions as a hard mask for e-beam exposure. Then, parallel fluidic slits of 5 – 20  $\mu$ m width and 5 mm length were exposed in PMMA (950k, 4% ethylacetate) using e-beam lithography and developed in MIBK:IPA (1:3, 60 s). After etching the slits into the chromium hard mask (BMP Plasmatechnology GmbH, O<sub>2</sub>:Cl<sub>2</sub> with a rate of 1:5) and removing PMMA in acetone, the slits were etched 90 – 200 nm deep using RIE. The remaining Cr layer was subsequently removed using chromium etchant (Chrome ETCH No 1, Technic). This process was repeated to etch the finer nanowells, circle pockets or rectangular slits with a diameter or width of 100 to 500 nm, into the surface of the microchannels. The final potential depth of the wells resulted in the variation of the microchannel height, well depth and well lateral extension [17, 116]. After processing, the wafer was diced into  $5\times 5$  mm<sup>2</sup> chips covered by a protection resist (Shipley 1813). To reduce any defects during bonding, the chips and cover glasses were cleaned in freshly-made piranha solution (H<sub>2</sub>SO<sub>4</sub>(%):H<sub>2</sub>O<sub>2</sub>(%) = 2:1) for 30 min, rigorously rinsed in DI water, and dried under a nitrogen stream. The chips were finally irreversibly bonded to a borosilicate cover glass (PlanOptik), with an adjusted thermal expansion coefficient to silicon, using anodic bonding (SUSS MicroTech BA6/8) at 450°C with a voltage of -600 V. The cover glass sealed the fluidic channels and provided optical access to the sample.

### 3. Glass-based geometry-induced electrostatic trapping devices for improved scattering contrast imaging of nano-objects

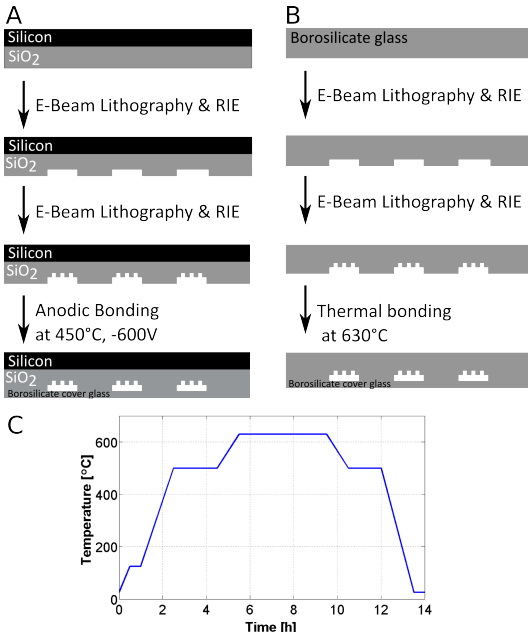


**Figure 3.3.:** A) Fabrication of the current silicon-based GIE trapping devices using electron beam lithography and anodic bonding, B) fabrication of new glass-based GIE trapping devices made by thermal bonding, C) Temperature cycle and annealing rate of the thermal bonding process.

#### 3.3.3. Fabrication of glass-based GIE trapping devices

The fabrication of the glass-based GIE trapping devices is schematically shown in Fig. 3.3B. The first two fabrication steps were identical to that of the fabrication of the silicon-based devices except for the replacement of the silicon wafer by a 200- $\mu\text{m}$ -thick borosilicate glass wafer (PlanOptik). After dicing the finished etched glass wafer into smaller 5 $\times$ 5 mm<sup>2</sup> chips, the chips and borosilicate cover glasses were cleaned in piranha solution for 10 min, rigorously rinsed in DI water and activated in 29% ammonium hydroxide solution at 35°C for 40 min [153]. After another rinsing with DI water and nitrogen blow-drying, the glass chip and cover glass were instantly aligned and pressed together at a pressure of 390 kN/m<sup>2</sup> for about 24 hours. Finally, the pressed devices were thermally bonded in a controllable furnace (Process Products Corporation) without applying any pressure by annealing at 630°C for 4 hours at the ramp rate and time cycle shown in Fig. 3.3C. We needed extensive optimization of the ramp rate and time cycle in order to achieve successful and reproducible bonding processes.



### 3.3.4. Sample preparation

Gold NPs with diameters of 40, 60, and 80 nm were purchased from BBI Solutions (EM.GC40/60/80). The 60 and 80 nm gold particles were centrifuged at 2000 rpm for 20 min and re-suspended in DI water (18 M $\Omega$ ) three times to exchange buffer solution and create a dense solution of gold NPs of about  $10^{11}$  particles/ml. The 40 nm gold particles were centrifuged only once at 1500 rpm for 20 min to create a dense solution of about  $10^{11}$  particles/ml.

## 3.4. Results and Discussion

### 3.4.1. Contrast and SNR comparison of silicon- and glass-based nanofluidic systems.

Our current work uses gold NPs and iSCAT to advance geometry-induced electrostatic trapping for smaller objects. In silicon-based devices we find limits in optical detection of gold NPs smaller than 60 nm because of the high background noise and low signal of the particles. This is caused by the high reflection of the Si-SiO<sub>2</sub> interface of the GIE trapping devices, which rapidly leads to overexposure of the camera detector and thus limits the incident laser power.

Spherical NPs in tightly focused electromagnetic beams have been theoretically studied [154], and the formalism has been adapted to the case of the particle near a reflecting surface [120]. For a gold NP trapped by a pocket, the intensity at the detector can be written as

$$I(x, y, z)_{\text{det}} = I_{\text{bg}} + I_{\text{a}}(x, y) \cos \Delta\varphi(z) + I_{\text{poc}} \quad (3.3)$$

where  $I_{\text{bg}}$  is the background intensity,  $I_{\text{poc}}$  is the intensity of the fixed pocket,  $I_{\text{a}}$  is the amplitude of the signal of the particle, and  $\cos \Delta\varphi(z)$  is the modulation of the iSCAT signal that depends on the axial particle location. In order to avoid the  $I_{\text{poc}}$  subtraction procedure [120] which would increase localization errors in the low signal regime, we recorded the gold NPs in microchannels without pockets to create comparable conditions on all NPs for contrast and signal-to-noise ratio (SNR) characterization. The detector intensity can be then rewritten as

$$I(x, y, z)_{\text{det}} = I_{\text{bg}} + I_{\text{a}}(x, y) \cos \Delta\varphi(z) \quad (3.4)$$

and the contrast  $K$  can be defined as the amplitude of the particle over the background:

$$K(x, y, z) = \frac{I_{\text{a}}(x, y) \cos \Delta\varphi(z)}{I_{\text{bg}}}. \quad (3.5)$$

In a shot-noise-limited experiment, the SNR is proportional to the contrast and to  $N^{1/2}$ , where  $N$  is the number of photons detected by the camera. The resulting iSCAT SNR can be written as [15]:

$$\text{SNR} = \frac{\text{iSCAT signal}}{\text{background fluctuation}} \propto \text{contrast} \cdot \sqrt{N}. \quad (3.6)$$

Single gold NPs in water solution in silicon-based devices of 40, 60, and 80 nm size and their contrast cross-sections are shown in Fig. 3.4A. The 80 nm particle is clearly detected as it can be seen as a Gaussian dip in the contrast cross-section. The observed dip, i.e. negative contrast, is a clear indication of the destructive interference of the reflected and scattered field. By analyzing more than 400 gold NPs with a diameter of 80 nm in silicon-based devices, we obtained a mean contrast of  $K_{\text{Si},80} = 0.20$  and a mean  $\text{SNR}_{\text{Si},80} = 30$  (see Fig. 3.5). The contrast of 60 nm particles is decreased to  $K_{\text{Si},60} = 0.10$  and the  $\text{SNR}_{\text{Si},60} = 24$  due to lower scattering from the NPs. For NPs smaller than 60 nm, the outlines are smeared in the background of the image, which makes the localization almost impossible as seen in Fig. 3.4A. The simple reason for this is the low contrast of the particle of  $K_{\text{Si},40} = 0.06$ . Here the background inhomogeneity (the standard deviation in  $I_{\text{bg}}$  fluctuations in a single image) is in the range of the amplitude  $I_a$  of the particle. With a  $\text{SNR}_{\text{Si},40} = 13$ , however, the movements of the 40 nm particle can be still detected since the background fluctuation over time is stable in all experiments with about 0.8 counts of an 8-bit imaging system.

Eq. 3.6 demonstrates that the SNR is proportional to  $N^{1/2}$ . As a result, increasing the number of photons incident on the particle will also increase the SNR. However, this is not feasible for silicon-based GIE trapping devices. In the silicon-based devices, the high reflection of the Si-SiO<sub>2</sub> interface quickly saturates the camera and consequently limits the incident laser beam that can be used, which leads to lower scattered light from the particle. The images of the gold NPs in the silicon-based devices were recorded at an output laser power of maximum 50  $\mu\text{W}$  for homogenous image exposure. Further increase of the laser power resulted in an overexposure of the background.

To increase the potential of iSCAT imaging, nanofluidic systems made from glass were used for gold NPs of 40, 60, and 80 nm in diameter as shown in Fig. 3.4B and C. Here, two different modes were observed. By slightly tuning the focus of the beam, the contrast of the particles can be changed from a negative to a positive mode. This effect clearly indicates the interferometric nature of the scattering detection, since the final signal is a result of constructive (bright) or destructive (dark) interference of  $E_r$  and  $E_s$ . For a particle at a certain axial height, there is a systematic phase difference ( $\Phi_{\text{sys}}$ ) between

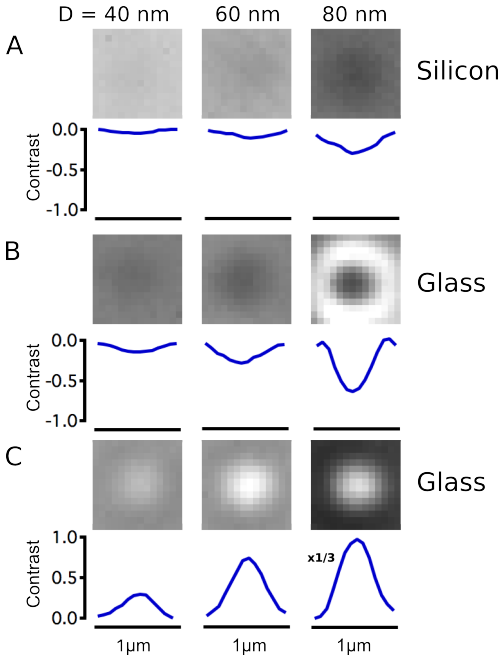


**Figure 3.4.:** iSCAT images of 40, 60 and 80 nm gold particles freely moving in A) silicon based nanofluidic systems, B) glass-based nanofluidic systems with negative contrast and C) glass-based nanofluidic systems with positive contrast. The line-out from the center of each image is plotted in the graph below it. The contrast profile of the 80 nm gold particle in C) was multiplied by 1/3 for better visualization.

these two fields, which directly influences the detected contrast [120]. In the case of glass-based devices, this phase difference becomes sensitive to the beam-focus position and therefore the particle contrast rapidly changes by axial movement of the sample. For the silicon-based devices, the contrast change is less sensitive, since the main reflection from the Si-SiO<sub>2</sub> interface (Fig. 3.2B) is several hundred nanometers away from the focus, where the particle is levitating.

In Fig. 3.4B, negative contrast images of gold NPs are shown. For all cases, significant contrast and SNR enhancement in the glass-based devices were observed compared to the silicon-based devices. It was possible to detect 40 nm gold particles, which showed an even higher contrast than 60 nm gold particles in silicon-based devices. The contrast of the 60 and 80 nm particles was increased by a factor of 3 whereas the SNR was increased by a factor of 2 for the 60 nm gold particles and by a factor of 4.5 for the 80 nm gold particles. The enhanced contrast could be achieved by increasing the laser power up to 1 mW. The saturation limit of the glass-based systems was reached at an output laser power of 1.2 mW where an overexposure of the background was reached.

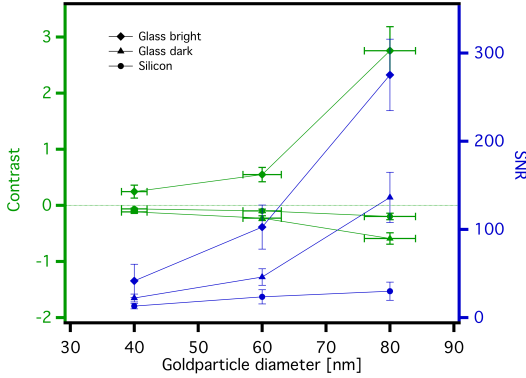


**Figure 3.5.:** Mean contrast and mean SNR measurements of 40, 60 and 80 nm gold particles in different nanofluidic systems. X-error bars highlight the particles size error given by the distributor. Y-error bars highlight the standard deviation of the contrast and SNR of untrapped particles moving in the channels. A minimum of 400 particles was analyzed for every mean contrast and SNR measurement. The background fluctuation noise was stable from  $\sim 0.5$  counts in glass-based devices to  $\sim 0.8$  counts in silicon-based devices of an 8-bit imaging system.

An even higher contrast and SNR of the particles could be achieved by a positive contrast as shown in Fig. 3.4C and Fig. 3.5. Comparing the absolute contrast of the 80 nm particles in the glass-based devices with the 80 nm particles in the siliconbased devices, an increased contrast by a factor of 14 was achieved. This high contrast ( $K > 1$ ) indicates that the detected signal comes not only from the interference between the scattering and reference beam, but also originates from pure scattering of the particle. For the 80 nm gold particles an  $\text{SNR}_{\text{Glass},80} = 275$  was measured which is an increase of an order of magnitude compared to 80 nm gold particles in silicon-based devices. Even more impressive, the detected 40 nm gold particles in the glass-based devices showed a higher SNR than the 80 nm gold particles in the silicon-based devices. The higher error bars in contrast and SNR for glass-based GIE trapping devices result from the higher sensitivity of the lateral position of the particles. Indeed, in glass-based devices this high SNR provides the possibility for particle tracking with higher localization precision in  $x$ ,  $y$ , and  $z$  direction [120]. The GIE trapping devices were slightly modified in channel height for the different particle diameters. For 40, 60, and 80 nm gold particles a channel height of 100, 130, and 160 nm was used, respectively.

### 3.4.2. Trapping of gold nanoparticles in glass-based GIE trapping devices

To show the functionality of the glass-based GIE trapping devices, we trapped 60 nm gold particles as shown in Fig. 3.6. The particles were confined in pockets of 100 nm in diameter, which are arranged in a square array with a periodicity of 3  $\mu\text{m}$ . The microchannel height was 130 nm and the depth of the pocket was 70 nm. We expect the surface charge density, and thus the device characteristics to be unchanged since the surface charge density  $\sigma$  of grown  $\text{SiO}_2$  and borosilicate glass is about 1  $\text{mC}/\text{m}^2$  at neutral pH [107, 155]. In Fig. 3.6, the dashed arrows highlight particles undergoing free Brownian motion in the microchannel after escape or before getting trapped (solid arrows) in the well-defined 100 nm pockets. A stable trapping for several seconds to minutes could be achieved using the 60 nm gold particles at low salt concentration of  $\sim 0.1$  mM.

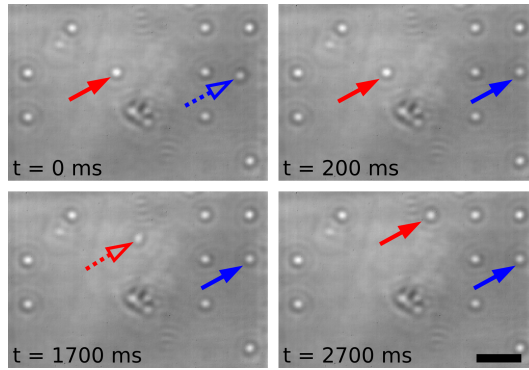


**Figure 3.6.:** Image sequence of trapped 60 nm gold particles in a new generation glass-based GIE trapping device with a channel height of 130 nm. The particles were trapped in 100 nm wide pockets at low salt concentration. Dashed arrows highlight freely moving particles that are escaped or trapped (solid arrows) during the image sequence. The scale bar is 3  $\mu\text{m}$ .

## 3.5. Conclusion

In this work, we introduced the fabrication of a new generation of geometry-induced electrostatic trapping devices based on thermal-bonded glass-based chips. Due to a decreased background reflection at the glass-water interface using glass-based chips compared to the high reflection at the  $\text{Si-SiO}_2$  interface of silicon-based GIE trapping devices, the contrast of 40, 60, and 80 nm gold particles could be increased by an order of magnitude. The high contrast and

SNR achieved with glass-based GIE trapping devices give the possibility to detect gold NPs down to 40 nm with high localization precision and to observe their trapping dynamics. We foresee using the glass-based GIE trapping devices for trapping and detection of smaller gold NPs and biomolecules, such as DNA or large proteins using iSCAT. Finally, the devices will provide better SNR for fluorescence experiments since the reflected background is minimized.

### **3.6. Acknowledgments**

This work was funded by the Swiss Nanoscience Institute in Basel, Switzerland (SNI PhD graduate school). We would like to thank the technical staff of the Laboratory for Micro- and Nanotechnology, PSI, and Steffen Reidt from IBM Zürich, Rüschlikon, for their technical help and fruitful discussions.

## Nanofluidic lab-on-a-chip trapping devices for screening electrostatics in concentration gradients

*The following section has been published in:*

Microelectronic Engineering, Volume 175, 17-22, 2017  
<http://dx.doi.org/10.1016/j.mee.2016.12.017>

### Nanofluidic lab-on-a-chip trapping devices for screening electrostatics in concentration gradients

**Michael Adrian Gerspach<sup>a,b,c,\*</sup>, Nassir Mojarad<sup>d</sup>, Deepika Sharma<sup>a,b,e</sup>, Thomas Pfohl<sup>a,c,f</sup>, Yasin Ekinci<sup>a,b</sup>**

<sup>a</sup> *Swiss Nanoscience Institute, 4056 Basel, Switzerland*

<sup>b</sup> *Laboratory for Micro and Nanotechnology, Paul Scherrer Institut, 5232 Villigen, Switzerland*

<sup>c</sup> *Chemistry Department, University of Basel, 4056 Basel, Switzerland*

<sup>d</sup> *Nanotechnology Group, ETH Zürich, 8803 Rüschlikon, Switzerland*

<sup>e</sup> *Biozentrum, University of Basel, 4056 Basel, Switzerland*

<sup>f</sup> *Biomaterials Science Center, University of Basel, 4123 Allschwil, Switzerland*

\* Correspondence: [michael.gerspach@unibas.ch](mailto:michael.gerspach@unibas.ch) (M.A. Gerspach), [thomas.pfohl@gmail.com](mailto:thomas.pfohl@gmail.com) (T. Pfohl), [yasin.ekinci@psi.ch](mailto:yasin.ekinci@psi.ch) (Y. Ekinci)

Keywords: nanofluidic systems, geometry-induced electrostatic trapping, nano-object trapping, concentration gradient, high-throughput screening, glass-based GIE trapping devices

**Abstract**

Geometry-induced electrostatic (GIE) trapping is a novel contact-free method of stably confining charged nano-objects in solution. This method has proven to be very effective in trapping sub-100 nm objects and is based only on the electrostatic repulsion between the charged object and the device surfaces, without requiring an external control or power. We report on fabricating a GIE trapping device integrated into a microfluidic system and demonstrate its performance in screening the behaviour of individually trapped nano-objects along a NaCl salt concentration gradient. We use 60 nm gold particles as probes to analyze the trapping stiffness and residence time of the particles along the salt gradient. We show that in our devices a critical concentration for the reliable trapping of the particles in the order of seconds is reached at an ionic concentration of 0.3 mM. By analyzing the trap stiffness and residence times, we determine a smooth gradient of the salt concentration, as expected from Fick's first law. Furthermore, we find that the instability of the colloidal dispersion is reached at 0.8 mM NaCl.



## 4.1. Introduction

Stable contact-free trapping and detection of single nano-objects in solutions provide the ultimate sensitivity in characterizing analytes at nanometer dimensions. This methodology offers explicit information on local dynamics, reactions, structural information, and net charges. Extensive developments in active trapping methods, such as optical [49, 50, 56], plasmonic [65, 70, 75], magnetic [77, 82] or acoustic [94, 95] tweezers, rely on the induced field gradient and have been successfully demonstrated for stable confinement of single objects. However, stable trapping of nano-objects smaller than 100 nm remains challenging for such methods as the trapping force, for instance in optical tweezers, relies on the polarizability,  $\alpha$ , of the trapped objects, which scales with the third power of the object size. In addition,  $\alpha$  vanishes when the material properties of the object and its surrounding media are similar. As a result, for trapping ever smaller objects using optical tweezers, large field powers in the order of hundreds of mW are needed [61], which might lead to photodamage in specimens [62].

Geometry-induced electrostatic (GIE) trapping is a field-free method that allows reliable confinement of nanometer-size objects for time durations from seconds to hours [17]. This method comes with the key benefit that the trapping force depends only on the net charge of the object rather than on its size and mass. In conventional GIE trapping devices, single negatively-charged nano-objects are trapped by electrostatic repulsion from negatively-charged SiO<sub>2</sub> walls in nanofluidic channels. The surface topology of the channels is tailored by nanometer-sized indentations, which results in the formation of local energy potential wells, as shown in Fig. 4.1. This system has the flexibility that various trapping geometries such as circular pockets or rectangular slits or grids can be realized using, for example, e-beam lithography. The depth of the potential wells, and thereby the trapping strength and time, can be adjusted by altering the size of the indentations, the nanofluidic channel height, the surface charge density, and the ionic concentration of the buffer solution. GIE trapping has evolved over the years to be used for stable trapping of single gold nanoparticles (Au NPs) [7, 17, 120], polymer beads, lipid vesicles [17], as well as for angular dependent trapping of silver nanorods [121], which can be used for digital information storage applications [122]. While lab-on-chip approaches made from silicon or glass substrates have fixed nanofluidic channel heights and trap geometries, active approaches such as scanning-aperture trapping [103] or piezo-controlled SiO<sub>2</sub> slices [104] are capable of altering the trap potential depth during the experiment. Nevertheless, the ease-of-use of the chip-based devices makes integration into more complex microfluidic systems straightforward and would provide a range of new applications for electrostatic trapping, such as high-throughput screening of nano-objects, *in*

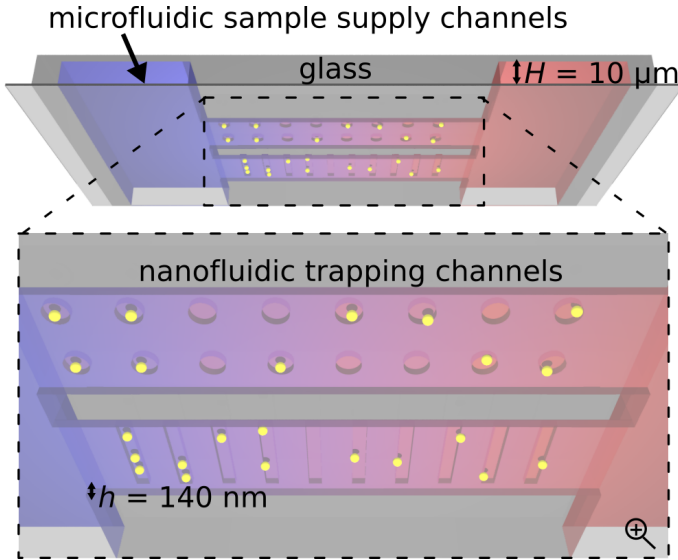


**Figure 4.1.:** Schematic of a geometry-induced electrostatic (GIE) trapping device integrated into a microfluidic system. Nano-objects are trapped within the pockets and slits of the nanofluidic channels (middle) by electrostatic repulsion. Large microfluidic supply channels provide the GIE trapping area with reactants or buffer solutions (left and right).

*situ* mixing and sorting of nano-objects, or the feasibility to precisely control the fluidic conditions.

In this work, we demonstrate the successful integration of GIE trapping devices into a microfluidic system and utilize it for determining very small sample and reagent quantities, precise control of reactant concentrations, and short analysis times (see Fig. 4.1). In this system, a precise and controlled steady-state concentration gradient can be formed along the trapped nano-objects e.g. of reactants, pH or salt, allowing the analysis and screening of contact-free trapped nano-objects in different environments in a single experiment using one device. We use Au NPs of 60 nm diameter as probes along a NaCl gradient, and thereby find critical concentrations on trapping strength and particle aggregation stability, an important parameter of nanoparticle emulsions. For optical visualization of the particle motions, we used interferometric scattering detection (iSCAT), which relies on the interference between the reflected beam at the interfaces in the device and the light scattered from the particle. Due to the strong optical scattering of the Au NPs [120] and the interferometric nature of the detection, iSCAT allows for high signal-to-noise

ratio (SNR) imaging and thus sensitive and fast detection of particle trajectories [15, 17, 29, 120]. For improved SNR imaging [156], the devices were fabricated from glass substrates using top-down nanofabrication methods, i.e. reactive ion etching (RIE) and electron beam (e-beam) lithography.

## 4.2. Chip design and working principle

The architecture of the multi-height device is sketched in Fig. 4.2A. It is made of two main elements: the microfluidic channels, which serve as sample supplies, and the GIE trapping nanofluidic area. Two microfluidic channels are separated by a distance of  $890 \mu\text{m}$  and have a depth of  $H = 10 \mu\text{m}$ , each connected by an inlet and outlet. The two microfluidic channels are interconnected by several GIE trapping channels with a length of  $L = 890 \mu\text{m}$  and a height of  $h = 50 - 200 \text{ nm}$ . Within these nanofluidic channels finer nanostructures, i.e. the actual nanotraps are etched. Microfluidic tubings are connected to the inlets and outlets for the delivery of sample, reactant, and buffer solutions.

The device is filled by injecting the sample solution through the upper microfluidic supply channel as sketched in Fig. 4.2B. The GIE trapping nanofluidic channels are easily filled with the sample solution containing the NPs by capillary forces. After the particles are trapped in the GIE trapping area, the upper and lower supply channels are flushed with buffer and reactant solutions, respectively. The supply channels are only connected through the nanofluidic channels and are continuously flushed with fresh solutions at equal flow rates to ensure a pressure difference between the supply channels of  $\Delta p = 0$ . This results in a linear steady-state gradient between the two buffer solutions in the GIE trapping area, caused by diffusion [157]. Based on Fick's first law of diffusion, the net flux of the ions or reactants in solution in the nanofluidic channels,  $J_x$ , is written as [158]

$$J_x = -D \frac{\delta C}{\delta x} = -D \frac{C_2 - C_1}{L}, \quad (4.1)$$

where  $D$  is the diffusion coefficient and  $\delta C/\delta x$  is the change of concentration along the nanofluidic channel between the upper and lower solutions with concentrations of  $C_1$  and  $C_2$ , respectively. Hence, the concentration at any given position  $x$  in the nanofluidic trapping channels with a length of  $L$  is given by

$$C(x) = \gamma x + C_1 \quad (4.2)$$

where  $\gamma = \frac{C_2 - C_1}{L}$ . After an idle time to evolve a steady state, depending on the reactants diffusion coefficients, measurements of the motion of trapped

nano-objects along the nanofluidic channels are performed at various positions.

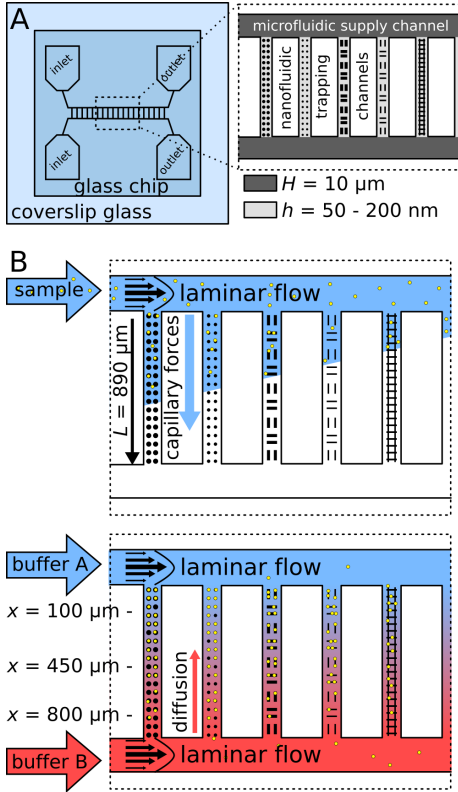


**Figure 4.2.:** Top view schematic of the microfluidic device design with the integrated nanofluidic GIE trapping area. The microfluidic channels have a depth of  $10 \mu\text{m}$  and are only connected through the nanofluidic channels with a height from  $50 - 200 \text{ nm}$ . B) Sketch of the experimental process and the principle function of the device. The nano-objects are filled into the GIE trapping area by capillary forces. A linear steady-state gradient in the trapping region (nano-channels) is created by flowing two different solutions through the upper and lower microfluidic supply channels, respectively. The gradient is formed in the nanofluidic channels by diffusion. Thus the analysis of individual nano-objects at different concentrations is achieved within a single device.

### 4.3. Material and Methods

#### 4.3.1. Experimental setup

iSCAT was used as the imaging method to visualize the trajectories of the NPs. A green 300 mW solid-state laser (MGL-III-532, CNILaser), with  $\lambda = 532 \text{ nm}$ , which is near the plasmon resonance peak of the Au NPs, was focused and scanned on the back focal plane of an inverted microscope (DMI 5000 M, Leica) equipped with a  $100\times$  magnification, 1.3 NA oil objective (HCX PL Fluostar,

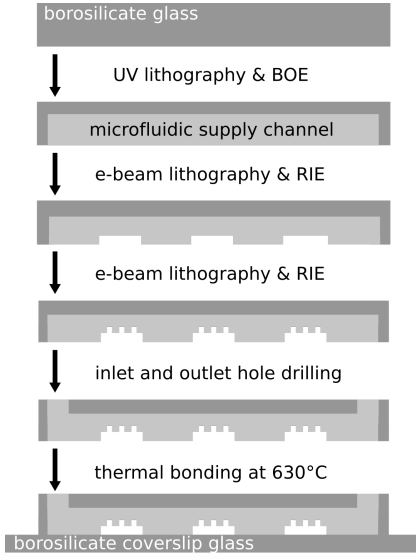


**Figure 4.3.:** Side view of the fabrication steps of the GIE trapping devices integrated into a microfluidic system. The devices are fabricated using UV-lithography, electron beam lithography and thermal bonding.

Leica) and an additional internal  $1.5\times$  tube lens (Leica). The laser intensity was attenuated with neutral density (ND) filters to reach a laser output power of 1-2 mW before the microscope objective in order to achieve a high SNR signal while avoiding saturation of the camera pixels. To scan the laser over the sample, an  $x$ -,  $y$ - galvo mirror deflection system (GVS002, Thorlabs Inc.) running at 1 kHz was used. The interference signal between the scattered and reflected beams was finally imaged onto a CMOS camera (MV-D1024-160-CL-12, Photon Focus) at an exposure time of 10 ms and a sample rate of 86 Hz. To ensure a uniform illumination between the recorded frames, the camera and the  $x$ - and  $y$ - deflections of the mirror system were synchronized by a four channel AO-LabView controller (cDAQ-9171/NI 9269, LabView, with three channels used) and triggered by custom-built LabView software. The center of a Gaussian profile fit was determined for each frame to obtain the particle trajectories [120].

#### 4.3.2. Fabrication of the GIE trapping devices integrated into a microfluidic system

The fabrication process flow of the GIE trapping devices is sketched in Fig. 4.3. The process consists of three main steps: first, the fabrication of the microfluidic supply channels including the inlets and outlets, which were patterned by UV lithography and etched using buffered oxide etch (BOE); second, the

implementation of the GIE trapping areas between the microchannels, which was done by e-beam lithography and RIE; and finally, the in- and outlet holes were drilled and the device was thermally bonded to a coverslip glass. All features were patterned on a substrate of 200  $\mu\text{m}$  thick borosilicate glass wafer (Borofloat 33, Plan Optik AG). A 5 nm chromium adhesion layer and an additional 150 nm gold layer were evaporated (Univex 450) with a rate of 0.1 nm/s on both sides of the glass wafer to function as a hard mask during BOE etching. The wafer was spin-coated with a photoresist (Microposit S1813, Shipley Company; 2000 rpm, 500 rpm/s, 40 s) and exposed under UV-light for 12 s (Suess MA 6,  $\lambda = 365 \text{ nm}$ ,  $120 \text{ mJ/cm}^2$ ) using a chromium mask (Compugraphics Jena GmbH) with the design of the microchannels and the inlets and outlets. After developing in MF-24A (Shipley, Megaposit MF-24A) for 40 s, the structures were etched into the metal layers using gold etchant (200 g KI + 50 g I, dissolved in 5 l DI water) for 45 s and chromium mask etchant (Chrome ETCH No 1, Technic) for 10 s and subsequently etched 10  $\mu\text{m}$  into the glass wafer for 6 h using BOE (BOE 7:1, General Chemical Corporation) as shown in Fig. 4.4A. The remaining resist was removed in acetone and the wafer was cleaned in a piranha bath ( $\text{H}_2\text{SO}_4(\%) : \text{H}_2\text{O}_2(\%) = 2:1$ ) for 20 min at  $90^\circ\text{C}$ . The remaining metal layers were dissolved in the gold etchant and chromium mask etchant and the wafer was rigorously rinsed in DI water and dried under a nitrogen air stream. For the second step of producing nanochannels, a 25 nm Cr layer was evaporated on the structured side of the glass wafer, which serves as a hard mask during RIE. PMMA was spin-coated (E-Beam Resist PMMA 940K, Allresist; 4% in ethylacetate, 4000 rpm, 500 rpm/s, 120 s) on the chromium layer and cured on a hotplate at  $180^\circ\text{C}$  for 4 min. Parallel fluidic channels with a length of 1 mm and a width of 5 – 20  $\mu\text{m}$  were exposed into the PMMA resist using e beam lithography (Vistec EBPG 5000 Plus) and developed in MIBK:IPA (1:3, 60 s). After etching the channels into the chromium layer (BMP Plasma Technology GmbH,  $\text{O}_2:\text{Cl}_2$  with a 1:5 ratio) and stripping the resist in acetone, RIE (Oxford 100, Ar 38 sccm,  $\text{CHF}_4$  12 sccm, 100 W) was used to etch the structures 140 nm deep into the glass wafer (see Fig. 4.4A and B). The chromium layer was then removed in a chromium mask etchant solution, rinsed in DI water and dried under a nitrogen air stream. These steps were repeated with a 15 nm chromium layer as the hard mask to etch the finer nanostructures (circular pockets, rectangular slits or grids with a diameter or width of 200 and 500 nm) 70 nm into the nanofluidic channels (see Fig. 4.4A and B). After dicing the wafer into  $15 \times 15 \text{ mm}^2$  chips, holes of 1 mm diameter were drilled into the in- and outlets of the device using a diamond drill bit (see Fig. 4.4C). The wafer and chips were covered with a protection resist (Microposit S1813, Shipley Company; 3000 rpm, 500 rpm/s, 40 s) during the dicing and drilling to prevent the adhesion of glass dust to the device surface. After removing the resist in acetone, the chips and borosilicate coverslip glasses with a thickness

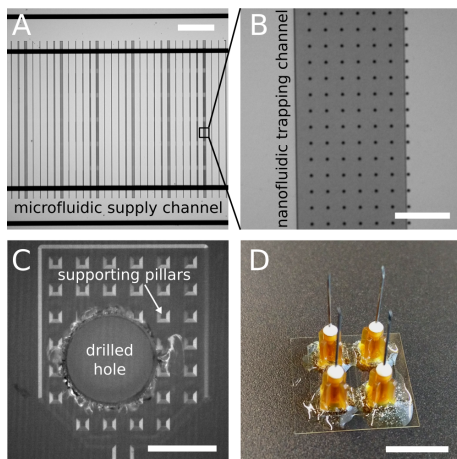


**Figure 4.4:** A) Optical image of the microfluidic supply channels (horizontal lines) connected by several nanofluidic trapping channels (vertical lines), scale bar  $200\ \mu\text{m}$ . B) Optical image of a nanofluidic trapping channel including the finer traps with a diameter  $d = 500\ \text{nm}$ , scale bar  $10\ \mu\text{m}$ . C) Optical image of a hole drilled into the inlets and outlets of the devices before bonding to a coverslip glass, scale bar  $1\ \text{mm}$ . The pyramidal structures are supporting pillars that prevent the chamber from possible collapse during the thermal bonding process. D) Final device after bonding process and ports attachment, scale bar about  $10\ \text{mm}$ .

of  $150\ \mu\text{m}$  (Borofloat 33, Plan Optik) were cleaned in a freshly made piranha solution for 10 min, activated in 29% ammonium hydroxide solution at  $35^\circ\text{C}$  for 40 min, rigorously rinsed in DI water, and dried with nitrogen. The chips and the coverslip glasses were directly aligned and pressed together for at least 24 h at a pressure of  $390\ \text{kN/m}^2$ . The chips were subsequently placed into a thermal annealing furnace (Process Products Corporation) and covalently bound together at  $630^\circ\text{C}$  without applied pressure. For more details on the thermal bonding process see references [153, 156]. Four syringe needles were prepared by shortening the plastic cylinders with a razor blade to reduce the dead volume. The needles were glued on top of the inlet and outlet holes for tubing connections using a two-component epoxy resin (UHU PLUS, Schnellfest 5 min). An image of the final device is shown in Fig. 4.4D.

#### 4.3.3. Sample preparation

877 mg of NaCl (S9888, Sigma Aldrich) was dissolved in 15 ml DI water ( $18\ \text{M}\Omega$ ) to obtain a stock solution of 1 M. Then, serial dilutions using DI water were performed to obtain the 0.05 mM and 1 mM salt solutions. Commercially available Au NPs with a diameter of 60 nm were purchased from BBI Solutions (EM.GC60). The 60 nm Au NPs were centrifuged at 2000 rcf for 20 min. The supernatant was tipped away and the particles were re-suspended in the 0.05 mM salt solution to exchange the buffer solution. This step was repeated once. To create a dense solution of Au NPs of about  $10^{11}$  particles/ml, the particles were centrifuged a third time and the excess salt solution was removed.

## 4.4. Results and Discussion

To demonstrate the potential of the GIE trapping devices integrated into a microfluidic system, we generated a NaCl gradient along the nanofluidic channels hosting 500 nm wide pockets. In this work, we focused on the investigation of cylindrical pockets in order to extract quantitative information on the particles dynamics such as radial trap stiffness and residence times. 1  $\mu\text{l}$  of the Au NPs in  $C_1 = 0.05$  mM NaCl solution (blue) were inserted into the upper microfluidic supply channel. After the GIE trapping area was filled and the particles were trapped in the pockets, a solution of  $C_2 = 1$  mM (red) was inserted into the lower microfluidic supply channel. The solutions were continuously refreshed through the microfluidic channels at flow rates of 1 nl/s. Before the particles were recorded at several positions along the channel, the system was left for 10 min to establish a steady-state linear gradient of the concentration with  $\gamma = 1.07 \cdot 10^{-3} \text{mM}/\mu\text{m}$ .

### 4.4.1. Screening the ionic strength

The trapping strength of the potential wells depends on the electrostatic repulsion between the device surface and the trapped object. This parameter can be adjusted by varying the nanofluidic channel height, trap diameter and depth, the net charge of the nano-object, and the ionic concentration of the buffer solution. The electrostatic potential near a charged surface in solution follows an exponential decay with a characteristic length scale, called the Debye length  $\kappa^{-1}$ , which is proportional to  $1/\sqrt{C}$ . Thus, adding salt to the solution causes screening of the surface charges of the device and the nano-object by the free counter ions in solution, making the trapping force weaker.

We recorded the motion of trapped 60 nm Au NPs ( $\sim -96 e$ ) at different positions along the nanofluidic channels, which correspond to different ionic concentrations, highlighted by the stars in Fig. 4.5A. Three sample plots of the lateral motions of the particles at the positions  $x = 73 \mu\text{m}$  (blue),  $x = 136 \mu\text{m}$  (green) and  $x = 193 \mu\text{m}$  (orange) are illustrated in Fig. 4.5B. The positions of the trapped particles correspond to an ionic concentration of the solution of 0.13 mM, 0.2 mM and 0.26 mM. The lateral motion plots clearly illustrate that the confinement of the particles within the traps is weakened as the ionic concentrations along the channel is increased. To quantify the trapping strength of the particles, we calculated the corresponding mean square displacements (MSD),  $\langle [\Delta r(\Delta t)]^2 \rangle$  as a function of lag time  $\Delta t$  for each position. Six sample MSD plots, which correspond to the concentrations highlighted with the stars in Fig. 4.5A, are shown in Fig. 4.5C. In contrast to a freely diffusing particle where the MSD continuously increases proportional



to  $\Delta t$ , it reaches a plateau for long lag times (lag times much higher than the relaxation time of the particle in the potential well) for a particle restricted in diffusion [141]. The plateau represents the strength of the confinement and, for a harmonic trapping potential, is directly correlated to the radial trap stiffness  $k_r$  by [7, 159]

$$\langle [\Delta r(\Delta t)]_p^2 \rangle = \frac{4k_B T}{k_r}. \quad (4.3)$$

The trapping stiffness obtained from the MSD plateaus are plotted in Fig. 4.5D. For low salt concentration of 0.13 mM, a strong trap stiffness of 0.009 pN/nm is observed. However, higher salt concentrations along the gradient in the nanofluidic channel reduce the trapping strength as expected, which can be seen in the increased plateaus of the MSDs. At a concentration of 0.26 mM, the trap stiffness was reduced by about an order of magnitude to 0.0017 pN/nm.

#### 4.4.2. Effect of solution ionic strength on residence time

At a low solution ionic strength, the particles were trapped stably from several seconds up to hours at very low salt concentrations below 0.15 mM. However, at concentrations above 0.3 mM, particles escaped more frequently from the traps making a quantitative analysis of the trapping stiffness in these regions difficult. The residence time, defined as the average time a particle levitates in the potential well before escaping, is also shortened at higher ionic concentrations due to the reduced Debye length and thus lower potential well. We investigated the residence times along the nanofluidic channel at higher salt concentrations as illustrated in Fig. 4.5E. At concentrations below 0.3 mM the particles could be stably trapped with an average trapping time of 18 s at 0.22 mM. However, at a concentration of 0.31 mM, the residence time was shortened to only 1.8 s and further decreased to only about 150 ms at a concentration of 0.62 mM. Applying an exponential fit to the data indicates that the critical concentration for trapping the particles longer than a second was reached at an ionic concentration of 0.4 mM. We should remark that the obtained results on the residence times illustrate the performance of the device with a channel height of  $h = 140$  nm and a trap diameter of  $d = 500$  nm, which was selected to demonstrate the different behavior along the salt gradient from  $C_1 = 0.05$  mM to  $C_2 = 1$  mM. However, higher trapping strength and longer residence times can be achieved by fabricating thinner nanofluidic channels.

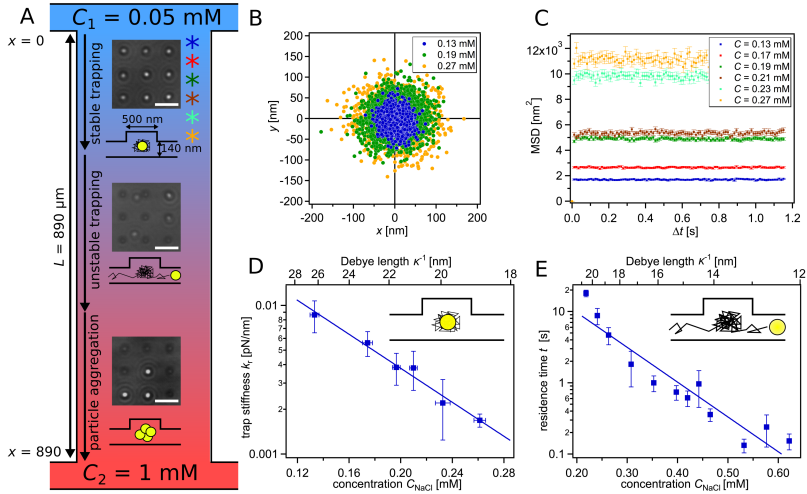


**Figure 4.5.:** A) Sketch that summarizes the results obtained by trapping 60 nm Au NPs along a NaCl gradient from 0.05 mM to 1 mM in a GIE trapping device with a height of  $h = 140$  nm and pocket diameters of  $d = 500$  nm. Whereas the particles are stably trapped at low salt concentrations up to 0.3 mM, the trapping times are shortened for higher concentrations. At concentrations higher than 0.8 mM, the particles become unstable and form aggregations. Scale bars of optical iSCAT images equal 3  $\mu\text{m}$ . B) An example of lateral position plots of 60 nm particles along the nanofluidic channel at different concentrations of 0.13, 0.20 and 0.26 mM NaCl corresponding to the marked positions with stars in A). C) Sample mean square displacement (MSD) plots of single particles with a lag time  $\Delta t = 11$  ms corresponding to the lateral position plots in B) and the marked positions in A). D) Radial trapping stiffness  $k_r$  calculated from the MSD plots in C).  $X$ -error bars describe the standard deviation of the position of trapped particles in the channel.  $Y$ -error bars describe the standard deviation of the trap stiffness of several analyzed particles in the same regions. E) Residence times of particles at higher salt concentrations along the nanofluidic channel.  $Y$ -error bars are the standard deviation of analyzed residence times of particles at the given positions.

#### 4.4.3. Instability of the colloidal dispersion at high salt concentrations

Particle motions were recorded further down in the nanochannels at high salt concentrations, where stable trapping of the particles was also observed. However, the trapped particles appeared with an increased intensity as seen in the bottom iSCAT image of Fig. 4.5A. The increased intensity signifies that the particles formed aggregations and could be trapped due to higher net charges or steric restrictions. The clustering of the particles was observed at ionic concentrations starting from 0.8 mM NaCl and higher. Charged particles in contact with a polar medium are as well surrounded by an electrostatic

potential. The electrostatic repulsion between the particles in the dispersion prevents the particles from forming aggregations. However, increasing the salt concentration of the dispersion reduces the Debye length of the electrostatic potential of the particles and leads to instability and aggregation of the particles. These results are consistent with the observation made during washing of the 60 nm Au NPs directly in a salt concentration of 1 mM. After centrifugation of the 60 nm particles and replacing the initial buffer solution with a 1 mM NaCl solution, a black precipitation was immediately obtained at the inner surface of the Eppendorf tubes, indicating that the particles formed aggregates and adsorbed at the surface.

## 4.5. Conclusion

In this work, we introduced the fabrication of new geometry-induced electrostatic (GIE) trapping devices integrated into a microfluidic system. The fully integrated system comes with key benefits such as reduced sample volume, in situ change of solutions during the experiment, precise control of solution delivery, and the feasibility to trap nano-objects along a gradient of e.g. salt or other reactants. In single experiments, we could quantitatively analyze the performance of our chip on the reliable trapping of 60 nm Au NPs along a salt gradient. Furthermore, the critical salt concentration for the stability of the colloidal dispersion was reached at 0.8 mM. Our extension of this method by successful integration of nanofluidic traps into a microfluidic system sets the ground for a variety of new experiments. The presented concept can be used for high-throughput screening over a range of reactant concentrations of individual trapped nanoparticles or biomolecules, such as DNA, viruses or large proteins.

## 4.6. Acknowledgments

This work was funded by the Swiss Nanoscience Institute in Basel, Switzerland (SNI PhD Graduate School, Project P1202). We would like to thank the technical staff of the Laboratory for Micro- and Nanotechnology, PSI Villigen, for their technical help and fruitful discussions.



## Soft electrostatic trapping in nanofluidics

*The following section has been accepted in:*

Microsystems & Nanoengineering

### Soft electrostatic trapping in nanofluidics

Michael A. Gerspach<sup>a,b,c</sup>, Nassir Mojarad<sup>d,e</sup>, Deepika Sharma<sup>a,b,f</sup>,  
Thomas Pfohl<sup>a,c,g,h,\*</sup>, Yasin Ekinci<sup>a,b,\*</sup>

<sup>a</sup> *Swiss Nanoscience Institute, 4056 Basel, Switzerland*

<sup>b</sup> *Laboratory for Micro and Nanotechnology, Paul Scherrer Institut, 5232 Villigen, Switzerland*

<sup>c</sup> *Chemistry Department, University of Basel, 4056 Basel, Switzerland*

<sup>d</sup> *Nanotechnology Group, ETH Zürich, 8803 Rüschlikon, Switzerland*

<sup>e</sup> *Current employer: ABB Switzerland Ltd., Semiconductors, 5600 Lenzburg, Switzerland*

<sup>f</sup> *Biozentrum, University of Basel, 4056 Basel, Switzerland*

<sup>g</sup> *Biomaterials Science Center, University of Basel, 4123 Allschwil, Switzerland*

<sup>h</sup> *New address: Institute of Physics, University of Freiburg, 79104 Freiburg, Germany*

\* corresponding authors: [thomas.pfohl69@gmail.com](mailto:thomas.pfohl69@gmail.com), [yasin.ekinci@psi.ch](mailto:yasin.ekinci@psi.ch)

Keywords: contact-free electrostatic nanoparticle trapping, PDMS nanofluidic devices, high-throughput fabrication, single nano-object manipulation, soft-lithography

## **Abstract**

Trapping and manipulation of nano-objects in solution are of great interest and have emerged in a plethora of fields spanning from soft condensed matter to biophysics and medical diagnostics. We report on establishing a nanofluidic system for reliable and contact-free trapping as well as manipulation of charged nano-objects using elastic polydimethylsiloxane (PDMS)-based materials. This trapping principle is based on electrostatic repulsion between charged nanofluidic walls and confined charged objects, called geometry induced electrostatic (GIE) trapping. With gold nanoparticles as probes, we study the performance of the devices by measuring the stiffness and potential depths of the implemented traps, and compare the results with numerical simulations. When trapping 100 nm particles, we observe potential depths of up to  $Q \cong 24 k_B T$  that provide stable trapping for many days. Taking advantage of the soft material properties of PDMS, we actively tune the trapping strength and potential depth by elastically reducing the device channel height, which boosts the potential depth up to  $Q \sim 200 k_B T$ , providing practically permanent contact-free trapping. Due to a high-throughput and low-cost fabrication process, ease of use, and excellent trapping performance, our method provides a reliable platform for research and applications in study and manipulation of single nano-objects in fluids.

## 5.1. Introduction

The unique properties of the polydimethylsiloxane (PDMS) elastomer in making integrated microfluidic systems established its applications as a standard tool in a broad range of disciplines, such as disease diagnostics [160], cell biology [161], drug discovery [162], and photonics [163], to name a few. Biocompatibility, gas permeability, optically transparency, and having a low elastic modulus are its most important chemical and physical features that allow for its implementation in such diverse fields [164]. A reduction of channel dimensions and fabricating nanofluidic PDMS devices not only provides a higher efficiency and sensitivity to analytes, but could also allow for controlled processing of objects with nanometer dimensions in soft matter such as colloids, viruses and individual macromolecules. Recent efforts in developing tailored fabrication procedures led to the fabrication of nanofluidic PDMS channels that provide laminar flows without clogging or collapse [165, 166]. More advanced integrated systems were also adapted to applications in, e.g. protein preconcentration [167], DNA stretching [168] and Raman spectroscopy [169].

However, stable trapping and manipulation of single nano-objects in PDMS devices are hindered by the lack of techniques that produce strong retraction forces acting against the driving force of randomization, the Brownian motion. On average, every single particle contains an energy of  $1/2 k_B T$  for each translational dimension. However, the instantaneous velocity of a particle follows a Maxwell-Boltzmann distribution [44–46], in which the energy of the particle can temporarily considerably exceed the average value. To compensate for these high energy kicks, typically potential depths of around  $10 k_B T$  are required for stable trapping of an object in solution as established by Ashkin *et al.* [47, 48].

Geometry-induced electrostatic (GIE) trapping is an effective method for parallel trapping of charged nanoparticles in a nanofluidic system [17]. This method has shown to be efficient for levitating various types of objects including metal nanoparticles of various shapes [121], sizes [7, 156] and charges [125], as well as polystyrene beads [17] and lipid vesicles [17, 103]. Moreover, it has been used in other applications such as single particle charge and size determination [7], information storage [122], and screening of electrostatic potentials [124]. The underlying physical principle of GIE-trapping is the creation of local electrostatic potential minima in a nanofluidic channel by introducing indentations in one surface of the channel. These indentations result in potential wells for stable trapping of nano-objects carrying the same sign of the net charges as that of the walls (Fig. 5.1A). For these devices, state-of-the-art fabrication procedures play a vital role, since smallest pertur-

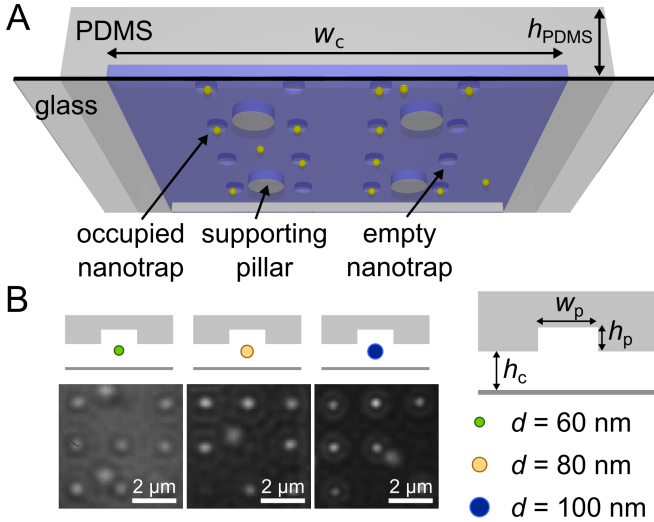


**Figure 5.1.:** A) Schematic of the PDMS-based nanofluidic trapping device with integrated pockets and supporting pillars. The nanofluidic channels had a width of  $w_c = 10 \mu\text{m}$ . Two device geometries  $G_1$  ( $h_c = 210 \text{ nm}$ ,  $h_p = 70 \text{ nm}$ ) and  $G_2$  ( $h_c = 160 \text{ nm}$ ,  $h_p = 100 \text{ nm}$ ) were used for trapping gold nanoparticles. The width  $w_p$  of the pockets varied in both device geometries from 200 to 500 nm. B) Schematics and corresponding experimental optical iSCAT images of  $d = 60$ , 80 and 100 nm gold particles trapped in circular pockets with a diameter of  $w_p = 250 \text{ nm}$  in  $G_2$  devices. Scale bars:  $2 \mu\text{m}$ .

bations from the ideal device geometry largely distort the potential landscape. Hence, the fabrication of GIE-trapping devices has been limited to using  $\text{SiO}_x$  substrates processed by top-down nanofabrication procedures, making their production time consuming and resource demanding, practically limiting them to exploratory applications. As a result, PDMS-based GIE-trapping devices fabricated by soft lithography will substantially reduce production costs and time, making them easily to integrate into standard lab-on-a-chip systems, and making them available for research and commercial applications.

In this article, we report on the successful fabrication of PDMS-based nanofluidic systems that are used for GIE-trapping of charged nano-objects. Designing optimal device geometries, using precise fabrication techniques and an appropriate PDMS composition, preloading the device prior to bonding, and applying a tailored topographical design to avoid channel collapse play crucial roles in obtaining functional trapping devices. We use gold nanoparticles (Au NPs) down to 60 nm as probes to characterize the main trapping features such as the strength, lateral extension, and potential depth. For imaging,



interferometric scattering detection (iSCAT) is used as a sensitive technique that allows for precise tracking of Au NPs as seen in Fig. 5.1B [120, 156]. Beyond passive nanoparticle trapping, we also demonstrate active manipulation of the trap stiffness by locally applying a mechanical force to elastically deform the device, a feature that is not possible in SiO<sub>x</sub>-based devices. A successful implementation of PDMS nanofluidics would allow for facile production of functional nanofluidic systems and could provide a unique platform in fields such as single-molecule force spectroscopy, pharmaceutical drug discovery and integrated labs-on-chips.

## 5.2. Materials and Methods

### 5.2.1. Device design

The design of the multi-height GIE trapping silicon master is sketched in Fig. 5.2A. It consists of two microfluidic reservoir channels and the nanofluidic GIE trapping region. The two microfluidic channels have a depth of  $H = 3 \mu\text{m}$  and a width of  $100 \mu\text{m}$ , each connected by an inlet and outlet. Several GIE trapping nanofluidic channels with a length of about 0.5 mm are connected with the microfluidic channels. Within these nanofluidic channels finer nanostructures, i.e. the actual nanotraps are etched. The design schematics and fabrication steps of the nanofluidic trapping region are depicted in Figs. 5.1 – 5.3. The nanofluidic channels have a width of  $w_c = 10 \mu\text{m}$ . Two device geometries were fabricated with a nanofluidic channel height of  $h_c = 210 \text{ nm}$  (device geometry  $G_1$ ) or  $h_c = 160 \text{ nm}$  (device geometry  $G_2$ ) as shown in Fig. 5.2C. Along the width of each channel, circular indentations (pockets) with a depth of  $h_p = 70 \text{ nm}$  ( $G_1$ ) or  $h_p = 100 \text{ nm}$  ( $G_2$ ) and diameters of  $w_p = 200 - 500 \text{ nm}$  were fabricated. Supporting pillars with a diameter of  $1 \mu\text{m}$  and a spacing of  $4 \mu\text{m}$  were implemented in the devices to prevent the channels from sagging and collapsing (Fig. 5.1, 5.2 and Supplementary Information 5.7.1). A final PDMS device filled with methylene blue for better visualization is shown in Fig. 5.2B.

### 5.2.2. Device fabrication

The transition from micro- to nanofluidics requires advanced designs, material processing and handling techniques to obtain functional PDMS devices that are micrometer in width but only nanometers in height. The fabrication steps of the nanofluidic trapping region are shown in Fig. 5.3. A silicon master was first made (Fig. 5.3A) by top-down fabrication methods in a cleanroom facility, namely electron beam (e-beam) lithography, followed by reactive ion etching (RIE). Next, a replica molding was carried out using a UV

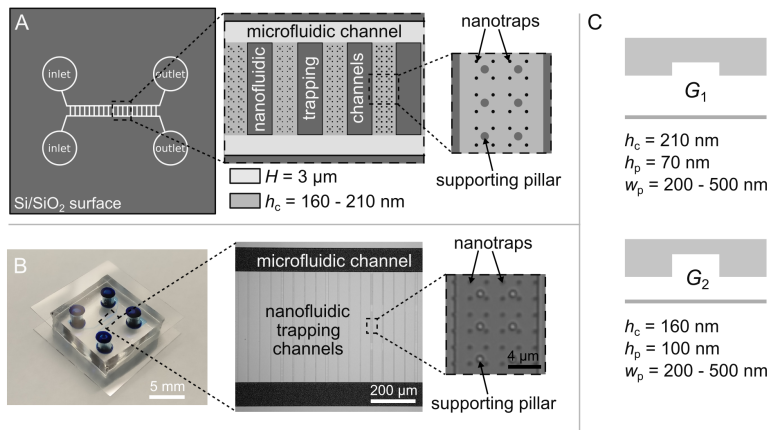


**Figure 5.2.:** A) Schematic of the silicon master design highlighting the two main features, the microfluidic reservoir channels and the nanofluidic GIE trapping area. B) Optical images of a finished PDMS device with the punched inlets and outlets and filled with a 0.2% methylene blue solution for better visualization of the microfluidic channels (left), a silicon master showing the magnified area of the microfluidic reservoir channels and the nanofluidic trapping channels (middle) and a silicon master showing one magnified nanofluidic trapping channel (right). Scale bars of images: left 5 mm, middle 200  $\mu\text{m}$ , right 4  $\mu\text{m}$ . C) Schematic of the two device geometries used for trapping gold nanoparticles.

curable hybrid polymer (OrmoStamp<sup>®</sup>, micro resist technology GmbH, 12555 Berlin, Germany) to obtain a negative copy of the original silicon master (Fig. 5.3B) [170–172]. This step brings along two major benefits: (i) the established fabrication steps available and optimized for silicon-based GIE trapping devices do not need a redevelopment to obtain negative masters for making PDMS devices, and (ii) replica molding into OrmoStamp<sup>®</sup> results in high-throughput fabrication because several negative OrmoStamp<sup>®</sup> masters can be produced from a single silicon master, which leads to benefits in rapid replication and possibilities for commercial applications (Fig. 5.3D). The last step, transferring the OrmoStamp<sup>®</sup> into PDMS (Sylgard 184 Silicone Elastomer, Dow Corning Corporation, Midland, 48686-0994 Michigan, USA) structures (Fig. 5.3C) was then carried out under a laminar flowbox in a conventional chemistry lab. To increase the stiffness of PDMS and thereby reduce the risk of channel collapse [173, 174], PDMS was mixed at a crosslinking rate of 5:1 (prepolymer : crosslinker) resulting in an elastic modulus of about  $E = 3.6 \text{ MPa}$  [175]. The PDMS was cured on a hotplate at 150°C, which is the optimized temperature for high patterning resolution [176, 177] and fast crosslinking. After curing, inlet and outlet reservoirs of 4 mm diameter were punched into the PDMS device as seen in Fig. 5.2B. The detailed

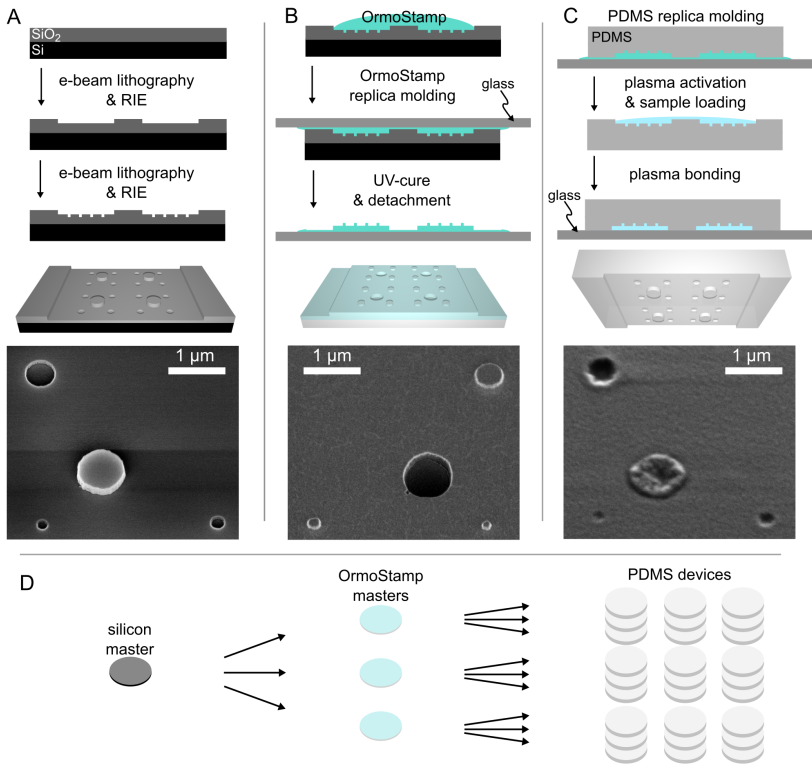


**Figure 5.3.:** Side view sketch, 3D-model and SEM images of the fabrication steps of the GIE trapping devices. Scale bars: 1 μm. A) Fabrication of a silicon master using top-down nanofabrication tools in cleanroom facilities. B) Replica molding of the original silicon master using a UV curable resin (OrmoStamp<sup>®</sup>) to obtain a negative master. This step can be repeated unlimited to receive multiple negative masters enabling a high-throughput production of PDMS devices. Each obtained OrmoStamp<sup>®</sup> master can be repeatedly used for PDMS replica molding. C) Replica molding of the negative OrmoStamp<sup>®</sup> master into PDMS. The cured PDMS devices were plasma activated and covalently bound to a coverslip glass. D) Sketch of high-throughput fabrication using two-step replica molding.

nanofabrication process is provided in the Supplementary Information 5.7.2.

### 5.2.3. Sample solution preparation

The Au NPs were purchased from BBI Solutions with a diameter  $d$  of 60, 80, and 100 nm (EM.GC60/80/100, BBI Solutions, CF14 5DX Cardiff, UK). 60 and 80 nm Au NPs were centrifuged two times at 2000  $g$ . To exchange the buffer solution, the Au NP pellets were separated from the solution and re-suspended in fresh deionized (DI) water (18 M $\Omega$ ) each time. After a third centrifugation and extraction of the excess water, a dense solution of Au NPs of  $\sim 10^{11}$  particles/ml was created. The extracted water was stored as a buffer solution to fill the microfluidic reservoirs and used to analyze the net charge of the particles and the ionic strength of the solution. To avoid clustering of the 100 nm Au NPs, centrifugation was done at 1500  $g$  for 15 min two times and re-suspended in DI-water to exchange the buffer solution. A dense solution of about  $\sim 10^{11}$  particles/ml of 100 nm gold particles was obtained after a third centrifugation step and decantation of the supernatant. The particle zeta potentials  $\zeta_p$ , the solution conductivities  $b$ , and the diffusion coefficients  $D$  were measured by phase analysis light scattering (Zetasizer Nano, Malvern Instruments, WR14 1XZ Malvern, UK). For 12 different measurements of each sample, 60, 80 and 100 nm Au NPs, the measured particle zeta potentials  $\zeta_p$  were  $-36 (\pm 2)$  mV,  $-34 (\pm 2)$  mV and  $-35 (\pm 3)$  mV, the solution conductivities  $b$  were  $\sim 6.2 \mu\text{S cm}^{-1}$ ,  $\sim 6.1 \mu\text{S cm}^{-1}$  and  $\sim 5.5 \mu\text{S cm}^{-1}$ , and the diffusion coefficients  $D$  were  $\sim 6.4 \mu\text{m}^2 \text{s}^{-1}$ ,  $\sim 5.2 \mu\text{m}^2 \text{s}^{-1}$  and  $\sim 4.2 \mu\text{m}^2 \text{s}^{-1}$  respectively. From the measured zeta potentials and conductivities, the average surface charge density  $\sigma_p$  and particle net charges could be calculated using the semi-empirical equation [7, 178]  $\sigma_p = -\epsilon\epsilon_0\kappa(k_B T/j e) [2 \sinh(jy/2) + (8/\kappa d) \tanh(jy/4)]$ , with the permittivity of free space  $\epsilon_0$ , the dielectric constant of the medium  $\epsilon$ , the valence of the ions  $j = 1$ , the Debye length [40]  $\kappa^{-1} = 0.304/\sqrt{c_0}$ , and  $y = \zeta_p e/k_B T$  with the elementary charge  $e$ . The ionic strength of the solution of 0.09 mM, 0.1 mM and 0.1 mM for each sample of 60, 80 and 100 nm Au NPs was estimated by the linear approximation  $c_0 = 1.6 \times 10^{-2} b$ , where  $c_0$  is in units mM and  $b$  in  $\mu\text{S/cm}$  [17, 179]. The particles net surface charge  $q$  for 60, 80 and 100 nm Au NPs was thus measured to be  $\sim -92 e$ ,  $\sim -168 e$  and  $\sim -258 e$ , corresponding to a average surface charge density of  $\sigma_p \sim 8 \cdot 10^{-3} e \text{ nm}^{-2}$ .

### 5.2.4. Experimental procedure

A 150- $\mu\text{m}$ -thick borofloat glass microscope coverslip (Borofloat 33, Plan Optik AG, 56479 Elsoff, Germany) was rinsed with acetone, IPA and DI water and dried by nitrogen blowing. The glass and a PDMS device were air-plasma activated for 35 s at a chamber pressure of 0.5 mbar and 80% power (Femto, Diener electronic GmbH + Co. KG, 72224 Ebhausen, Germany). The PDMS parts were loaded prior bonding to the coverslip glass with a solution containing the nanoparticles to prevent collapsing during bonding [174]. Therefore 0.25  $\mu\text{l}$  of the particle solution were placed directly on the nanofluidic channel region of the PDMS. Within 1 min after the activation, the PDMS device was gently pressed to the coverslip glass. After waiting another 1 min the PDMS was covalently bound to the coverslip and could not be separated anymore. Then about 60  $\mu\text{l}$  of the buffer solution was placed into each inlet, which filled the microfluidic reservoir channels by capillary forces. To stop the flow, 60  $\mu\text{l}$  of the buffer solution was filled into each outlet. Finally, the device was sealed by a second cover glass to avoid evaporation of the solutions as seen in Fig. 5.2B. The finished device was placed on the microscope holder and the particles were recorded using the iSCAT setup. For tuning the trap stiffness, the PDMS was compressed by an applied mechanical force. A precision screw (150-801ME, Thorlabs Inc., Newton, New Jersey 07860, USA) and a silicon plate of  $4 \times 4 \text{ mm}^2 \times 0.5 \text{ mm}$  was used as sketched in Fig. 5.6A and B. The pressure was applied to the PDMS surface by turning the screw clockwise to attain a stepwise deformation of the PDMS of about  $\Delta L = 15 \mu\text{m}$  each, corresponding to a pressure increase of about  $\Delta P = 10 \text{ kPa}$ . The deformation pressure was calculated by taking the Young's modulus  $E = 3.6 \text{ MPa}$  and the initial thickness of the PDMS of  $h_{\text{PDMS}} = 5 \text{ mm}$  [175].

### 5.2.5. Electron microscopy imaging and sample preparation

To inspect if the nanostructures' morphology are preserved during the two-step replica molding transfer into OrmoStamp<sup>®</sup> and PDMS, scanning electron microscopy (SEM) images were taken. To reduce charging effects during SEM imaging, a 15 nm chromium metal layer was sputtered on the OrmoStamp<sup>®</sup> and the PDMS replica mold (Leica EM SCD 500, Leica Microsystems, 35578 Wetzlar, Germany, sputtering rate 0.1 nm/s). The conductive silicon master was not specially pretreated. The wafers were imaged by a Zeiss Supra 55 VP SEM (Carl Zeiss AG, 1846 Jena, Germany) using the following imaging parameters: silicon master, EHT 10 kV, InLens, WD 6 mm; OrmoStamp<sup>®</sup> master, EHT 1 kV, InLens, WD 5 mm; PDMS, EHT 3 kV, SE2, WD 16 mm.

### 5.2.6. Optical microscopy

Interferometric scattering detection (iSCAT) was used as the imaging method for particle tracking [15, 17, 19, 20, 120, 154]. The iSCAT signal is generated by the interference of a reference beam, which is reflected by a strongly reflecting interface in the device, and the beam scattered from the particle [15, 19]. Similar to glass-based devices [156], PDMS systems have a weak reference beam caused by having a refractive index close to that of water, which increases the detected signal-to-noise ratio (SNR) of the trapped objects (Supplementary Information 5.7.3). The setup was built using a 300 mW diode-pumped solid-state laser (MGL-III-532, CNILaser, 130103 Changchun, P.R. China) at  $\lambda = 532$  nm wavelength. The laser intensity was decreased and controlled using a fixed neutral density (ND) filter of OD 2 and a continuously variable ND filter wheel of OD 0–2 (NDC-50C-2, Thorlabs Inc.). An  $xy$  galvo deflection mirror system (GVS002, Thorlabs Inc.) was used to scan the laser over the sample running at 1 kHz rate. The laser was slightly defocused on the back focal plane of an inverted microscope (DMI 5000 M, Leica Microsystems) equipped with a  $100\times$ , 1.3 NA oil-immersion objective (HCX PL FLUOSTAR, Leica Microsystems) and an additional  $1.5\times$  internal tube lens (11 888 699, Leica Microsystems). The reflected and scattered beams were imaged on a CMOS camera (MV-D1024-160-CL-12, Photonfocus AG, 8853 Lachen SZ, Switzerland). To synchronize the camera with the galvo deflection mirror system a four-channel AO-LabView controller (DAQ, National Instruments, Austin, TX 78759-3504, USA) was used and controlled by a custom made LabView software. The images for the residence time measurements were taken at an exposure time of 10 ms and an acquisition frequency from 5 – 90 Hz depending on the device geometries and particle sizes scanning a field of view  $9 \times 9 \mu\text{m}^2$ . Images for stiffness measurements were taken at an exposure time of 1 ms and an acquisition frequency of 111 Hz scanning a field of view  $1 \times 5 \mu\text{m}^2$ . The lateral trajectories of the particles were obtained by the center of a Gaussian profile fit to each frame, and the axial position is correlated to the amplitude of each profile fit [104, 120] (see Supplementary Information 5.7.4). The average lateral localization accuracy in the  $x$ - or  $y$ -direction were  $\delta x = 6.5$  nm for  $d = 60$  nm Au NPs and  $\delta x = 4.5$  nm for  $\delta x = 80$  and 100 nm Au NPs.

## 5.3. Results

### 5.3.1. Device fabrication

We used scanning electron microscopy (SEM) to determine if the shape of the small nanostructures were preserved during the two-step replica molding transfer into OrmoStamp<sup>®</sup> and PDMS. The shapes and dimensions of the 200, 250 and 500 nm pockets were well resolved in the silicon master as depicted in Fig. 5.3A. In the 30° tilt micrograph, the height difference of the pocket depth ( $h_p = 70$  nm) in comparison to the supporting pillar height ( $h_c = 210$  nm) is seen. Replica molding into OrmoStamp<sup>®</sup> preserved both lateral and axial dimensions of the nanometer-sized structures as well as the micrometer-wide channels and supporting pillars (Fig. 5.3B). The flat top of the inverse pockets indicates that the resin could permeate entirely into the pockets before UV curing. To obtain functional devices, besides the device design, proper handling of the PDMS substance by controlling the mixture, curing parameters, and sample filling play critical roles (see fabrication details in Supplementary Information 5.7.2). All pocket dimensions could be transferred from OrmoStamp<sup>®</sup> into PDMS as seen in the SEM image of Fig. 5.3C. The lateral dimensions of the pockets and supporting pillars were entirely preserved during the PDMS molding. However, the well-defined axial profile of the pockets and supporting pillars in the OrmoStamp<sup>®</sup> looked smoothed and more shallow in the PDMS mold.

### 5.3.2. Electrostatic potential landscape

In GIE-trapping devices, the induced electrostatic potentials depend on a number of parameters, such as the channel and trap height, lateral trap dimension, solution ionic strength and pH, and the surface charge density of the cover glass and PDMS surfaces. Whereas SiO<sub>x</sub>-based GIE trapping devices have similar material layers on all decisive surface sides, PDMS-based GIE trapping devices consist of a top PDMS surface and a bottom glass surface layer. However, similar surface Zeta potentials of both activated PDMS and activated glass in solution of about  $\zeta_{\text{surface}} \sim -80$  mV (see Supplementary Information 5.7.5) indicate similar numbers of spontaneous ionization of silanol groups in water. Thus, it may be expected that the potential minimum in GIE trapping devices made from PDMS and glass substrates results in the slit midplane of the nanofluidic channel.

The trapping strengths of different geometries were characterized by tracking the lateral motion of trapped Au NPs. Exemplary position plots of Au NPs trapped in  $G_2$  devices ( $h_c = 160$  nm,  $h_p = 100$  nm) with a particle diameter of  $d = 60$  nm in pockets of  $w_p = 250$  and 500 nm and with larger particles of

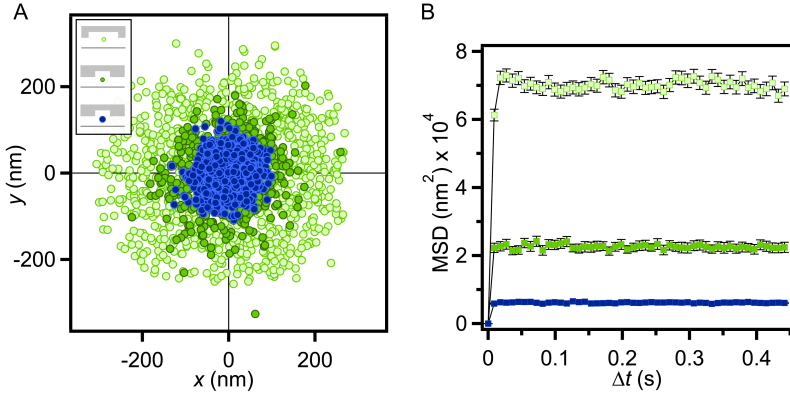


**Figure 5.4.:** Influence of lateral trap dimensions and particle net charges on the lateral trap stiffness for devices with a channel height of  $h_c = 160$  and a pocket depth of  $h_p = 100$  nm (device geometry  $G_2$ ). A) Lateral position plots of a  $d = 60$  nm Au NP trapped by a  $w_p = 250$  nm (dark green) and a  $w_p = 500$  nm (light green) circular pocket and a  $d = 100$  nm (blue) Au NP trapped by  $w_p = 250$  nm circular pocket. B) MSD plots corresponding to the lateral position plots in A). The error bars denote the standard error of the mean values.

$d = 100$  nm in  $w_p = 250$  nm pockets are shown in Fig. 5.4A. These scatterplots underline the influence of geometrical parameters and particle net charges on the spatial confinement of the particles. As expected, a smaller trap width of  $w_p = 250$  nm confines the particle to smaller dimensions in comparison to larger  $w_p = 500$  nm ones. Moreover, the 100 nm particles, carrying a higher net charge of  $\sim -258 e$  compared to the  $\sim -92 e$  of 60 nm particles, experience a stronger trapping by the pockets with the same diameter (see Supplementary Movie 1). The radial symmetry of the scatterplots verifies the high replica mold fabrication quality of the lateral dimensions of the pockets as also shown from SEM inspection (Fig. 5.3C). To quantify the trapping strength, the 2D mean-square displacement (MSD),  $\langle [\Delta r(\Delta t)]^2 \rangle$ , was evaluated as a function of lag time  $\Delta t$  for each series of acquired frames for a trapped particle (Fig. 5.4). For a particle with restricted diffusion, the MSD reaches a plateau for lag times much higher than its relaxation time  $\tau_r$  in the potential well (the time a non-trapped particle would take to freely diffuse across a distance corresponding to the width of the potential well) [141]. For a harmonic potential, the plateau of the MSD is directly correlated to the radial trap stiffness  $k_r$  as [7, 159]

$$\langle [\Delta r]_p^2 \rangle = \frac{4 k_B T}{k_r} \quad (5.1)$$



where  $k_B$  is the Boltzmann constant and  $T$  is the absolute temperature. For the 60 nm particles trapped by the  $w_p = 500$  nm pockets in a  $G_2$  device, a radial trap stiffness of  $k_r = 0.22 (\pm 0.06)$  fN nm<sup>-1</sup> was obtained. Decreasing the trap diameter to  $w_p = 250$  nm confined the motion of the 60 nm particles stronger and thus increased the trap stiffness to  $k_r = 0.8 (\pm 0.3)$  fN nm<sup>-1</sup>, as expected. The 100 nm particles trapped by the same pockets of  $w_p = 250$  nm experienced an even stronger trap stiffness of  $k_r = 2.9 (\pm 0.9)$  fN nm<sup>-1</sup> due to their higher net surface charge. We would like to point out that we observed no trap stiffness variation along the width of the nanofluidic channels showing that there is no roof sagging towards the middle of the channel width (Supplementary Information 5.7.1).

In addition to the lateral confinement of the electrostatic potentials, we evaluate their depth by measuring the mean residence time  $\bar{\tau}_K$  (Kramers time), defined as the average time a particle dwells inside a trap before escaping. For a harmonic potential, the Kramers time is given by

$$\bar{\tau}_K \cong \tau_R e^{\frac{Q}{k_B T}} \quad (5.2)$$

where  $k_B T$  is the thermal energy and  $Q = q \Delta\Psi$  the potential depth with  $q$  the surface net charge of the particle and  $\Delta\Psi$  the electrostatic potential difference between center of the trap and a position outside the trap in the nanofluidic channel [17, 142, 143]. We quantitatively analyzed the mean residence time by monitoring 100 – 300 escaping events for each particle size in various pocket and device geometries at a monovalent ionic concentration of  $c_0 = 0.1$  mM. In this procedure,  $\bar{\tau}_K$  is extracted from the “residence time probability distribution”,  $p(\tau)$ , which decays exponentially with the residence time  $\tau$  of the individual particles as [143]:

$$p(\tau) = A e^{-\frac{\tau}{\bar{\tau}_K}}. \quad (5.3)$$

Measured  $p(\tau)$  are illustrated in Fig. 5.5A – F and the corresponding  $\bar{\tau}_K$  obtained from these graphs are plotted in Fig. 5.5G. For different particle sizes trapped in the same geometry of  $h_c = 210$  nm,  $h_p = 70$  nm ( $G_1$ ) and with a pocket width of  $w_p = 500$  nm, smaller particles escape faster from the potential wells. 60 nm Au NPs carrying a net charge of  $\sim -92 e$  quickly escaped from the traps with a very short Kramers time of  $\bar{\tau}_K = 0.073 (\pm 0.012)$  s. By increasing the diameter of the particles to 80 nm, carrying a higher net charge of  $\sim -168 e$ , the Kramers time was increased to  $\bar{\tau}_K = 0.242 (\pm 0.037)$  s and further to  $\bar{\tau}_K = 2.70 (\pm 0.36)$  s for 100 nm gold particles with a net charge of  $\sim -258 e$ . Experimentally, we find an over-exponential increase of the Kramers time as a function of particle diameter. To obtain the potential depths

$$Q \cong \ln\left(\frac{\bar{\tau}_K}{\tau_R}\right) k_B T \quad (5.4)$$

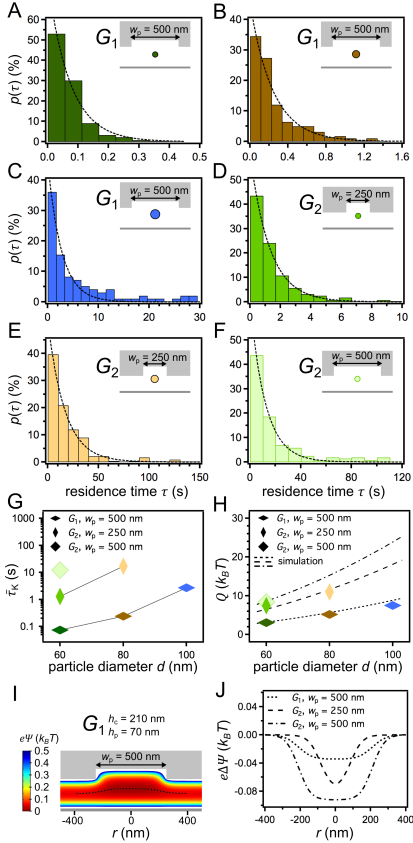


**Figure 5.5.:** Residence time measurements. A-F) Histograms of the residence time probability distribution showing the exponential decay of the residence times of trapped Au NPs in different device geometries (dashed lines are exponential fits) at a concentration of  $c_0 = 0.1$  mM. A-C) 60 nm (dark green, A), 80 nm (dark brown, B) and 100 nm (blue, C) Au NPs trapped in devices with a nanofluidic channel height of  $h_c = 210$  nm, a pocket depth of  $h_p = 70$  nm (device geometry  $G_1$ ) and a width of  $w_p = 500$  nm,  $N = 278, 281$  and  $104$  trapping events. D-E) 60 nm (middle green, D) and 80 nm (brown, E) Au NPs trapped in  $G_2/w_p = 250$  nm,  $N = 290$  and  $235$  trapping events. F) 60 nm Au NPs trapped in  $G_2/w_p = 500$  nm,  $N = 275$  trapping events. G) Kramer's time corresponding to the histogram distributions of A)-F) as a function of particle diameter. H) Potential depths  $Q$  in  $k_B T$  as a function of particle diameter calculated from the experimentally obtained Kramer's time and from simulations (dashed lines). I) Simulation of the electrostatic potential of a point charge of  $-1 e$  by solving the nonlinear Poisson-Boltzmann equation numerically for the device geometry  $G_1$  and a pocket width of  $w_p = 500$  nm. J) Extraction of the electrostatic potential difference of a point charge of  $-1 e$  for the device geometry  $G_1/w_p = 500$  nm,  $G_2/w_p = 250$  nm and  $G_2/w_p = 500$  nm as a function of  $r$  along the axial energy minimum (black dashed line in I)).

Device design	Device geometry $h_c, h_p$ (nm)	Trap diameter $w_p$ (nm)	Particle diameter $d$ (nm)	Diffusion coefficient $D$ ( $\mu\text{m}^2\text{s}^{-1}$ )	Radial stiffness $k_r$ (fN/nm)	Relaxation time $\tau_R$ (ms)
$G_1$	210, 70	500	60	6.38	0.18	3.5
		500	80	5.23	0.55	1.4
		500	100	4.17	0.64	1.5
$G_2$	160, 100	250	60	6.38	0.81	0.8
		250	80	5.23	2.61	0.3
		500	60	6.38	0.22	2.9

**Table 5.1.:** Relaxation times  $\tau_R$  for 60, 80, 100 nm gold particles in different trap geometries. The diffusion coefficients  $D$  were measured using a dynamic light scattering system.

of each system, the relaxation time  $\tau_R$  was determined by the experimentally measured trap stiffness  $k_r$  and the Diffusion coefficients  $D$  of the particles (see Tab. 5.1). In a harmonic potential,  $\tau_R$  is related to the trap stiffness  $k_r$  and the Diffusion coefficients  $D$  of the particles as [7, 144]

$$\tau_R = \frac{k_B T}{D k_r} \quad (5.5)$$

where  $D = k_B T / 3\pi\eta d$  for a particle with diameter  $d$  in a solution of dynamic viscosity  $\eta$ .

For the 60 nm Au NPs trapped in the  $G_1$  devices, only a potential depth of about  $Q \cong 3.0 k_B T$  is required to be released from the 500 nm pockets, explaining the fast escape of the particles from the trap. The potential depth is increased to  $Q \cong 5.2 k_B T$  and  $Q \cong 7.5 k_B T$  for the 80 and 100 nm Au NPs carrying a higher net charge. From simulating the electrostatic potential of a point charge by solving the nonlinear Poisson-Boltzmann equation numerically [17] (COMSOL Multiphysics 4.2, see Fig. 5.5I and J and Supplementary Information 5.7.6) we can extract the potential depths for the given geometry as a function of the particle size (dashed lines in Fig. 5.5H). For the simulations, a mean surface charge density of the particles was taken from measurements of  $\sigma_p = 8 \cdot 10^{-3} e \text{ nm}^{-2}$  and a surface charge density of the substrate glass and PDMS were estimated from spontaneous ionization in water of about  $\sigma_s \sim 3 \cdot 10^{-3} e \text{ nm}^{-2}$  [107]. The experimental results and the good agreement with the simulations show that the Kramers time increases over-exponentially with the particle diameter. Taking Eq. 5.2 and Eq. 5.5, this can be confirmed by the proportionality of  $\bar{\tau}_K$  as

$$\bar{\tau}_K \cong \frac{k_B T}{D k_r} e^{\frac{q \Delta \Psi}{k_B T}} \propto \frac{e^{\alpha d^2}}{d} \quad (5.6)$$

assuming the net surface charge  $q$  of the particles is proportional to  $d^2$ , the diffusion coefficients  $D$  inverse proportional to  $d$ , and the stiffness  $k_r$  proportional to  $d^2$  ( $q \Delta\Psi(r) = k_r r^2/2$ ) [103]. A stable trapping longer than a few seconds in geometry  $G_1$  ( $h_c = 210$  nm and  $w_p = 70$  nm) devices and at an ionic concentration of  $c_0 = 0.1$  mM was only possible for the 100 nm particles. For creating deeper potential wells, the height  $h_c$  of the nanofluidic channel and the depth  $h_p$  and width  $w_p$  of the pockets are important geometrical parameters to vary. Decreasing the channel height results in deeper potentials and thus longer trapping times of the particles as well as increasing of the potential depth.

By fabricating a second design of GIE trapping devices with a reduced nanofluidic channel height of  $h_c = 160$  nm and slightly deeper pockets of  $h_p = 100$  nm (device geometry  $G_2$ ), 60 to 100 nm particles could be stably trapped by the pockets as seen in the iSCAT images of Fig. 5.1B. The residence time probability distribution plots for the 60 nm Au NPs trapped in pocket widths of  $w_p = 250$  nm and 500 nm and for the 80 nm Au NPs trapped in a pocket width of  $w_p = 250$  nm are shown in Fig. 5.5D – F. For the 60 nm and 80 nm particles trapped in the  $w_p = 250$  nm pockets, Kramer times of  $\bar{\tau}_K = 1.28 (\pm 0.05)$  s and  $\bar{\tau}_K = 16.8 (\pm 0.3)$  s were obtained with a corresponding potential depth of  $Q \cong 7.4 k_B T$  and  $Q \cong 10.9 k_B T$ . Trapping the 60 nm particles in  $w_p = 500$  nm pockets (same pocket width as for the device geometry  $G_1$ ), the Kramers time was increased to  $\bar{\tau}_K = 12.2 (\pm 0.3)$  s resulting in a potential depth of  $Q \cong 8.3 k_B T$ . For the same pocket width, this is a  $165 \times$  increase of the Kramers time compared to the  $\bar{\tau}_K = 0.073 (\pm 0.012)$  s measured in the  $G_1$  devices. The experimental observations confirm that particles trapped in pockets with a larger diameter have longer trapping times caused by a deeper potential (up to a certain limit) and lower counts per time of hitting the potential boundaries, due to the longer relaxation times within the larger pockets. The quantitative analysis of the Kramers time and potential depth requires statistics of many escaping events. Since for the second device design  $G_2$ , the 80 nm particles in the  $w_p = 500$  nm pockets and the 100 nm particles in the  $w_p = 250$  nm and 500 nm pockets were stably trapped for several minutes to days the corresponding potential depths could be obtained only by simulations. For the 100 nm particles trapped by the  $w_p = 250$  nm pockets in a  $G_2$  device, a potential depth of  $Q \sim 18 k_B T$  can be estimated which corresponds to a Kramers time of about  $\bar{\tau}_K \sim 10$  h. When trapped in the  $w_p = 500$  nm pockets, potential depths of  $Q \sim 24 k_B T$  are calculated resulting in an extremely long Kramers time beyond experimental demands.

### 5.3.3. Tunable trapping by elastic deformation

In contrast to rigid materials, such as silicon and glass, PDMS is an elastomer that can be compressed and bent easily [180]. This provides new advantages in addition to its low-cost fabrication as discussed in previous sections. We use this unique feature of our nanofluidic system to tune the channel heights  $h_c$  and hence the trap stiffness and potential depth. Compressing the PDMS part of the devices by using mechanical forces, modifies the nanofluidic channel height and thus allows for an additional *in situ* tuning of the trap stiffness and residence times. By applying a compression pressure on the PDMS, valves and pumps in devices have been realized by e.g. pneumatic pressure [181–183], torque actuation from embedded screws [184] or solenoids [185] to open and close microfluidic channels.

To apply a mechanical deformation, a precision screw and a silicon plate were used as sketched in Fig. 5.6A and B. The compression distance and the elastic modulus of the PDMS of about  $E = 3.6$  MPa [175] was used to quantify the pressure exerted on the device. The result for an individual 100 nm Au NP trapped in a  $w_p = 250$  nm pocket at an initial nanofluidic channel height of  $h_{c,0} = 160$  nm and a pocket depth of  $h_p = 100$  nm (device geometry  $G_2$ ) is shown in Fig. 5.6C. If no compression pressure was applied on the PDMS device ( $P = 0$  kPa), a radial stiffness of  $k_{r,0} = 3 \cdot 10^{-3}$  pN nm $^{-1}$  was measured. Applying a stepwise deformation pressure on the PDMS device of about  $\Delta P \sim 10$  kPa each step, resulted in the reduction of the nanofluidic channel height of about  $\Delta h_c(\Delta P) \sim 25$  nm and thus to a stronger trap stiffness. The nanofluidic channel heights were derived by estimating the radial trap stiffness  $k_{r,\text{sim}}$  for different simulated channel heights according to  $q \Delta \Psi = k_{r,\text{sim}} r^2 / 2$  as shown in Fig. 5.6D and comparing  $k_{r,\text{sim}}$  with the experimentally obtained trap stiffness (Fig. 5.6E). Here,  $q \Delta \Psi$  represents the electrostatic energy for a point charge  $q$  of  $-258 e$ . During the approach (reduction of channel height), the particle was further laterally and axially confined, which can be seen in the decrease of the radial displacement and the corresponding MSDs in Fig. 5.6C, the Supplementary Information 5.7.4, and the Supplementary Movie 2. At  $P = 50$  kPa, the radial trap stiffness increased  $45\times$  to  $k_{r,50} = 0.09$  pN nm $^{-1}$ . At this trap stiffness, corresponding to a channel height of less than 40 nm, a potential depth of more than  $Q_{\text{max}} \sim 200 k_B T$  was obtained from our simulations. Additionally, since a smaller nanofluidic channel height than the actual particle diameter was estimated, the particle could be trapped electrostatically as well as geometrically, a remarkable advantage compared to chip-based devices made from rigid materials. This process could be reversed, proving the contact-free nature of the trapping method, by releasing the pressure and going back to  $P = 0$  kPa, resulting in a less confined particle with the initial radial trap stiffness of

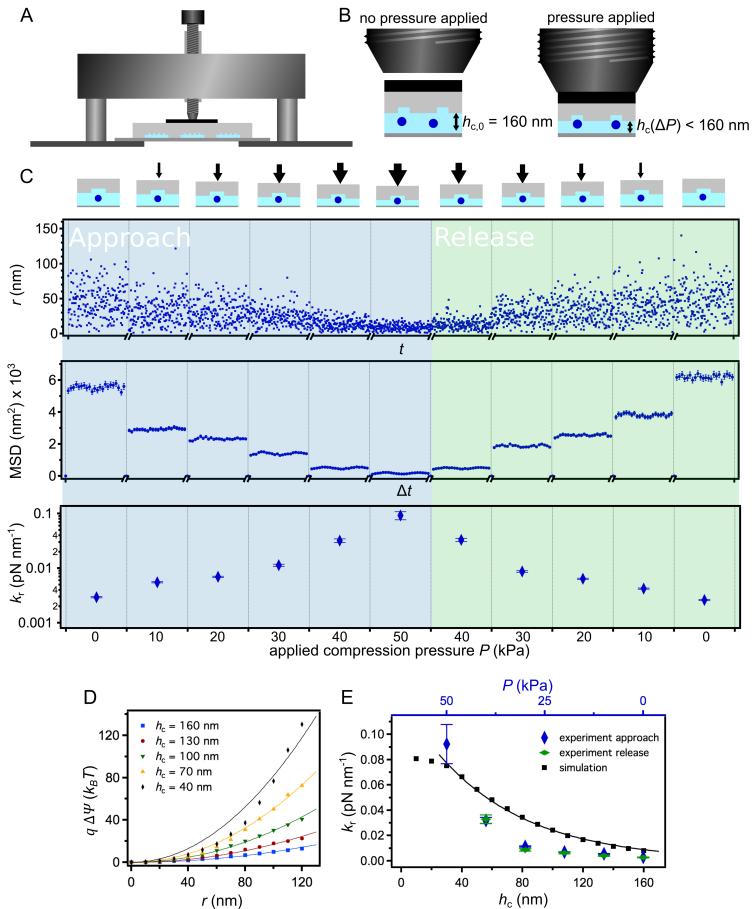


**Figure 5.6.:** Active manipulation of trapping performance by elastic deformation of the PDMS device. A) Sketch of the experimental setup using a precision screw to apply an axial compression force onto the PDMS device. B) Magnified area of A), illustrating the height change of the nanofluidic channel when a compression force is applied to the device. C) Active manipulation of the trapping strength of a  $d = 100$  nm Au NP trapped in a  $w_p = 250$  nm circular pocket at an initial nanofluidic channel height of  $h_{c,0} = 160$  nm and a pocket depth of  $h_p = 100$  nm. In the top graph the radial fluctuations  $r$  of the particle are plotted as a function of time  $t$  at different applied pressures. The corresponding MSDs are shown in the middle graph as a function of the lag time  $\Delta t$ . The obtained radial trap stiffnesses from the MSDs are plotted in the lower graph as a function of the applied compression pressure  $P$ . Increasing the compression pressure of to the PDMS results in a nanofluidic channel height reduction and thus higher trapping strength. D) Radial trap stiffness fits on simulations of the electrostatic energy along the axial energy minimum for a point charge of  $q = -258 e$  (100 nm particle) for different nanofluidic channel heights  $h_c$ . E) Comparison of measured and simulated values of the radial trap stiffness  $k_r$  as a function of applied compression pressure  $P$  and nanofluidic channel height  $h_c$ .

about  $k_{r,0} = 3 \cdot 10^{-3}$  pN nm<sup>-1</sup> (Fig. 5.6C and E).

## 5.4. Discussion

Our results demonstrate that deeper potential depths as the required  $10 k_B T$  for stable trapping can be obtained by geometry induced electrostatic trapping in soft matter devices. For potential depths  $< 10 k_B T$  trapping times of only milliseconds to some seconds were observed, whereas reliable trapping of Au NPs was achieved from several seconds up to hours and days if the potential depths exceeded  $10 k_B T$ . Furthermore, the unique feature of soft PDMS devices to manipulate the nanofluidic channel height by an applied pressure enables straightforward tuning of the chip performance during the experiment and thus opens the capability of active trapping and releasing of nanoparticles. The performance of current chip-based GIE trapping devices made from rigid SiO<sub>x</sub> materials however is characterized by their initial fabricated geometric parameters, especially the nanofluidic channel height. In addition, achieving trapping potentials of more than  $Q_{\max} \sim 200 k_B T$  and having the possibility of trapping the Au NPs geometrically could make the trapping of smaller nano-objects in physiological buffer conditions possible. Tuning the nanofluidic channel height during the experiments gives the possibility to load a particle solution without clogging, followed by trapping the particles by an applied pressure while still having the option to change the condition of the solution by an integrated flow fluidic system or by diffusion. Krishnan reported that even uncharged particles might be trapped in the nanofluidic indentations within potential depths  $> 10 k_B T$ , if the ratio of the particle diameter and the nanofluidic channel height  $d/h_c$  is larger than about 0.6 [116]. This effect was explained by the repelling of the particle from the nanofluidic channel into the trap caused by the counterions entropy of the charged channel walls. Thus, the feasibility to manipulate the nanofluidic channel heights during the experiment down to the size of the particle diameters may extend the PDMS-based trapping method for trapping even uncharged particles. For nanofluidic channel heights smaller than  $\sim 50$  nm, the simulated electrostatic energies scale slightly different from the predicted correlation  $q \Delta\Psi = k_{r,\text{sim}} r^2 / 2$  (see Fig. 5.6D). For such small channel heights, the potential energy landscape might deviate from a perfect harmonic potential, caused by the reduced axial dimension but still constant lateral dimension of the trap width. Additionally, the simulated trapping strengths deviate from our experimentally explored stiffnesses as seen in Fig. 5.6E. We note that for the simulations no external fit parameters were used and that the simulations are based on the obtained mean values,

described in Section 5.3.2. The experiment in Fig. 5.6 demonstrates the behavior of an individually trapped Au NP. Thus, the uncertainties in the particle size and charge and in the correlation between the applied pressure and nanofluidic channel height are the main reasons for this deviation. At small channel heights further effects such as the finite size of the particle and the effect of entropic trapping play an additional role. These effects could be studied in future experiments by exploring the variation of each effect individually.

From the viewpoint of implementation, such systems can have a great impact in the field of nanofluidics since the flexibility and low cost of fabrication bypasses the need for cleanroom facility for top-down processes. Moreover, the present method is integrated with the well-established microfluidic techniques and infrastructure, enabling the integration of GIE trapping nanofluidic devices with more complex fluidic systems such as particle sorting or trapping along concentration gradients [124]. Demonstrating that GIE trapping devices can be fabricated from replica molding processes opens additionally the possibility for fabricating such systems out of a variety of new materials. As an example, GIE trapping devices made from polystyrene foils and UV-curable adhesives could be used for X-ray scattering such as free-electron-laser studies [186, 187].

## 5.5. Conclusion

We present nanofluidic trapping devices made from the elastomeric material PDMS for high-throughput fabrication and high performance contact-free passive trapping of single charged nano-objects. These devices consist of fluidic channels that are  $\sim 160$  nm in height but several micrometers in width, enabling the trapping of multiple single particles in parallel by fabricating trap lattices within the channels. Analyzing the lateral motion and residence times of the particles, we could obtain both, the trap strength and the potential depths of our traps experimentally supported by simulations. For the as-fabricated device geometries (i.e. without exerted pressure), we found potentials of the electrostatic traps as deep as  $Q \cong 24 k_B T$ , corresponding to stable trapping times of many days. We were able to actively tune the nanofluidic channel heights by applying a mechanical compression pressure and thus varying the trap stiffness and potential depths in situ. With this feature that is not possible in rigid SiO<sub>x</sub>-based devices, remarkable deep potentials of  $Q_{\max} \sim 200 k_B T$  and high trap stiffness of more than  $k_{r,\max} = 0.09$  pN nm<sup>-1</sup> were achieved. Realizing such high potential depths could facilitate practical implementation of trapping devices for in situ isolation of fundamental biological entities such as macromolecules in physiological buffer conditions.



Due to its ease of fabrication, our method opens the feasibility to carry out single and label-free particle research using the GIE trapping method with little effort.

## 5.6. Acknowledgments

This work was funded by the Swiss Nanoscience Institute in Basel, Switzerland (SNI PhD graduate school, Project P1202). We would like to thank the technical staff of the Laboratory for Micro- and Nanotechnology at the Paul Scherrer Institut, Switzerland. Further, we want to thank Celestino Padeste and Victor Cardaso for their technical help and fruitful discussions.

Supplementary information accompanies the manuscript on the Microsystems & Nanoengineering website <http://www.nature.com/micronano>.

## 5.7. Supplementary Information

### 5.7.1. Sagging of PDMS nanochannels

A key advantage of PDMS is the possibility of actively tuning the nanofluidic channel height and therefore the trapping stiffness and potential depth by applying a compression pressure to the device. If no pressure is applied to the PDMS device, however, the design of the chip and the fabrication process including a stiffer PDMS mixture, loading of the sample solution before binding and the supporting pillars should prevent the PDMS from sagging towards the middle of the channel width (Fig. 5.7A). To investigate roof sagging of the PDMS nanofluidic channels, the trap stiffness at the positions 2, 4, 6 and 8  $\mu\text{m}$  along the width of the channel were measured using Au NPs of  $d = 100$  nm trapped in  $w_p = 250$  nm pockets and at a channel height of  $h_c = 160$  nm and pocket depth of  $h_p = 100$  nm (device geometry  $G_2$ ). In Fig. 5.7B the mean trap stiffness of the particles at the different positions along the nanofluidic channel is shown. Since there was no increase in the trap stiffness towards the center of the nanochannel observed and the trapping stiffnesses were constant along the channel width, roof sagging of the nanochannel along the 10  $\mu\text{m}$  width can be excluded. Pure scattering standard bright field microscopy (DMI 5000 M, Leica Microsystems) equipped with a 100  $\times$ , 1.3 NA oil-immersion objective (HCX PL FLUOSTAR, Leica Microsystems) and an additional 1.5  $\times$  internal tube lens (11 888 699, Leica Microsystems) was used to measure multiple Au NPs at the same time with a field of view of  $22 \times 22 \mu\text{m}^2$  at an exposure time of 0.1 ms and an acquisition rate of 199 Hz using a sCMOS camera (Neo 5.5 sCMOS, Andor Technology Ltd, Belfast BT12 7AL, UK).

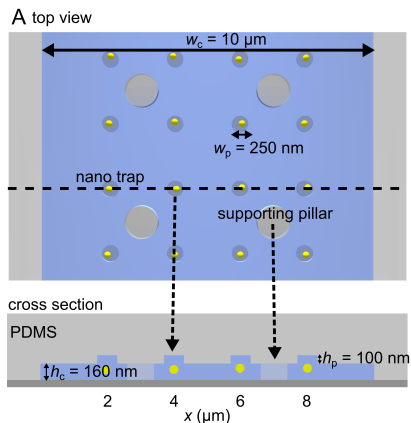
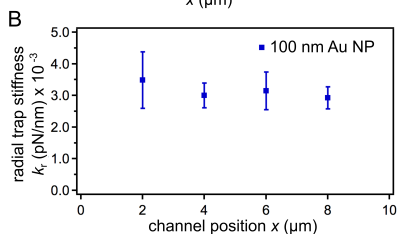


**Figure 5.7.:** A) Top and side view of a nanofluidic trapping channel with the integrated circular pockets and supporting pillars. The circular pockets have a distance of  $2 \mu\text{m}$  from each other and are placed at the positions 2, 4, 6 and  $8 \mu\text{m}$  along the width of the channel. B) Mean radial trap stiffness measurements of 100 nm Au NPs trapped in  $w_p = 250 \text{ nm}$  pockets at different positions along the width of the nanofluidic channel with a height of  $h_c = 160 \text{ nm}$  and a pocket depth of  $h_p = 100 \text{ nm}$ .



### 5.7.2. Device fabrication

All features were patterned on a silicon wafer with a thermally grown SiO<sub>2</sub> layer of 400 nm thickness (Fig. 5.8A). To etch the microfluidic reservoir channels, inlets, outlets and the alignment markers, a chromium layer of 120 nm (Univex 450, Leybold GmbH, 50968 Koeln, Germany) was first evaporated, which served as a hard mask during the RIE etching of the deep channels. After spin-coating a photoresist (Microposit S1813, Dow (Shipley), Newark, DE 19713, USA; 2000 rpm, 500 rpm/s, 40 s) and UV-light exposure (Suess MA 6, Suess Microtec AG, 85748 Garching, Germany;  $\lambda = 365$  nm, 120 mJ/cm<sup>2</sup>, 12 s) using a chromium mask (Compugraphics Jena GmbH, 07751 Jena, Germany) with the design of the microfluidic system, the wafer was developed in MF-24A (Shipley, Megaposit MF-24A, Dow (Shipley)) for 40 s. The structures were etched through the chromium layer (BMP Plasmatechnology GmbH, O<sub>2</sub>:Cl<sub>2</sub> with a ratio of 5:1) and further etched 3  $\mu$ m into the SiO<sub>2</sub> (Ar 38 sccm, CHF<sub>3</sub> 12 sccm, 100 W) and Si (SF<sub>6</sub> 4 sccm, CHF<sub>3</sub> 30 sccm, O<sub>2</sub> 3 sccm, 100 W) substrate using RIE (Oxford 100, Oxford Instruments plc, Abingdon, Oxfordshire OX13 5QX, UK) as shown in Fig. 5.2B and Fig. 5.8B. The remaining resist was removed in acetone and the wafer was cleaned in a piranha bath (H<sub>2</sub>SO<sub>4</sub>(%):H<sub>2</sub>O<sub>2</sub>(%) = 2:1) for 20 min at 90°C. The remaining chromium was dissolved in chromium mask etchant (Chrome ETCH No. 1, Microchemicals GmbH, 89079 Ulm, Germany) and the wafer was rigorously rinsed in DI water and dried under a nitrogen air stream. To further fabricate the nanofluidic GIE trapping region, a new chromium layer of 25 nm was evaporated on the silicon wafer. This layer was again used as a hard mask for RIE etching. After spin-coating PMMA (PMMA 950k, Allresist GmbH, 15344 Strausberg, Germany; 4 % ethylacetate; 4000 rpm, 1000 rpm/s, 60 s) on the chromium layer, the design of parallel channels of 10  $\mu$ m width and 0.5 mm length including supporting pillars were exposed using e-beam lithography (Vistec EBPG 5000 Plus, Vistec Electron Beam GmbH, 07743 Jena, Germany), developed in a mixture of methyl isobutyl ketone and isopropyl alcohol (MIBK:IPA = 1:2 (v/v), 60 s) and etched into the chromium hard mask using BMP. After removing the PMMA layer in acetone, the channels were further etched 160 nm or 210 nm deep into the silicon dioxide layer, using RIE as shown in Fig. 5.8C. The hard mask was removed in the chromium mask etchant. These steps were repeated to etch the actual nano-traps, circular pockets with a diameter of 200 – 500 nm, 70 – 100 nm deep into the surface of the existing channels (Fig. 5.8D). The wafer was cleaned in a freshly made piranha solution (H<sub>2</sub>SO<sub>4</sub>(%):H<sub>2</sub>O<sub>2</sub>(%) = 2:1 (v/v)) and silanized (mixture of trichloro(1H, 1H, 2H 2H-perfluorooctyl)-silane and (tridecafluoro-1,1,2,2-tetrahydrooctyl) dimethylchlorosilane with a ratio of 1:1 (v/v)) in an evacuation chamber. The silicon wafer then served as a master to fabricate several OrmoStamp<sup>®</sup>-based negative masters. Before each replica

molding step from the silicon master to OrmoStamp<sup>®</sup>, a new silanization of the silicon master was carried out to insure high quality OrmoStamp<sup>®</sup> masters and non-sticking to the silicon wafer. In the second main step, a cleaned 700  $\mu\text{m}$  thick borofloat glass wafer (Borofloat<sup>®</sup> 33, 700  $\mu\text{m}$ , Schott AG, 55122 Mainz, Germany) was plasma activated for 2 min (Oxford 80, Oxford Instruments plc, O<sub>2</sub> 20 sccm, 20 W), spincoated with an adhesion layer (OrmoPrime<sup>®</sup>, micro resist technology GmbH, 4000 rpm, 45 sec) for better adhesion of the OrmoStamp<sup>®</sup> resin to the glass wafer and baked at 180°C for 5 min. A 2 ml droplet of OrmoStamp<sup>®</sup> hybrid polymer was placed in the middle of the silicon wafer and the glass wafer was gently aligned upside down onto the droplet and left for about 30 min until the droplet reached the edge of the two wafers. Then the silicon-OrmoStamp<sup>®</sup>-glass stack was placed under a UV lamp (ELC-500, Electro-Lite Corporation, Bethel, CT 06801, USA) for 10 min to cure the hybrid polymer. After detaching the two wafers, a negative OrmoStamp<sup>®</sup>-glass wafer was received. Each OrmoStamp<sup>®</sup> wafer was silanized (mixture of trichloro(1H, 1H, 2H 2H-perfluorooctyl)-silane and (tridecafluoro-1,1,2,2-tetrahydrooctyl) dimethylchlorosilane with a ratio of 1:1 (v/v)) once in an evacuation chamber before the first PDMS replica molding. The OrmoStamp<sup>®</sup> wafer was used in the third main step as a negative master to obtain the PDMS-based devices. To reduce sagging and roof collapse of the thin nanometer height fluidic channels, PDMS was mixed at a ratio of 5:1 (prepolymer : crosslinker) to achieve a higher elastic modulus [ $E = 3.6$  MPa [175]] and degassed in a vacuum chamber to remove air bubbles. The PDMS devices were cured on a hotplate at 150°C for 3 h which reduced the viscosity of the PDMS prepolymer before crosslinking to achieve high resolution replication into PDMS [176, 177]. The PDMS was removed from the OrmoStamp<sup>®</sup> master and devices were cut out using a scalpel. Finally, inlet and outlet reservoirs of 4 mm diameter were punched into the PDMS device as seen in Fig. 5.2B.

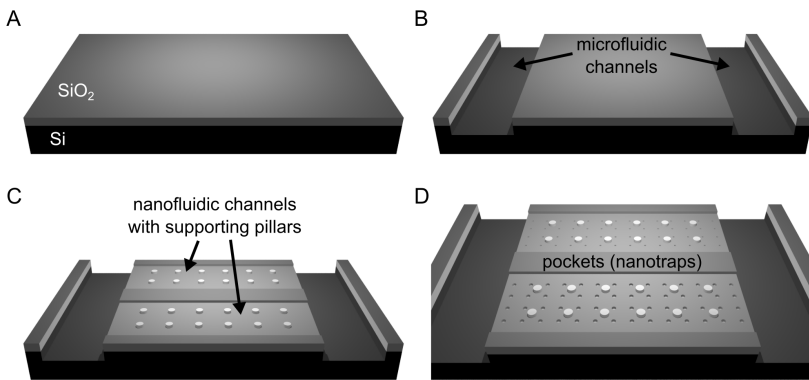


**Figure 5.8.:** Schematic of the fabrication steps of the silicon master showing the microfluidic channels, nanofluidic GIE trapping region and the actual nanotraps.

### 5.7.3. High contrast and SNR imaging using PDMS

Interferometric scattering detection (iSCAT) is used for many applications as a detection method, since it provides high sensitivity and nanometer precision detection of nano-objects down to 5 nm in diameter [19, 20, 120]. In our device configuration, the iSCAT signal is based on the interference between the scattered light from a particle and a reference beam reflected from the water-solid interface. The interference signal scales with the third power of the object diameter ( $d^3$ ) whereas the pure scattering signal is proportional to  $d^6$ .

In comparison to glass-based devices [156], PDMS also has the key advantage that it is transparent from UV to IR (240 nm – 1100 nm) with a refractive index of  $\sim 1.4$  [188] in the visible range, making it possible to enclosure fluidic optical components and highly suitable for high signal-to-noise detection using iSCAT imaging. The background intensity in PDMS-based GIE trapping devices originates mainly from the reflected field of the glass-water interface  $E_{r1}$  and the water-PDMS interface  $E_{r2}$  with a reflectivity of  $R_1 = 0.26\%$  and  $R_2 = 0.11\%$  respectively, as sketched in Fig. 5.9A. Example contrast cross-section of single Au NPs with a diameter of 60, 80 and 100 nm are seen in Fig. 5.9B. We have analyzed over 150 frames of single Au NPs with a diameter 60, 80 and 100 nm each in nanofluidic PDMS channels. The mean contrast and SNR values are shown in the graph in Fig. 5.9C. We would like to point out that, using PDMS-based GIE trapping devices, the contrast and SNR values for detecting Au NPs are comparable to glass based devices and one order of magnitude higher than compared to silicon based devices [156]. This is explained due to the limited incident laser power used in silicon based devices, preventing an overexposure of the camera detector, caused by the high reflection of the Si-SiO<sub>2</sub> interface in the device.

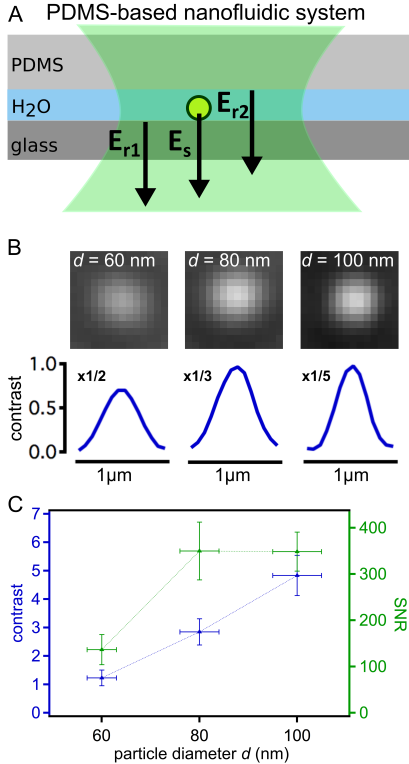


**Figure 5.9.:** A) Schematics of the PDMS-based nanofluidic device demonstrating the path of the incident laser beam (green) and the fields scattered from the nano-object and reflected from the glass-water and water-PDMS interfaces. Similar to glass-based nanofluidic systems, PDMS devices have a reduced reflection of the incident beam, which leads to higher SNR and contrast imaging using iSCAT. B) Example of iSCAT images and the corresponding contrast profiles of 60, 80 and 100 nm gold particles as used in this paper. The contrast profiles were multiplied by 1/2, 1/3 and 1/5 for better visualization. C) Mean contrast and SNR measurements as a function of particle diameter.



### 5.7.4. Reduction of axial movement of the particle at reduced nanofluidic channel heights

Additional to the lateral trajectories, iSCAT imaging provides information on the axial movement of the particle due to the interference signal between the scattered field of the particle and the reflected background field [17, 103, 104, 120]. This information can be extracted from the intensity fluctuation of the particle and thus from the amplitude of each acquired Gaussian profile fit. For the individual trapped particle in Fig. 5.6 of the manuscript, we obtain a decrease of the standard deviation of the intensity fluctuation of the particle for increased compression pressure (see Fig. 5.10). This confirms, that the reduction of the nanofluidic channel height results additionally in a stronger confinement in  $z$ -direction.

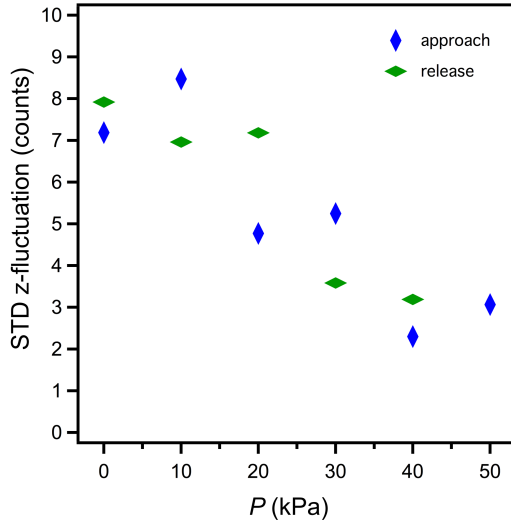


**Figure 5.10.:** Standard deviation of the intensity fluctuation of the 100 nm Au NP trapped at different applied compression pressures.

### 5.7.5. Surface zeta potential measurement of activated glass and PDMS

In glass-based GIE trapping devices, the top and bottom surface layer consist of the same material, which results in an energy minimum at the midplane of the nanofluidic channel without implemented traps. However, PDMS-based GIE trapping devices consist of a top PDMS surface and a bottom glass surface. To determine the charge properties of the glass and PDMS, surface zeta potential measurements were carried out at  $\text{pH} = 6.2$  (Surface zeta potential cell ZEN1020, Malvern Instruments Ltd) using  $1\ \mu\text{m}$  polystyrene beads (micromere 01-54-103, micromod Partikeltechnologie GmbH, 18119 Rostock, Germany). The beads were diluted 1:1000 (v/v) in fresh DI water (18 M $\Omega$ ). After activating a PDMS and glass sample, respectively, the apparent mobility of the tracer particles was measured at several distances away from the surfaces. Close to the surfaces, the tracer mobility is dominated by the electro-osmotic surface flow whereas far from the surface, the electrophoretic motion of the tracer particles itself dominates the mobility. By extrapolating the reported zeta potential values to zero displacement (see Fig. 5.11) and using the equation  $\zeta_{\text{surface}} = -\zeta_{\text{tracer}}(0) + \zeta_{\text{tracer}}(\infty)$ , the surface zeta potentials of the materials were obtained [189]. At  $\text{pH} 6.2$ , a zeta potential of the tracer particles of  $\zeta_{\text{tracer}}(\infty) = -43.8 (\pm 0.9)$  mV was measured. For activated glass and activated PDMS a surface zeta potential of  $\zeta_{\text{surface,glass}} = -79.9 (\pm 0.9)$  mV and  $\zeta_{\text{surface,PDMS}} = -78.2 (\pm 1.2)$  mV was obtained ensuring that the energy minimum in GIE trapping devices made from PDMS and glass as substrates results in the slit midplane of the nanofluidic channels without the trap implementations.

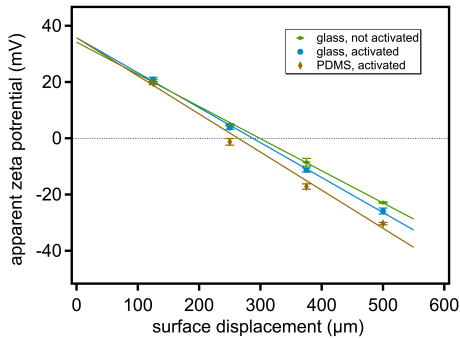


**Figure 5.11.:** Surface zeta potential measurements of non-activated and activated glass and of activated PDMS in water. For activated glass and activated PDMS a similar surface zeta potential of around -80 mV was obtained ensuring that PDMS can be used as a material for GIE trapping devices.

### 5.7.6. Simulation of the electrostatic potentials

The simulated electrostatic potentials of a point charge of  $-1 e$  for all three device geometries (see Fig. 5.12) were obtained by numerically solving the nonlinear Poisson-Boltzmann equation in 3D using the COMSOL Multiphysics package 4.2 (COMSOL) [17]. An ionic strength of a monovalent ionic salt concentration of  $c_0 = 0.1$  mM and a surface charge density of the Au NPs of  $\sigma_p \sim 8 \cdot 10^{-3} e \text{ nm}^{-2}$  were measured and taken as a boundary condition. The surface charge density of the glass and PDMS of  $\sigma_s \sim 3 \cdot 10^{-3} e \text{ nm}^{-2}$  were estimated to fit the simulations to the experimentally observed data in agreement with literature [107].

The circular pockets were rotationally symmetric about the  $r = 0$  axis in the nanofluidic channels. The potential depths  $\Delta Q$  of a point charge of  $-1 e$  were extracted by calculating the energy difference between the minimum potential along the  $z$ -axis for  $r = 0$  nm (center of the pocket, blue dashed lines) and  $r = 400$  nm (midplane of the nanofluidic channels outside the trap potential, red dashed lines).

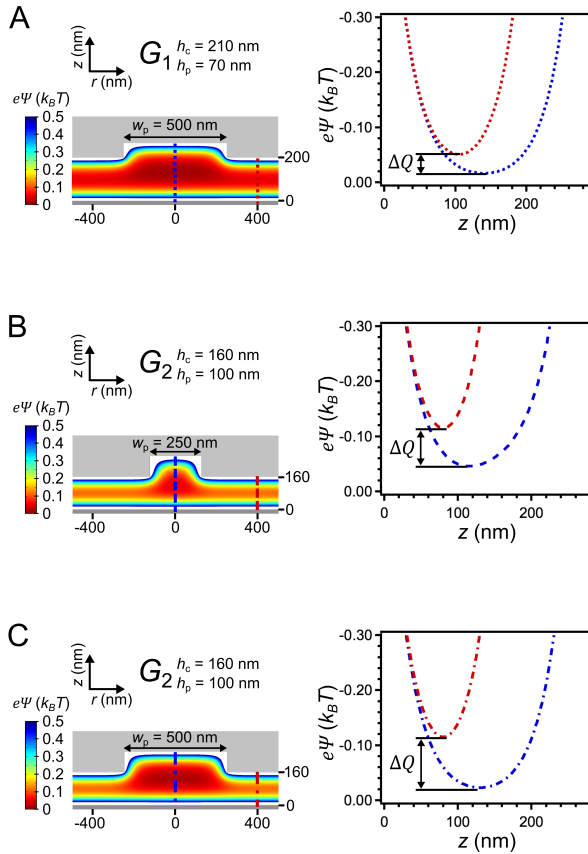


**Figure 5.12.:** Two-dimensional electrostatic potentials and electrostatic energy plots along the  $z$ -axis for  $r = 0$  nm and  $r = 400$  nm for a point charge of  $-1 e$  for the two device geometries and pocket sizes used in the experiments.

## Pneumatic nanofluidic devices for controlled manipulation and contact-free trapping of nanoparticles

*The following section is a manuscript in preparation*

### Pneumatic nanofluidic devices for controlled manipulation and contact-free trapping of nanoparticles

Michael A. Gerspach<sup>a,b,c</sup>, Nassir Mojarad<sup>d,e</sup>, Deepika Sharma<sup>a,b,f</sup>,  
Yasin Ekinici<sup>a,b,\*</sup>, Thomas Pfohl<sup>a,c,g,h,\*</sup>

<sup>a</sup> Swiss Nanoscience Institute, 4056 Basel, Switzerland

<sup>b</sup> Laboratory for Micro and Nanotechnology, Paul Scherrer Institut, 5232 Villigen, Switzerland

<sup>c</sup> Chemistry Department, University of Basel, 4056 Basel, Switzerland

<sup>d</sup> Nanotechnology Group, ETH Zürich, 8803 Rüschlikon, Switzerland

<sup>e</sup> Current employer: ABB Switzerland Ltd., Semiconductors, 5600 Lenzburg, Switzerland

<sup>f</sup> Biozentrum, University of Basel, 4056 Basel, Switzerland

<sup>g</sup> Biomaterials Science Center, University of Basel, 4123 Allschwil, Switzerland

<sup>h</sup> New address: Institute of Physics, University of Freiburg, 79104 Freiburg, Germany

\* corresponding authors: [thomas.pfohl69@gmail.com](mailto:thomas.pfohl69@gmail.com), [yasin.ekinici@psi.ch](mailto:yasin.ekinici@psi.ch)

**Abstract**

Contact-free trapping and manipulation of individual nano-objects in solution is of great scientific interest and remains one of the main and current challenges in nanofluidics. Geometry-induced electrostatic (GIE) trapping is one method that provides stable trapping of charged nano-objects smaller than 100 nm without the need of any external power. However, due to the non-existing external control, there is a lack of active manipulation of the trapped objects during the experiment. Our new trapping devices are fabricated from polydimethylsiloxane (PDMS)-based soft lithography replica molding, which simplifies fabrication resulting in high-throughput and low cost production and makes usage of single particle trapping available with little effort. We describe the development of an implemented 3D PDMS pneumatic system that makes the PDMS-based GIE trapping devices capable of controlling the potential depth and trap stiffness by actively tuning the height of the nanofluidic channel using pneumatic microchannels. Besides tuning the trapping strength, the nano-objects can be actively trapped and released during the experiment.

---

Recent research in nanofluidics shows great interest in developing tools and systems to confine and manipulate nano-objects in a stable and non-invasive manner. The reliable detection and trapping of individual objects provide sensitive information on local dynamics, which leads to a fundamental understanding of biological interactions [92, 190–192] and physical properties of the trapped objects [7, 34, 55]. The precise manipulation of trapped objects found further applications in e.g. surface patterning [58], nanoparticle assembly [59], or sorting of particles [57]. Extensive developments, mainly in active trapping methods such as optical- [47, 49, 50] or plasmonic-tweezers [48, 65, 66, 72, 73], successfully demonstrated stable confinement of single objects, even the contact-free trapping of nano-particles smaller than 100 nm [61]. However, optical-based methods are limited by the polarizability of the trapped object that scales with the third power of the object size and the ratio of the refractive index of the object and that of the medium. Thus, to create strong enough forces to act against the randomization effect in fluids and stably trap particles smaller than 100 nm or biomolecules, high-energy gradient fields are needed which can easily reach the hundred mW range [61] leading to concerns of photothermal damage [62] or heating of the surrounding media [48, 63, 74]. Alternative approaches based on electric fields are the planar Paul trap (PPT) [83, 84] or the anti-Brownian electrokinetic trap (ABEL) [88, 90]. With the PPT, trapping of single polymer spheres of about 500 nm in aqueous [83] and of 100 nm diameter in ethanol solutions [84] were demonstrated. The ABEL trap was even suitable to stably confine single biomolecules such as proteins or DNA strands [90, 92]. However, as for optical tweezers, these methods require externally applied fields or a complex feed-back-loop system, which makes the fabrication and built up of the system more advanced and difficult.

In the last years, one method has attracted the attention for reliable trapping single objects smaller than 100 nm without the need of any external applied power, called geometry induced electrostatic (GIE) trapping [7, 17, 103, 120–122]. GIE trapping relies on the principle of the electrostatic repulsion between a charged object and walls of nanometer height fluidic channels carrying the same sign of charge as the trapped object. The nanofluidic channels contain small circular indentations (pockets) that result in local energy potential wells as seen in Fig. 6.1(a). Depending on the potential depth of these pockets, nano-objects can be stably trapped from milliseconds to several hours and days [17]. Electrostatic trapping was demonstrated for levitating negatively [17, 156] and positively [125] charged gold nanoparticles (Au NPs), lipid vesicles [17] and even for angular depended trapping of silver nano-rods [121]. Further it found concepts in digital information storage [122], and applications in screening the electrostatic potential in salt gradient solutions [124] and to determine the size and charge of Au NPs [7]

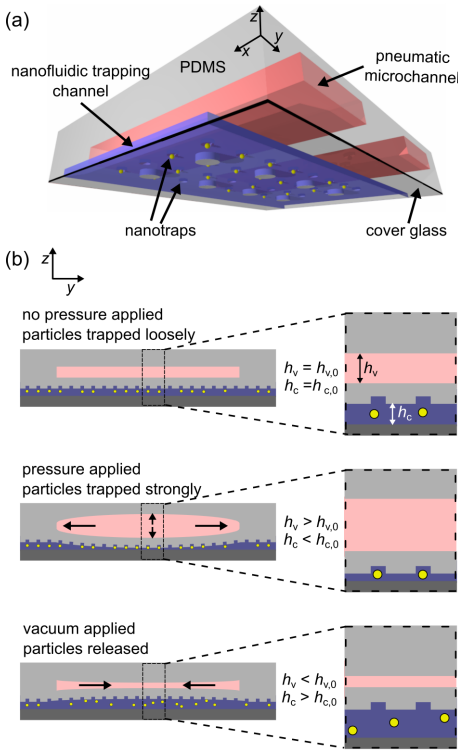


**Figure 6.1.:** (a) Schematic of the PDMS multilayer geometry-induced electrostatic (GIE) trapping device with an integrated air pressure system for manipulating the trapping performance. (b) Working principle of the device: If no pressure is applied in the air microchannel, the particles are loosely confined in the pockets, can exit and enter the trap. If the pressure is increased, the particles are stably trapped since the nanofluidic channel height  $h_c$  is reduced. The particles are fully released if a vacuum is applied in the air microchannel.

or biomolecules [34]. In GIE trapping, the potential depth of the nano-traps can be easily tuned by modifying parameters such as the pocket dimensions or the nanofluidic channel height [103]. However, chip-based GIE trapping devices are mainly fabricated from rigid  $\text{SiO}_x$  substrates (glass or silicon), which defines the performance of the devices by the initial fixed geometric parameters, especially the nanofluidic channel height. Additionally, the required state-of-the-art top-down nano-fabrication tools as electron beam (e-beam) lithography and reactive ion etching (RIE) needed for the fabrication of the devices makes the production time consuming and resource demanding and thus the usage and development of GIE trapping devices difficult. As an alternative, we recently introduced GIE trapping devices made by soft lithography with polydimethylsiloxane (PDMS) used for replica molding (see Chapter 5), which simplifies the fabrication resulting in high throughput and low cost production processes [180, 193–195]. In addition, taking advantage of the elastic nature of PDMS, we demonstrated the tuning of the nanofluidic



---

channel height by applying a mechanical compression pressure to the device using a screw. This resulted in the manipulation of the trap strength and trapping time of the nanoparticles.

In this letter, we report on the contact-free electrostatic trapping of individual Au NPs with a diameter of  $d = 100$  nm and demonstrate active manipulation of the trapping performance during the experiment using an implementing 3D PDMS pneumatic system [181, 182]. Further, applying a rapid pressure change in the pneumatic system makes the devices capable for actively releasing and trapping of Au NPs *in situ*. The fact that the trapping depends only on the electrostatic charge of the channels and objects surface and thus no external applied fields are needed, and the PDMS devices are fabricated using replica molding, results in a simple and low-cost production, which makes a combination with many other techniques straightforward. The design and principle of the device is highlighted in Fig. 6.1(a) and (b). It is made up of a nanofluidic channel with an initial height of  $h_{c,0} = 210$  nm and an upper perpendicular microchannel with a height of  $h_{v,0} = 20$   $\mu\text{m}$  separated by a thin 70  $\mu\text{m}$  membrane. The pockets in the nanofluidic channel had a width of  $w_p = 500$  nm and a depth of  $h_p = 70$  nm. With no additional air pressure applied in the microchannel, the particles in the nanofluidic channels are loosely confined, can enter and exit the traps. Increasing the air pressure in the upper microchannels results in a reduction of the nanofluidic channel height  $h_c < h_{c,0}$  and thus stable and strong trapping of the particles. The particles can be fully released by applying a vacuum, which increases the nanofluidic channel height  $h_c > h_{c,0}$ .

The devices are fabricated with a multilayer soft lithography process as seen in Fig. 6.2. The principle of the devices is based on pneumatic valve and pump systems introduced by the Quake group [181]. For the layers, two separate designs were needed. The first master with the features of the GIE trapping nanofluidic channels and an integrated microfluidic system (Fig. 6.2(a)) was imprinted into a UV curable hybrid polymer (OrmoStamp<sup>®</sup>, micro resist technology GmbH) as described in Chapter 5. The second master for the PDMS pneumatic microchannel system (Fig. 6.2(b)) was fabricated on a silicon wafer using a photoresist (SU-8 2025, Microchem) for the pattern. The photoresist was spin-coated, exposed and developed according to the manufacturer processing guidelines to reach a height of the structures of  $h_{v,0} = 20$   $\mu\text{m}$ . Before the first PDMS replica molding process, both masters were silanized in an evacuation chamber once (mixture of trichloro(1H,1H, 2H,2H-perfluorooctyl)-silane and (tridecafluoro-1,1,2,2-tetrahydrooctyl) dimethylchlorosilane with a ratio of 1:1 (v/v)). PDMS was mixed at a crosslinking ratio of 5:1 (prepolymer : crosslinker), degassed, purred over the silicon master with the pneumatic system and cured at 80°C in the

6. *Pneumatic nanofluidic devices for controlled manipulation and contact-free trapping of nanoparticles*

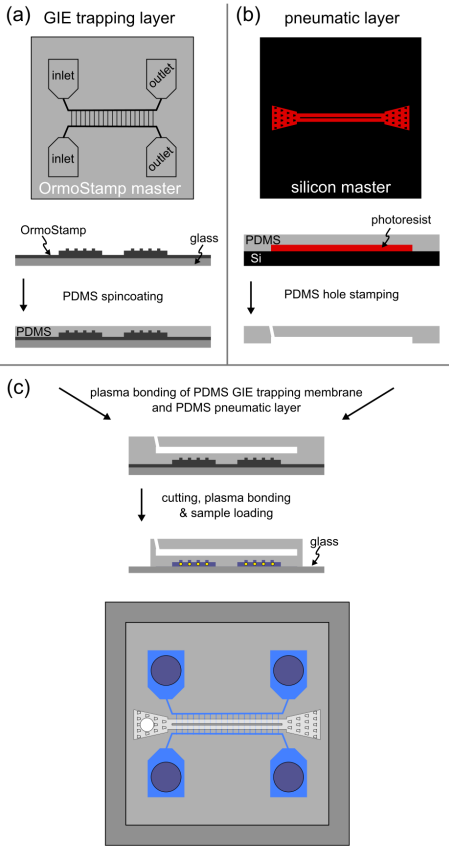


**Figure 6.2.:** Schematic of the fabrication steps. Two separate designs are fabricated for the multilayer PDMS device, a GIE trapping master (a) and an air pressure microchannel master (b). (c) The two layers are combined by covalently binding after air plasma activation to obtain a 3D PDMS trapping device.

oven for 3 h. Meanwhile, fresh PDMS was mixed again at a crosslinking ratio of 5:1, degassed and spin-coated on the OrmoStamp master to obtain a PDMS membrane thickness of about 70  $\mu\text{m}$  (1500 rpm, 30 s). The wafer was cured in the oven for 1.5 h at 80°C. After 3 h, the PDMS on the silicon master was peeled off and one inlet hole was punched into each chip for the connection of the air pressure tubing. After 1.5 h in the oven, the OrmoStamp master including the PDMS and the PDMS part with the pneumatic microchannels were air-plasma activated (Diener electronic, Femto, 0.5 mbar, 80% power, 35 s), aligned, pressed together (Fig. 6.2(c)) and post cured for 1 h at 150°C. To characterize the performance of the devices 100 nm Au NPs were used as probes (BBI solutions, EM.GC100). The solution was centrifuged two times to obtain pellets. The excess water was exchanged with fresh deionized water

(18 M $\Omega$ ) and the pellets were resuspended each time. After a third centrifugation and extraction of the excess water, a dense sample solution of Au NPs of  $\sim 10^{11}$  particles/ml was received. The particles had a net surface charge of  $\sim -258 e$ , measured using a dynamic light scattering system (Zetasizer Nano, Malvern). The final cured PDMS multilayer was cut into single device units, stamped with four holes each unit (fluidic reservoirs) and air-plasma activated together with a cleaned microscope coverslip. Within 1 min after activation, the PDMS unit was loaded with the sample solution and pressed together with the coverslip glass for 1 min to obtain a covalent binding. The reservoirs were finally filled with a 1 mM monovalent buffer solution and the finished device was placed on a microscope holder. A 1.07 mm outer diameter Teflon tubing (Adtech Polymer Engineering Ltd) was inserted into the inlet of the microfluidic air pressure channel of the device. The tubing was connected to a digital manometer (Kobold, MAN-SD) and a flow control unit (SMC Pneumatics, AS1002F-04) for experiments with a constant kept pressure or to a glass syringe (Microsyringes, 250  $\mu$ l) and a pump system (neMESYS, Low Pressure Dosing Module) for dynamic catching and releasing experiments. The particles were recorded using a custom-built interferometric scattering (iSCAT) detection system.

The contact-free electrostatic trapping and manipulation performance of the device is demonstrated in Fig. 6.3. A 100 nm AuNP was trapped in a pocket with a width of 500 nm. The gauge pressure  $p_g$  in the microchannel was increased to 500 mbar and kept to strongly trap the particle. Subsequently the pressure was stepwise reduced by  $\Delta p = -50$  mbar in a controlled manner. At every step, the motion of the particle was recorded as shown by the lateral position plots in the inset of Fig. 6.3(b). The Gaussian form of the radial probability distribution functions  $P(r)$  (Fig. 6.3(a)) obtained from the position plots indicate that the trap can be approximated by a harmonic potential with a radial trap stiffness of  $k_r = \sigma_r^2/k_B T$  which is directly correlated to the Gaussian width  $\sigma_r$ , the Boltzmann constant  $k_B$  and the absolute temperature  $T$ . At a gauge pressure of 500 mbar the particle is strongly confined in the pocket with a radial stiffness of  $k_r = 0.13$  pN/nm as seen in Fig. 6.3(b). Decreasing the air pressure in the microchannel, increases the nanofluidic channel height  $h_c$  and thus confines the particles less, which lowers the trap stiffness  $k_r$ . This behavior is clearly seen from the lateral position plots and the radial probability distribution functions  $P(r)$  at each measured pressure  $p_g$ . At a pressure of 100 mbar, the stiffness is reduced more than two orders of magnitude to  $k_r = 0.6$  fN/nm. The particle finally escaped from the trap as the pressure was lowered to 50 mbar as expected from the geometrical device design. This threshold however can be adjusted by fabricating devices with a lower initial nanofluidic channel height  $h_{c,0}$  (see Chapter 5).

## 6. Pneumatic nanofluidic devices for controlled manipulation and contact-free trapping of nanoparticles

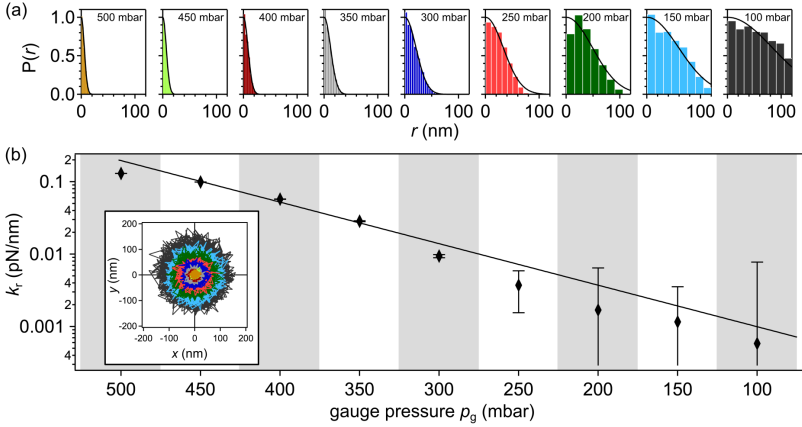


**Figure 6.3.:** The effect of pressure change in the microfluidic air chamber on the trapping strength. (a) Normalized radial probability histograms of a single trapped 100 nm Au NP in a  $w_p = 500$  nm pocket obtained from the  $(x-y)$  position scatterplot (inset in (b)) for different gauge pressures  $p_g$ . (b) Dependence on the radial trap stiffness  $k_r$  as a function of declining gauge pressure  $p_g$  in the microfluidic air channel. Error bars represent the error of the Gaussian fits. The solid line is the exponential fit to the data. Inset:  $(x-y)$  position scatterplot for different gauge pressures highlighted by different colors corresponding to the colors of the histograms in (a).

To demonstrate the capability of dynamic catching and releasing particles, we connected the pneumatic microchannel to a syringe and pump-system. Then, 200 ms short positive or negative flow peaks with a rate of  $100 \mu\text{l/s}$  were applied to increase or decrease the volume as seen in Fig. 6.4(b). Between  $t = 0$  s and  $t = 3$  s a particle was stably trapped in the left pocket with an obtained radial trap stiffness of  $k_r = 0.74$  fN/nm, which can be seen by the low fluctuations of the  $y$ -trajectories and in the top iSCAT image and sketch in Fig. 6.4(a) and (c). A first  $-100 \mu\text{l/s}$  drag of the syringe at  $t = 3.2$  s for 200 ms, induced a flow in the nanofluidic channel, which pressed the particle to the left border of the trap, clearly visible by the lower and left shifted center of the particle fluctuations in the  $y$ -trajectories. However, the particle was strongly trapped to withstand the induced flow. Since the drag of the syringe reduced the volume and pressure of the microchannel and thus increased the height of the nanofluidic channel, the trap stiffness was reduced to  $k_r = 0.71$  fN/nm, and further after each following drag. After the fourth pressure reduction, the particle was released from the trap as shown in the middle iSCAT micrograph at  $t = 8$  s. The particle was undergoing random walk with partially confinement in the middle pocket. In the time intervals where the particle was weakly trapped in the middle pocket, a radial trap stiffness of only  $k_r = 0.21$  fN/nm was measured. At  $t = 13.4$  s, a first pressure

---

increase of  $100 \mu\text{l/s}$  for  $200 \text{ ms}$  was applied, inducing a flow in the nanofluidic channel to the right, visible as big jumps in the  $y$ -trajectories. After a third increase, the particle was caught again, now in the right pocket and could be stably trapped with a radial trap stiffness of  $k_r = 0.75 \text{ fN/nm}$ .

In summary, we introduced the fabrication of multilayer PDMS devices with an integrated pneumatic control system for non-contact electrostatic trapping and manipulation of nano-objects in aqueous environments. A rapid and simple replica molding production process and the absence of any externally applied power source, makes the devices affordable and usable for research and commercial applications. In order to demonstrate the performance of the device, we showed that the trapping stiffness could be reliably tuned over more than two orders of magnitude and kept at a desired strength over time. Furthermore dynamic catching and releasing of the particles was shown to demonstrate fast and controllable manipulation of the objects. This feature enables the possibility for fast analysis of multiple samples by releasing the trapped objects after measurements and flushing the nanofluidic channels with new sample solutions.

This work was funded by the Swiss Nanoscience Institute in Basel, Switzerland (SNI PhD Graduate School, Project P1202).

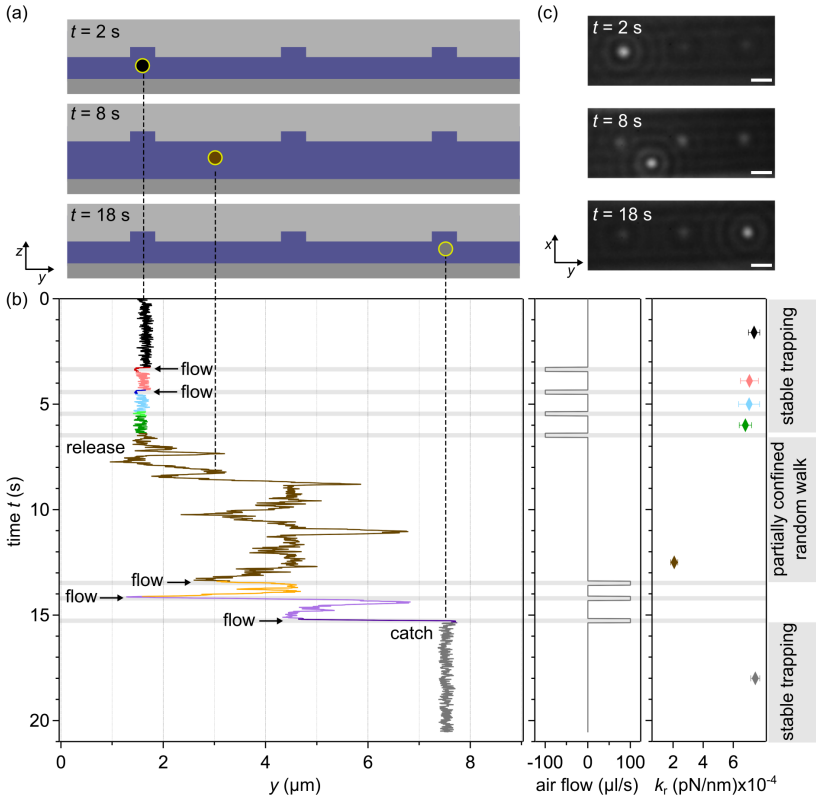


**Figure 6.4.:** Catch and release of nanoparticles: (a) Schematic of the nanofluidic channel height and particle position at different time  $t$ . (b) Time course of the catch and release sequence: left graph,  $y$ -trajectories of a single 100 nm particle; middle graph, volume change in the pneumatic microchannel; right graph, radial trap stiffness between volume changes when the particle is trapped in a pocket. (c) A series of iSCAT images at different times  $t$  corresponding to the sketch in (a). In the iSCAT images, the three pockets and the 100 nm particle are clearly visible. Scale bars: 1  $\mu\text{m}$ .

## Conclusions and Outlook

The detection and analysis of single molecules and particles in solution is of great scientific and commercial interest today. It provides new insights to understand and analyze chemical reactions, physical properties and transport phenomena, and biological reactions and interactions at the molecular level. Such studies could be only achievable by the investigation and development of new imaging and detection systems that allow the observation of the nanoworld. Further, various trapping and manipulation techniques were developed in the last decades which enable long observation times of the objects of interest and allow additional characterizations, such as force measurements. GIE trapping systems provide a great platform for studying individual nano-objects for research and industrial applications due to their chip-based approach and absence of any externally applied fields. The development, characterization and usages of these trapping systems were explored in this thesis. Within this chapter, the main achievements are again highlighted with conclusions and perspectives for future experiments and applications.

### 7.1. Conclusions and further investigations

#### 7.1.1. Higher detection contrast using glass-based GIE trapping devices

In order to explore the accurate motion and behavior of nano-objects in fluids, the detection of the trajectories with high lateral precision is of crucial need. For that reason, iSCAT detection was used in this work, which provides label-free imaging of nano-objects with higher SNR compared to imaging

methods based on pure scattering. Another advantage of iSCAT detection is that the underlying background structures of the devices are not canceled out and can be imaged simultaneously with the observed objects. However, to achieve precise tracking of the trapped objects, high contrast and SNR of the imaged objects are essential. In silicon-based GIE trapping devices, Au NPs smaller than 60 nm are vanished in the background noise and thus become difficult to detect and characterize. One possibility to address this issue could be the development and improvement of the iSCAT detection method. Investigations on the device technology could also result in higher detection of the Au NPs. In this context, the concept of iSCAT detection for different fluidic systems was elucidated and it was found, that the high reflection of the Si/SiO<sub>2</sub> interface in the silicon-based devices limits the detection of smaller Au NPs. To overcome this limitation, devices made from glass substrates were developed and characterized which led to the imaging of Au NPs with significant higher SNR of one order of magnitude compared to Au NPs imaged in silicon-based devices. These achievements on the glass-based devices allowed the precise tracking of Au NPs down to 40 nm in diameter. The detection and tracking of smaller Au NPs should be possible in general using these devices. However, when imaging smaller Au NP, such as 20 nm in diameter, the limits of the home-built iSCAT detection system were reached. Since the diffusion coefficient  $D$  of a spherical object is proportional to the diameter of the particle as  $D \propto 1/d$ , the particles velocity increases with decreasing diameter. The fast movements of the 20 nm Au NPs prevented a precise tracking, since the particles were vanished in the background noise due to the long exposure times and slow acquisition rates of the home-built iSCAT detection system. For tracking smaller particles using iSCAT detection, faster scanning elements and controllers are essential. This can be achieved by replacing the scanning mirrors with AODs and a faster LabView controller or function generators [17]. A second possibility could be the trapping of smaller particles in solutions with higher viscosity  $\eta$ , which would result in lower diffusion coefficients of the particles ( $D \propto 1/\eta$ ).

### 7.1.2. Integrating GIE trapping into a microfluidic system – fast screening of trapped objects

Another key advantage of GIE trapping compared to other trapping methods such as the ABEL trap is, that it allows the studying of a vast number of individually trapped objects simultaneously by creating trap lattices as shown in Fig. 7.3. In a few minutes of data collection one can image enough objects to obtain distributions of their properties and behavior. To advance this technology even more, the GIE trapping method was integrated into a microfluidic system that allows the precise forming of a gradient over the trapped objects of e.g. salt, pH, or other reactants. Since many nanofluidic



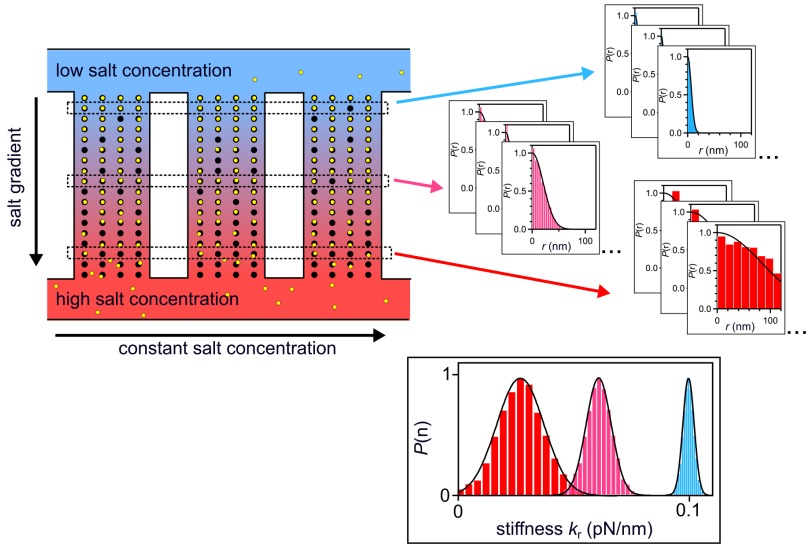


**Figure 7.1.:** Illustration, showing the potential of parallel trapping and imaging of individual nano-objects along a salt gradient.

channels can be fabricated in parallel, only a few minutes of data collection and a single experiment is sufficient to receive enough data to make distributions of the trapped objects at the same conditions and at various conditions along a gradient simultaneously (see Fig. 7.1). Furthermore, reduced sample volumes and precise control over the sample and buffer solutions are further benefits entailed to the GIE trapping method integrated into a microfluidic system. To demonstrate the functionality and potential of these devices, the trapping of 60 nm Au NPs along a NaCl salt gradient was performed and the motion of the particles were analyzed. Particles trapped in higher salt concentrations experienced a weaker trapping and shorter residence times due to the shortened Debye length of the device and particles surface potential.

### 7.1.3. Exploring the geometrical limits of glass-based devices and further biological investigations

Beside the development of devices for better detection and new designs, the geometrical fabrication limits for trapping smaller particles, biomolecules or particles at higher salt concentrations were explored. As described, reducing

the nanofluidic channel height  $h_c$  increases the potential depth and thus allows longer and stronger trapping. Glass-based nanofluidic channels with a height down to  $h_c = 75$  nm and a width of  $10\ \mu\text{m}$  could be produced without roof collapse. By fabricating channel heights of only  $h_c = 50$  nm, partially roof collapse was observed in the  $10\ \mu\text{m}$  wide nanofluidic channels. However, channels with a smaller width or integrating supporting pillars, as for the PDMS devices, could allow the fabrication of even thinner nanofluidic channels. Using these devices, trapping of smaller Au NPs down to 40 nm could be achieved in glass-based devices with dimensions of  $h_c = 95$  nm,  $w_p = 200$  nm and  $h_p = 50$  nm as shown in Fig. 7.2A at a salt concentration of  $\sim 3$  mM. The trapping of smaller Au NPs could be not explored due to the detection limits with the iSCAT setup as explained above.

A major objective in the development of contact-free trapping methods is to advance the technologies for trapping single biomolecules. This would allow the investigation of conformational changes, molecule-molecule interactions or to determine individual properties such as their net charge, size or length. Since electrostatic trapping depends mainly on the charge carried by the object and various biomolecules such as proteins, other macromolecules or DNA are usually charged when exposed to water at neutral pH, trapping of biological entities could be possible. Specifically DNA, carrying a charge of  $-2 e$  per base pair (every 0.34 nm), is a good candidate to be trapped with electrostatic systems, since it can be preserved and diluted in aqueous solutions of low ionic strength. To demonstrate, glass-based GIE trapping devices with a nanofluidic channel height of  $h_c = 75$  nm, a pocket depth of  $h_p = 40$  nm and a width of  $w_p = 500$  nm were fabricated to trap DNA. A fluorescence image sequence of trapped  $\lambda$ -DNA diluted in a buffer solution of 0.1 mM NaCl is shown in Fig. 7.2B. Here several trapping behaviors were observed, such as DNA strands that were completely trapped as a coiled structure by the pockets as seen by the single bright spots (yellow circle in Fig. 7.2B) or DNA strands fluctuating between two pockets with both ends hold by one pockets (white arrow). Additionally, DNA strands were observed with only one end trapped in a pocket (red arrow). These stretch-coil observations could lead to new information on mechanical properties of the DNA, important to understand the packaging of stretched DNA into chromosomes.

### 7.1.4. High-throughput, low-cost and simplified fabrication using PDMS-based devices

As described, the chip-based approach and the fact that no additional external power is needed to use the devices, experiments with little effort can be performed. However, time consuming and high-end nanofabrication processes lead to high-costs of the fabrication of glass- and silicon-based devices and

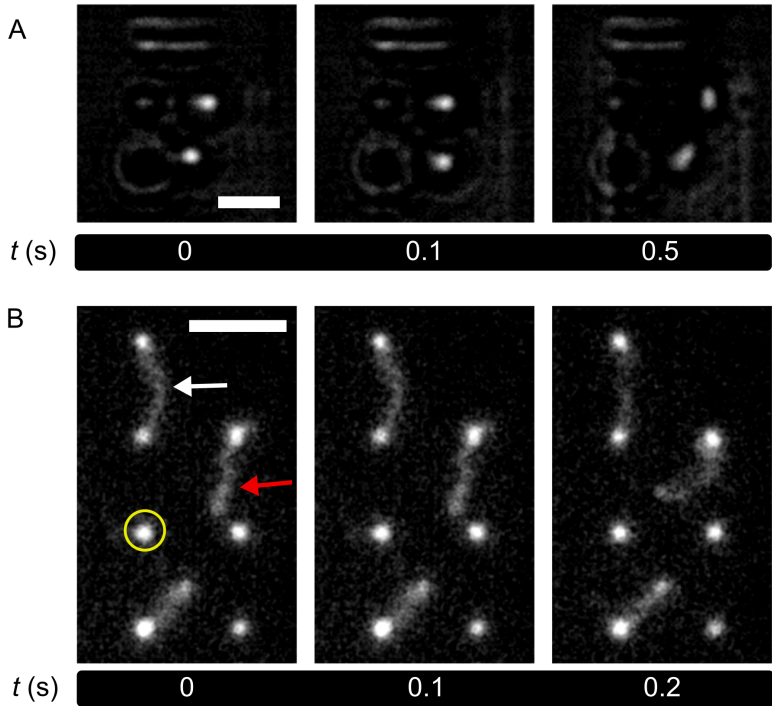


**Figure 7.2.:** A) iSCAT image sequence of 40 nm Au NPs trapped in glass GIE trapping devices. Imaged were processed by background subtraction and contrast adjustment, Scale bar:  $2 \mu\text{m}$ . B) Fluorescence microscopy image sequence of  $\lambda$ -DNA strands trapped by  $w_p = 500$  nm pockets. The DNA was either trapped completely as a coiled structure (yellow circle), partially (red arrow) or between two pockets (white arrow). Scale bar:  $4 \mu\text{m}$ .

thus makes the development for research and use for commercial applications difficult. GIE trapping devices made from soft-lithography replica molding processes were introduced in this work that overcome this major drawback. These devices made from flexible PDMS material can be fabricated by a high-throughput, low-cost, and simplified replica molding process. To demonstrate the functionality of the devices, a quantitative characterization of the trapping strength, residence time, and potential depth of Au NPs down to 60 nm in diameter was realized in different device geometries. For 100 nm Au NPs potential depths of up to  $Q \cong 24 k_B T$  were observed, corresponding to stable trapping times of many days. Furthermore, due to the elasticity of the PDMS material, the devices were mechanically compressed which resulted in the reduction of the nanofluidic channel height  $h_c$  and thus stronger and longer trapping. Using this capability, the nanofluidic channel height was reduced to only  $h_c \sim 40$  nm resulting in potential depths of up to  $Q \sim 200 k_B T$ , which provide strong and stable contact-free trapping of the particles beyond experimental demands.

As explained, a major objective would be the trapping of individual biomolecules. While polymer dynamics of DNA strands can be explored in low ionic strength solutions, the investigating of proteins in a natural environment remains challenging. Preserving their functionality would imply the trapping at physiological buffer conditions with an ionic strength in the range of 30 – 200 mM NaCl or KCl. As described in Chapter 4 and by Eq. 2.8 and 2.10 the electrostatic potential of a charged wall in solution follows an exponential decay with a characteristic length scale  $\kappa^{-1}$  proportional to  $1/\sqrt{c_0}$ . As a result, at a monovalent concentration of  $c_0 = 30$  mM,  $\kappa^{-1}$  is in the order of 2 nm, which would make electrostatic trapping difficult. In trapping devices, such as PDMS-based, where the nanofluidic channel height can be reduced comparable to the size of the molecules, entropic trapping could be possible due to the high salt concentration [117–119]. Even more, reducing the nanofluidic channel height below the actual size of the objects gives the possibility to sterically trap the object in the pocket while still having the option to change the buffer condition by diffusion. For demonstration, we introduced 100 nm Au NPs into a PDMS device and reduced the nanofluidic channel height by a compression pressure to trap the particles strongly. Then the buffer was exchanged with a 1:9 phosphate buffer saline (PBS) solution diluted in DI water, which results in a concentration of  $c_0 = 13.8$  mM NaCl and 0.27 mM KCl. During the exchange and at this high salt concentration, the particles could be stably trapped over time as shown in Fig. 7.3. This experiment demonstrate the potential of the PDMS-based trapping devices for confining nano-objects at high salt concentrations. The trapping at even higher salt concentration, such as physiological buffer conditions to trap biomolecules, should be possible and could be investigated in future experiments.

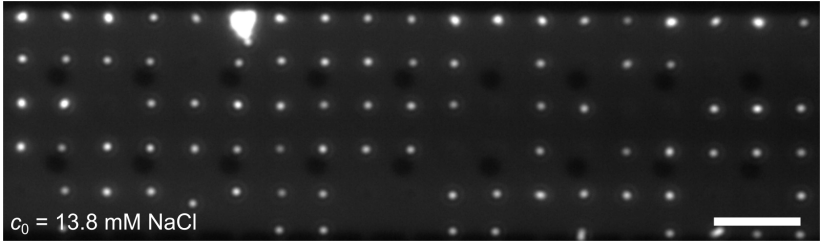


**Figure 7.3.:** A) Large scale trapping of 100 nm Au NPs in PDMS-based GIE trapping devices at high ionic buffer concentration of  $c_0 = 13.8$  mM NaCl. Scale bar: 4  $\mu\text{m}$ .

With the PDMS GIE trapping device a platform for studying the behavior and properties of individual trapped nano-objects with little effort is provided. Due to the deep trap potentials and low nanofluidic channel heights achieved, it is the prime chip-based candidate for trapping individual biomolecules at physiological conditions based on electrostatic fields. Additionally, simplified and low-cost fabrication processes make the device equally available for research experiments and developments, and commercial use. However, further investigations are needed to achieve the trapping of smaller nano-objects at higher salt concentrations.

From the fabrication point of view, one time and cost intensive step remained, which is the fabrication of the silicon master. This is especially caused by the nanofabrication steps, which include several rounds of metal layer deposition, e-beam exposure and etching steps as described in the nanofabrication protocols in Appendix B. To approach this drawback, the master could be fabricated by thermal scanning probe lithography (SwissLitho AG, NanoFrazer), where a cantilever with a heatable tip directly writes 3D structures into a spin-coated resist. This prime master could then be subsequently used to fabricate OrmoStamp<sup>®</sup> masters for PDMS device fabrication. With this method, the different heights of the microfluidic supply channels, nanofluidic trapping channels and the nanotraps could be made with only one lithographic step of nanofabrication. Additionally different nanofluidic channel heights and pocket depths could be implemented into one device.

The development of GIE trapping devices made by soft lithography replica molding demonstrates the possibility that the GIE trapping method can be extended to new materials and fabrication processes. As an example, X-ray free-electron laser (XFEL) studies provide structural elucidation on biological materials using nanocrystals or single molecules. To obtain struc-

tural resolution, thousands of diffraction patterns of single exposure shots are recorded, with each shot destroying the sample. Thus devices and platforms are developed to rapidly deliver the sample into the laser spot. Liquid jet devices [196, 197] or silicon nitride windows [198] are the main achievements. But, sample consumption is the bottleneck in liquid jet devices for experiments with precious samples, since the laser pulses are not synchronized with sample delivery in the jet leading to large sample lost. Silicon nitride windows could overcome this drawback, since the sample can be specifically shot at a known position. However, silicon nitride windows are made by high-end fabricating processes making them expensive to produce. As an alternative, GIE trapping devices made from polystyrene foils and UV-curable adhesives could be fabricated with a fast and low-cost replica molding process and used for XFEL studies [186, 187].

### 7.1.5. Direct manipulation of trapped nanoparticles

Optical tweezers are among the most used methods for trapping individual objects. Perhaps one reason of their broad popularity is the feasibility to directly manipulate the trapped object such as increasing the trapping strength or releasing and catching the object during the experiment. In order to extend the chip-based GIE trapping technology for manipulation of trapped objects, multilayer PDMS devices with an integrated pneumatic control system were introduced. The manipulation of the trapping strength on a 100 nm Au NP was demonstrated over two orders of magnitude by changing the pressure in the pneumatic chamber, obtaining a maximum radial stiffness of  $k_r = 0.13$  pN/nm. Again, such high trapping strengths related to deep potentials, could make the trapping of biological entities possible. Furthermore dynamic catching and releasing of the particles was shown to demonstrate fast and controllable manipulation of the objects, which enables the possibility for fast analysis of multiple samples by releasing the trapped objects after measurements and flushing the nanofluidic channels with new sample solutions. To maintain the simplicity of the system, this experiment was performed with a simple, conventional syringe and a syringe pump that should be available in every fluidic lab and thus allows to perform single particle experiments with low expenditure. For example, this fast and direct manipulation could be used to trap DNA along slits and observe the stretch-coil dynamics of the polymer chains when changing the pressure. From the fabrication point of view, the devices could be extended by multiple, individual controllable pneumatic microchannels [181]. This would bring the advantage to create multiple heights or height gradients within a nanofluidic channel and thus different trapping strengths and behavior along a channel. Applying a flow in devices with such a nanofluidic height gradient could lead to applications in particle sorting by size or net charge.

## 7.2. Further applications and considerations

### 7.2.1. Large-scale patterning for nanolithography

An array of 100 nm Au NPs trapped in a  $36 \times 10 \mu\text{m}^2$  lattice can be seen in Fig. 7.3. The particules are trapped in  $w_p$  500 nm pockets and separated by a distance of  $2 \mu\text{m}$ . The sizes of the trapped particles and the separation distance can be varied based on the experimental needs. Such systems could find applications in particle lithography if the particles could be placed and fixed to the surface [199, 200]. This behavior was observed when high salt concentrations in the devices were used. After strong trapping of 100 nm Au NPs in the PDMS devices (with an applied mechanical pressure) and increasing of the salt concentration in the buffer solution to about  $c_0 = 140 \text{ mM}$  NaCl, the particles got immediately and irreversibly stuck to the surface in the trap. Non-covalently bound PDMS devices could be used in this case. The adherent properties of PDMS and the additional mechanical force applied should still lead to a stable trapping. After increasing the salt concentration, the PDMS could be removed leaving the precise located Au NPs on the surface, uniformly arranged to a lattice or other pattern design as illustrated in Fig. 7.4A. The particles could be then directly used to attach other molecules, used for plasmonic studies, or as nanolithographic pattern mask as shown in Fig. 7.4B-C. Various lithography methods could be used to built fast and low-cost devices. The particles and the surface could be patterned with a metal layer followed by a lift-off process which would result in nanometer-sized apertures as seen in Fig. 7.4C. In such apertures, called zero-mode waveguides, observations of single molecules at high molecule concentrations are possible since only a zeptoliter ( $10^{-21} \text{ l}$ ) volume is exposed [132, 201]. Further these devices are used for real-time single molecule DNA sequencing [202] for fast DNA barcode analysis [203]. Instead of using the apertures for detection, holes could be etched into the underlying material to fabricate nanopores in SiN-membranes (see Fig. 7.4)D. Such nanopore membranes can be used to make artificial nuclear pore complexes and study the transport selectivity [204, 205].

### 7.2.2. Exploring single biomolecules

In this thesis, mainly Au NPs were used in experiments to characterize the performance of the developed devices and to compare it with other trapping methods. Stable confinement of these particles was achieved at even higher salt concentrations. Since the label-free trapping of biomolecules at physiological buffer conditions remains a major challenge, not only for electrostatic field-based methods, biomolecules could be attached to Au NPs to investigate their properties. In such an approach, DNA molecules could be labeled with two

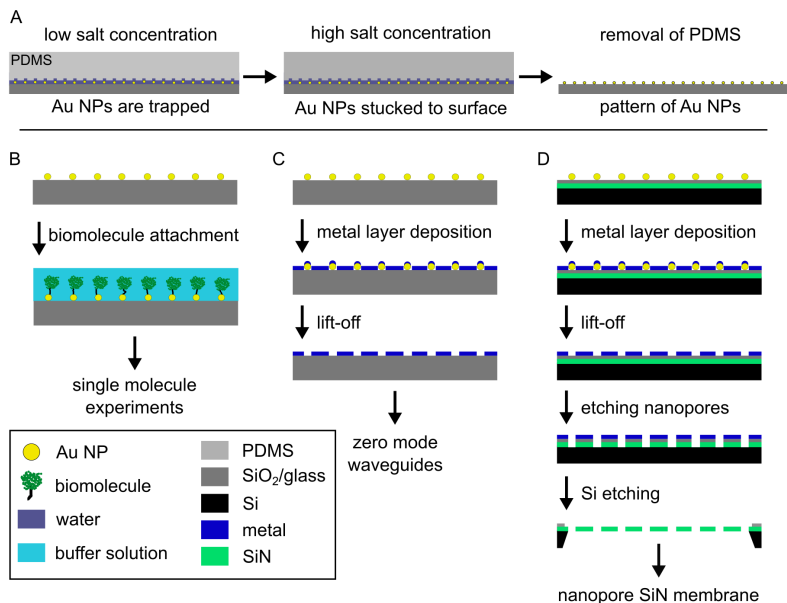


**Figure 7.4.:** A) Large-scale patterning of nanoparticles using GIE trapping devices, B) Application for single molecule experiments, C) Application for nanolithography using lift-off process, D) Application for nanolithography using lift-off process and etching

Au NPs at each end. Fabricating circular traps separated by the length of the DNA could lead to the trapping of the particles in two different pockets as illustrated in Fig. 7.5A. This would allow for studying the dynamics of DNA in solution. Applying a compression pressure to the PDMS device, either mechanically or by the pneumatic control system, would shift the motion of the particles to the center of the pockets and thereby induce a force on the DNA. This stretching force could be measured by analyzing the motion of the two particles. Reducing the nanofluidic channel height below the actual particle diameter would additionally confine the particles sterically. The salt concentration could be then increased with the integrated microfluidic system and molecules acting on DNA could be flushed in by pressure driven or electroosmotic flow. In Fig. 7.5B-C, three such proposed experiments are illustrated. Inserting DNA polymerase and deoxyribonucleotides would allow the direct observation of DNA replication (Fig. 7.5B). Simultaneously the force acting on the DNA by unzipping the double helix could be measured by tracking the motion of the Au NPs in the traps [190]. Similar experiments could be performed with single stranded DNA for real time sequencing



applications [202] or RNA polymerase and oxyribonucleotides to study the transcription from DNA into mRNA. A second suggestion could be the insertion of specific restriction enzymes that could allow the observation of DNA cleavage (Fig. 7.5C). From such an experiment, the cutting position, the lengths of the restriction pattern and the reaction kinetics of the enzymes could be studied [206]. Exploring the initial steps of DNA packaging could be another experiment to perform with the Au NP – DNA – Au NP approach. In the initial packaging step, the DNA is wrapped around proteins called histones as illustrated in Fig. 7.5D. This process shortens the end to end distance and could be probed by the particles motion. Further, applying a compression to the device could stretch and thus unwrap the DNA. From such experiments, not only the DNA-protein complex could be observed, but also the strength, dynamics, and energetics of the DNA-protein interactions [190].

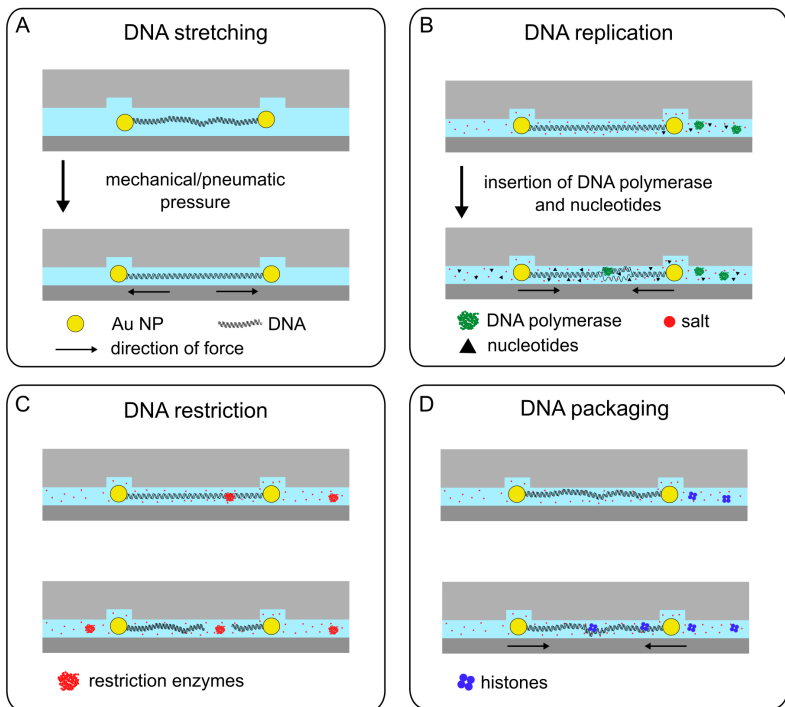


**Figure 7.5.:** Illustration for studying biomolecules bound to Au NPs using GIE trapping devices.

### 7.2.3. GIE trapping devices as sensors and diagnostic tools

Continuing with the approach of trapping Au NPs, the GIE trapping technology could be used as sensors or diagnostic tools. One possibility could be the sensing of charged analytes binding to specific antibody-labeled Au NPs trapped in circular pockets. Since the GIE trapping method is highly sensitive to changes of surface charge of the trapped object, single binding events of charged analytes should be detectable. Additionally, stable trapping over minutes and hours allows the monitoring and thus calibration of hundreds individually trapped particles before the analyte insertion. Every single trapped particle could then serve as a highly sensitive sensor element. In such an approach, both, binding positively and negatively charged analytes could be studied. Binding of a positively charged analyte would trap the particle stronger, whereas a negatively charged analyte would lead to weaker trapping. Suchlike sensors could be used in medical diagnostic or environmental applications as e.g. water quality analysis.

### 7.2.4. Direct observation of diffusive behavior

One key advantage of chip-based electrostatic devices is the implementation of different trap geometries. Beside circular pockets, rectangular slits, long grooves or grids can be fabricated as potential wells. As introduced in Chapter 2, the MSD of a freely diffusing particle in 1D, 2D and 3D is proportional to the lag time  $\Delta t$  as sketched in Fig. 7.6A. If a particle is restricted in diffusion, such as in a circular trap, the MSD reaches a plateau, correlated to the trap stiffness. However, if the dimension is reduced to a 1D system containing many particles, mutual passage of the particles is excluded and thus the sequence of the particles remains unchanged. This is called single file diffusion (SFD) and is often observed in biological systems such as ion transport through membrane channels [207–211]. In SFD, the motion of the particles is suppressed due to collisions with neighboring particles, which results in a sub-diffusive behavior and a  $\text{MSD}_{x,\text{SFD}}$  proportional to  $\sqrt{\Delta t}$  (see Fig. 7.6B). Using GIE trapping devices with long rectangular grooves, direct observation of such effect could be possible. Moreover, since grooves with several widths can be easily fabricated by e-beam lithography, an investigation of the crossover from single file to Fickian diffusion could be experimentally performed on the nanometer scale [210, 211]. Further, by fabricating grids with different widths (see Fig. 7.6C), the diffusive behavior of a semi 2D system (2D lattice) could be investigated. Here the passing of particles could be still possible in the junctions of the grid but not in the short channels. This would rise the question, if the  $\text{MSD}_{2\text{D lattice}} = B \Delta t^a$  would be affected by the time exponent  $a$  or only by the diffusion constant  $B$ ?

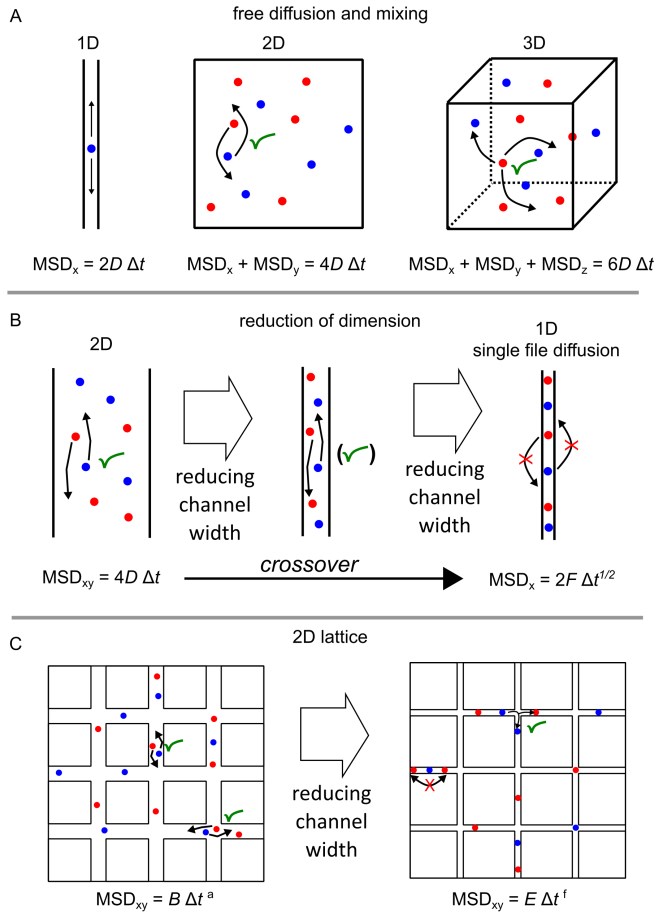


**Figure 7.6.:** Sketch of diffusion behavior in different systems. A) Free diffusion and passing of particles B) reduction of dimension and single file diffusion C) 2D lattice walk



## Bibliography

- [1] D. A. Schafer, J. Gelles, M. P. Sheetz, and R. Landick. “Transcription by single molecules of RNA polymerase observed by light microscopy”. *Nature* 352 (1991), pp. 444–448.  
DOI: [10.1038/352444a0](https://doi.org/10.1038/352444a0).
- [2] H. P. Lu, L. Xun, and X. S. Xie. “Single-Molecule Enzymatic Dynamics”. *Science* 282 (1998), pp. 1877–1882.  
DOI: [10.1126/science.282.5395.1877](https://doi.org/10.1126/science.282.5395.1877).
- [3] Y. Jiang, N. R. Douglas, N. R. Conley, E. J. Miller, J. Frydman, and W. E. Moerner. “Sensing cooperativity in ATP hydrolysis for single multisubunit enzymes in solution.” *Proceedings of the National Academy of Sciences of the United States of America* 108 (2011), pp. 16962–16967.  
DOI: [10.1073/pnas.1112244108](https://doi.org/10.1073/pnas.1112244108).
- [4] E. A. Lipman, B. Schuler, O. Bakajin, and W. A. Eaton. “Single-molecule measurement of protein folding kinetics.” *Science* 301 (2003), pp. 1233–1235.  
DOI: [10.1126/science.1085399](https://doi.org/10.1126/science.1085399).
- [5] G. Luo, M. Wang, W. H. Konigsberg, and X. S. Xie. “Single-molecule and ensemble fluorescence assays for a functionally important conformational change in T7 DNA polymerase”. *Proceedings of the National Academy of Sciences* 104 (2007), pp. 12610–12615.  
DOI: [10.1073/pnas.0700920104](https://doi.org/10.1073/pnas.0700920104).
- [6] Y. Sakiyama, A. Mazur, L. E. Kapinos, and R. Y. H. Lim. “Spatiotemporal dynamics of the nuclear pore complex transport barrier resolved by high-speed atomic force microscopy”. *Nature Nanotechnology* 11 (2016), pp. 1–6.  
DOI: [10.1038/nnano.2016.62](https://doi.org/10.1038/nnano.2016.62).

- [7] N. Mojarad and M. Krishnan. “Measuring the size and charge of single nanoscale objects in solution using an electrostatic fluidic trap.” *Nature Nanotechnology* 7 (2012), pp. 448–452.  
DOI: [10.1038/nnano.2012.99](https://doi.org/10.1038/nnano.2012.99).
- [8] A. N. Kapanidis and T. Strick. “Biology, one molecule at a time”. *Trends in Biochemical Sciences* 34 (2009), pp. 234–243.  
DOI: [10.1016/j.tibs.2009.01.008](https://doi.org/10.1016/j.tibs.2009.01.008).
- [9] I. Tinoco Jr. and R. L. Gonzalez Jr. “Biological mechanisms , one molecule at a time”. *Genes and Development* 25 (2011), pp. 1205–1231.  
DOI: [10.1101/gad.2050011](https://doi.org/10.1101/gad.2050011).
- [10] F. Ritort. “Single-molecule experiments in biological physics: methods and applications.” *Journal of Physics: Condensed Matter* 18 (2006), R531–R583.  
DOI: [10.1088/0953-8984/18/32/R01](https://doi.org/10.1088/0953-8984/18/32/R01).
- [11] P. Hinterdorfer and A. van Oijen. *Handbook of Single-Molecule Biophysics*. Springer Science & Business Media, 2009, p. 672.
- [12] A. A. Deniz, S. Mukhopadhyay, and E. A. Lemke. “Single-molecule biophysics: at the interface of biology, physics and chemistry.” *Journal of the Royal Society, Interface* 5 (2008), pp. 15–45.  
DOI: [10.1098/rsif.2007.1021](https://doi.org/10.1098/rsif.2007.1021).
- [13] T. Cordes and S. A. Blum. “Opportunities and challenges in single-molecule and single-particle fluorescence microscopy for mechanistic studies of chemical reactions”. *Nature Chemistry* 5 (2013), pp. 993–999.  
DOI: [10.1038/nchem.1800](https://doi.org/10.1038/nchem.1800).
- [14] K. Yserentant and D. P. Herten. “Single-Molecule Light Microscopy”. *eLS. John Wiley & Sons* (2016), pp. 1–9.  
DOI: [10.1002/9780470015902.a0002997.pub3](https://doi.org/10.1002/9780470015902.a0002997.pub3).
- [15] J. Ortega-Arroyo and P. Kukura. “Interferometric scattering microscopy (iSCAT): new frontiers in ultrafast and ultrasensitive optical microscopy.” *Physical Chemistry Chemical Physics* 14 (2012), pp. 15625–15636.  
DOI: [10.1039/c2cp41013c](https://doi.org/10.1039/c2cp41013c).
- [16] H. Taguchi, T. Ueno, H. Tadakuma, M. Yoshida, and T. Funatsu. “Single-molecule observation of protein-protein interactions in the chaperonin system”. *Nature Biotechnology* 19 (2001), pp. 861–865.
- [17] M. Krishnan, N. Mojarad, P. Kukura, and V. Sandoghdar. “Geometry-induced electrostatic trapping of nanometric objects in a fluid.” *Nature* 467 (2010), pp. 692–695.  
DOI: [10.1038/nature09404](https://doi.org/10.1038/nature09404).

- [18] K. Lindfors, T. Kalkbrenner, P. Stoller, and V. Sandoghdar. “Detection and Spectroscopy of Gold Nanoparticles Using Supercontinuum White Light Confocal Microscopy”. *Physical Review Letters* 93 (2004), pp. 1–4.  
DOI: [10.1103/PhysRevLett.93.037401](https://doi.org/10.1103/PhysRevLett.93.037401).
- [19] V. Jacobsen, P. Stoller, C. Brunner, V. Vogel, and V. Sandoghdar. “Interferometric optical detection and tracking of very small gold nanoparticles at a water-glass interface.” *Optics Express* 14 (2006), pp. 405–414.
- [20] P. Kukura, H. Ewers, C. Müller, A. Renn, A. Helenius, and V. Sandoghdar. “High-speed nanoscopic tracking of the position and orientation of a single virus.” *Nature Methods* 6 (2009), pp. 923–927.  
DOI: [10.1038/nmeth.1395](https://doi.org/10.1038/nmeth.1395).
- [21] H. Frauenfelder, P. G. Wolynes, and R. H. Austin. “Biological physics”. *Reviews of Modern Physics* 71 (1999), S419–S430.  
DOI: [10.1038/467033a](https://doi.org/10.1038/467033a).
- [22] M. Rief, M. Gautel, F. Oesterhelt, J. M. Fernandez, and H. E. Gaub. “Reversible Unfolding of Individual Titin Immunoglobulin Domains by AFM”. *Science* 276 (1997), pp. 1109–1112.  
DOI: [10.1126/science.276.5315.1109](https://doi.org/10.1126/science.276.5315.1109).
- [23] M. S. Kellermayer, S. B. Smith, H. L. Granzier, and C. Bustamante. “Folding-unfolding transitions in single titin molecules characterized with laser tweezers”. *Science* 276 (1997), pp. 1112–1116.  
DOI: [10.1126/science.276.5315.1112](https://doi.org/10.1126/science.276.5315.1112).
- [24] L. Tskhovrebova, J. Trinick, J. A. Sleep, and R. M. Simmons. “Elasticity and unfolding of single molecules of the giant muscle protein titin”. *Nature* 387 (1997), pp. 308–312.  
DOI: [10.1038/nature02555.1..](https://doi.org/10.1038/nature02555.1..)
- [25] J. Clarke, P. M. Williams, and A. Borgia. “Single-Molecule Studies of Protein Folding”. *Annual Review of Biochemistry* 77 (2008), pp. 101–125.  
DOI: [doi:10.1146/annurev.biochem.77.060706.093102](https://doi.org/10.1146/annurev.biochem.77.060706.093102).
- [26] K. Svoboda, C. F. Schmidt, B. J. Schnapp, and S. M. Block. “Direct Observation of Kinesin Stepping by Optical Trapping Interferometry”. *Nature* 365 (1993), pp. 721–727.  
DOI: [10.1038/365721a0](https://doi.org/10.1038/365721a0).
- [27] M. J. Lang, C. L. Asbury, J. W. Shaevitz, and S. M. Block. “An Automated Two-Dimensional Optical Force Clamp for Single Molecule Studies”. *Biophysical Journal* 83 (2002), pp. 491–501.

- [28] A. Yildiz, M. Tomishige, R. D. Vale, and P. R. Selvin. “Kinesin walks hand-over-hand.” *Science* 303 (2004), pp. 676–678.  
DOI: [10.1126/science.1093753](https://doi.org/10.1126/science.1093753).
- [29] J. Andrecka, J. Ortega Arroyo, K. Lewis, R. A. Cross, and P. Kukura. “Label-free Imaging of Microtubules with Sub-nm Precision Using Interferometric Scattering Microscopy”. *Biophysical Journal* 110 (2016), pp. 214–217.  
DOI: [10.1016/j.bpj.2015.10.055](https://doi.org/10.1016/j.bpj.2015.10.055).
- [30] K. C. Neuman, E. A. Abbondanzieri, R. Landick, J. Gelles, and S. M. Block. “Ubiquitous Transcriptional Pausing Is Independent of RNA Polymerase Backtracking”. *Cell* 115 (2003), pp. 437–447.  
DOI: [10.1016/S0092-8674\(03\)00845-6](https://doi.org/10.1016/S0092-8674(03)00845-6).
- [31] E. A. Abbondanzieri, W. J. Greenleaf, J. W. Shaevitz, R. Landick, and S. M. Block. “Direct observation of base-pair stepping by RNA polymerase.” *Nature* 438 (2005), pp. 460–465.  
DOI: [10.1038/nature04268](https://doi.org/10.1038/nature04268).
- [32] L. Edman, U. Mets, and R. Rigler. “Conformational transitions monitored for single molecules in solution.” *Proceedings of the National Academy of Sciences of the United States of America* 93 (1996), pp. 6710–6715.
- [33] M. Margittai, J. Widengren, E. Schweinberger, G. F. Schroder, S. Felekyan, E. Haustein, M. Konig, D. Fasshauer, H. Grubmuller, R. Jahn, and C. A. Seidel. “Single-molecule fluorescence resonance energy transfer reveals a dynamic equilibrium between closed and open conformations of syntaxin 1”. *Proceedings of the National Academy of Sciences of the United States of America* 100 (2003), pp. 15516–15521.  
DOI: [10.1073/pnas.2331232100](https://doi.org/10.1073/pnas.2331232100).
- [34] F. Ruggeri, F. Zosel, N. Mutter, M. Rózycka, M. Wojtas, A. Ozyhar, B. Schuler, and M. Krishnan. “Single-molecule electrometry”. *Nature Nanotechnology* 12 (2017), pp. 488–495.  
DOI: [10.1038/nnano.2017.26](https://doi.org/10.1038/nnano.2017.26).
- [35] R. I. Litvinov, H. Shuman, J. S. Bennett, and J. W. Weisel. “Binding strength and activation state of single fibrinogen-integrin pairs on living cells.” *Proceedings of the National Academy of Sciences of the United States of America* 99 (2002), pp. 7426–7431.  
DOI: [10.1073/pnas.112194999](https://doi.org/10.1073/pnas.112194999).
- [36] J. R. Wayment and J. M. Harris. “Biotin - Avidin Binding Kinetics Measured by Single-Molecule Imaging”. *Analytical chemistry* 81 (2009), pp. 336–342.  
DOI: [10.1021/ac801818t](https://doi.org/10.1021/ac801818t).



- [37] M. H. van Es, J. Tang, J. Preiner, P. Hinterdorfer, and T. H. Oosterkamp. “Single molecule binding dynamics measured with atomic force microscopy”. *Ultramicroscopy* 140 (2014), pp. 32–36.  
DOI: [10.1016/j.ultramic.2014.02.005](https://doi.org/10.1016/j.ultramic.2014.02.005).
- [38] S. Faez, Y. Lahini, S. Weidlich, R. F. Garmann, K. Wondraczek, M. Zeisberger, M. A. Schmidt, M. Orrit, and V. N. Manoharan. “Fast, Label-Free Tracking of Single Viruses and Weakly Scattering Nanoparticles in a Nanofluidic Optical Fiber”. *ACS Nano* 9 (2015), pp. 12349–12357.  
DOI: [10.1021/acs.nano.5b05646](https://doi.org/10.1021/acs.nano.5b05646).
- [39] A. M. Goldfain, R. F. Garmann, Y. Jin, Y. Lahini, and V. N. Manoharan. “Dynamic Measurements of the Position, Orientation, and DNA Content of Individual Unlabeled Bacteriophages”. *Journal of Physical Chemistry B* 120 (2016), pp. 6130–6138.  
DOI: [10.1021/acs.jpcc.6b02153](https://doi.org/10.1021/acs.jpcc.6b02153).
- [40] J. N. Israelachvili. *Intermolecular and Surface Forces Third Edition*. Academic Press, 2010, p. 710.  
DOI: [10.1016/B978-0-12-375182-9.10025-9](https://doi.org/10.1016/B978-0-12-375182-9.10025-9).
- [41] R. B. Schoch, J. Han, and P. Renaud. “Transport phenomena in nanofluidics”. *Reviews of Modern Physics* 80 (2008), pp. 839–883.  
DOI: [10.1103/RevModPhys.80.839](https://doi.org/10.1103/RevModPhys.80.839).
- [42] A. Einstein. “Über die von der molekularkinetischen Theorie der Wärme geforderte Bewegung von in ruhenden Flüssigkeiten suspendierten Teilchen”. *Annalen der Physik* 322 (1905), pp. 549–560.  
DOI: [10.1002/andp.19053220806](https://doi.org/10.1002/andp.19053220806).
- [43] W. E. Moerner. “A Dozen Years of Single-Molecule Spectroscopy in Physics, Chemistry, and Biophysics”. *The Journal of Physical Chemistry B* 106 (2002), pp. 910–927.  
DOI: [10.1021/jp012992g](https://doi.org/10.1021/jp012992g).
- [44] T. Li, S. Kheifets, D. Medellin, and M. G. Raizen. “Measurement of the instantaneous velocity of a Brownian particle.” *Science* 328 (2010), pp. 1673–1675.  
DOI: [10.1126/science.1189403](https://doi.org/10.1126/science.1189403).
- [45] S. Kheifets, A. Simha, K. Melin, T. Li, and M. G. Raizen. “Observation of Brownian motion in liquids at short times: instantaneous velocity and memory loss.” *Science* 343 (2014), pp. 1493–1496.  
DOI: [10.1126/science.1248091](https://doi.org/10.1126/science.1248091).

- [46] T. Franosch, M. Grimm, M. Belushkin, F. Mor, G. Foffi, L. Forró, and S. Jeney. “Resonances arising from hydrodynamic memory in Brownian motion - The colour of thermal noise”. *Nature* 478 (2011), pp. 8–11.  
DOI: [10.1038/nature10498](https://doi.org/10.1038/nature10498).
- [47] A. Ashkin, J. M. Dziedzic, J. E. Bjorkholm, and S. Chu. “Observation of a single-beam gradient force optical trap for dielectric particles”. *Optics Letters* 11 (1986), pp. 288–290.  
DOI: [10.1364/OL.11.000288](https://doi.org/10.1364/OL.11.000288).
- [48] M. L. Juan, M. Righini, and R. Quidant. “Plasmon nano-optical tweezers”. *Nature Photonics* 5 (2011), pp. 349–356.  
DOI: [10.1038/nphoton.2011.56](https://doi.org/10.1038/nphoton.2011.56).
- [49] A. Ashkin. “History of optical trapping and manipulation of small-neutral particle, atoms, and molecules”. *IEEE Journal of Selected Topics in Quantum Electronics* 6 (2000), pp. 841–856.  
DOI: [10.1109/2944.902132](https://doi.org/10.1109/2944.902132).
- [50] D. G. Grier. “A revolution in optical manipulation.” *Nature* 424 (2003), pp. 810–816.  
DOI: [10.1038/nature01935](https://doi.org/10.1038/nature01935).
- [51] A. Ashkin. “Acceleration and Trapping of Particles by Radiation Pressure”. *Physical Review Letters* 24 (1970), pp. 156–159.  
DOI: [10.1103/PhysRevLett.24.156](https://doi.org/10.1103/PhysRevLett.24.156).
- [52] P. Bartlett and S. Henderson. “Three-dimensional force calibration of a single-beam optical gradient trap”. *Journal of Physics: Condensed Matter* 14 (2002), pp. 7757–7768.  
DOI: [10.1088/0953-8984/14/33/314](https://doi.org/10.1088/0953-8984/14/33/314).
- [53] S. Nedev, A. S. Urban, A. A. Lutich, and J. Feldmann. “Optical force stamping lithography”. *Nano Letters* 11 (2011), pp. 5066–5070.  
DOI: [10.1021/nl203214n](https://doi.org/10.1021/nl203214n).
- [54] M. D. Wang, H. Yin, R. Landick, J. Gelles, and S. M. Block. “Stretching DNA with optical tweezers.” *Biophysical Journal* 72 (1997), pp. 1335–1346.  
DOI: [10.1016/S0006-3495\(97\)78780-0](https://doi.org/10.1016/S0006-3495(97)78780-0).
- [55] Y. Pang, H. Song, and W. Cheng. “Using optical trap to measure the refractive index of a single animal virus in culture fluid with high precision”. *Biomedical Optics Express* 7 (2016), pp. 1672–1689.  
DOI: [10.1364/BOE.7.001672](https://doi.org/10.1364/BOE.7.001672).

- [56] E. Stellamanns, S. Uppaluri, A. Hochstetter, N. Heddergott, M. Engstler, and T. Pfohl. “Optical trapping reveals propulsion forces, power generation and motility efficiency of the unicellular parasites *Trypanosoma brucei*”. en. *Scientific Reports* 4 (2014), pp. 1–7.  
DOI: [10.1038/srep06515](https://doi.org/10.1038/srep06515).
- [57] M. P. MacDonald, G. C. Spalding, and K. Dholakia. “Microfluidic sorting in an optical lattice”. *Nature* 426 (2003), pp. 421–424.  
DOI: [10.1038/nature02120](https://doi.org/10.1038/nature02120).1..
- [58] M. J. Guffey and N. F. Scherer. “All-optical patterning of Au nanoparticles on surfaces using optical traps”. *Nano Letters* 10 (2010), pp. 4302–4308.  
DOI: [10.1021/nl904167t](https://doi.org/10.1021/nl904167t).
- [59] P. J. Pauzauskie, A. Radenovic, E. Trepagnier, H. Shroff, P. Yang, and J. Liphardt. “Optical trapping and integration of semiconductor nanowire assemblies in water”. *Nature Materials* 5 (2006), pp. 97–101.  
DOI: [10.1038/nmat1563](https://doi.org/10.1038/nmat1563).
- [60] A. Hochstetter, E. Stellamanns, S. Deshpande, S. Uppaluri, M. Engstler, and T. Pfohl. “Microfluidics-based single cell analysis reveals drug-dependent motility changes in trypanosomes”. *Lab on a Chip* 15 (2015), pp. 1961–1968.  
DOI: [10.1039/C5LC00124B](https://doi.org/10.1039/C5LC00124B).
- [61] P. M. Hansen, V. K. Bhatia, N. Harrit, and L. Oddershede. “Expanding the optical trapping range of gold nanoparticles”. *Nano Letters* 5 (2005), pp. 1937–1942.  
DOI: [10.1021/nl051289r](https://doi.org/10.1021/nl051289r).
- [62] K. C. Neuman, E. H. Chadd, G. F. Liou, K. Bergman, and S. M. Block. “Characterization of photodamage to *Escherichia coli* in optical traps”. *Biophysical Journal* 77 (1999), pp. 2856–2863.  
DOI: [10.1016/S0006-3495\(99\)77117-1](https://doi.org/10.1016/S0006-3495(99)77117-1).
- [63] Y. Seol, A. E. Carpenter, and T. T. Perkins. “Gold nanoparticles : enhanced optical trapping and sensitivity coupled with significant heating”. *Optics Letters* 31 (2006), pp. 2429–2431.  
DOI: [10.1364/OL.31.002429](https://doi.org/10.1364/OL.31.002429).
- [64] O. M. Marago, P. H. Jones, P. G. Gucciardi, G. Volpe, and A. C. Ferrari. “Optical trapping and manipulation of nanostructures”. *Nature Nanotechnology* 8 (2013), pp. 807–819.
- [65] L. Novotny, R. Bian, and X. Xie. “Theory of Nanometric Optical Tweezers”. *Physical Review Letters* 79 (1997), pp. 645–648.  
DOI: [10.1103/PhysRevLett.79.645](https://doi.org/10.1103/PhysRevLett.79.645).

- [66] O. J. F. Martin and C. Girard. “Controlling and tuning strong optical field gradients at a local probe microscope tip apex”. *Applied Physics Letters* 70 (1997), pp. 705–707.  
DOI: [10.1063/1.118245](https://doi.org/10.1063/1.118245).
- [67] M. Righini, A. S. Zelenina, C. Girard, and R. Quidant. “Parallel and selective trapping in a patterned plasmonic landscape”. *Nature Physics* 3 (2007), pp. 477–480.
- [68] M. Righini, G. Volpe, C. Girard, D. Petrov, and R. Quidant. “Surface plasmon optical tweezers: Tunable optical manipulation in the femtonewton range”. *Physical Review Letters* 100 (2008), pp. 8–11.  
DOI: [10.1103/PhysRevLett.100.186804](https://doi.org/10.1103/PhysRevLett.100.186804).
- [69] A. N. Grigorenko, N. W. Roberts, M. R. Dickinson, and Y. Zhang. “Nanometric optical tweezers based on nanostructured substrates”. *Nature Photonics* 2 (2008), pp. 365–370.  
DOI: [10.1038/nphoton.2008.78](https://doi.org/10.1038/nphoton.2008.78).
- [70] W. Zhang, L. Huang, C. Santschi, and O. J. F. Martin. “Trapping and sensing 10 nm metal nanoparticles using plasmonic dipole antennas”. *Nano Letters* 10 (2010), pp. 1006–1011.  
DOI: [10.1021/nl904168f](https://doi.org/10.1021/nl904168f).
- [71] Z. Kang, H. Lu, J. Chen, K. Chen, F. Xu, and H.-P. Ho. “Plasmonic graded nano-disks as nano-optical conveyor belt”. *Optics Express* 22 (2014), pp. 19567–19572.  
DOI: [10.1364/OE.22.019567](https://doi.org/10.1364/OE.22.019567).
- [72] G. Magno, A. Ecarnot, C. Pin, V. Yam, P. Gogol, R. Mégy, B. Cluzel, and B. Dagens. “Integrated plasmonic nanotweezers for nanoparticle manipulation”. *Optics Letters* 41 (2016), pp. 3679–3682.  
DOI: [10.1364/OL.41.003679](https://doi.org/10.1364/OL.41.003679).
- [73] M. Sergides, V. G. Truong, and S. N. Chormaic. “Highly tunable plasmonic nanoring arrays for nanoparticle manipulation and detection”. *Nanotechnology* 27 (2016), pp. 1–10.  
DOI: [10.1088/0957-4484/27/36/365301](https://doi.org/10.1088/0957-4484/27/36/365301).
- [74] T. Shoji and Y. Tsuboi. “Plasmonic Optical Tweezers toward Molecular Manipulation: Tailoring Plasmonic Nanostructure, Light Source, and Resonant Trapping”. *Journal of Physical Chemistry Letters* 5 (2014), pp. 2957–2967.
- [75] K. Wang, E. Schonbrun, P. Steinvurzel, and K. B. Crozier. “Trapping and rotating nanoparticles using a plasmonic nano-tweezer with an integrated heat sink.” *Nature Communications* 2 (2011), pp. 1–6.  
DOI: [10.1038/ncomms1480](https://doi.org/10.1038/ncomms1480).

- [76] S. B. Smith, L. Finzi, and C. Bustamante. “Direct mechanical measurements of the elasticity of single DNA molecules by using magnetic beads”. *Science* 258 (1992), pp. 1122–1126.  
DOI: [10.1126/science.1439819](https://doi.org/10.1126/science.1439819).
- [77] J. Lipfert, J. W. J. Kerssemakers, T. Jager, and N. H. Dekker. “Magnetic torque tweezers: measuring torsional stiffness in DNA and RecA-DNA filaments.” *Nature Methods* 7 (2010), pp. 977–980.  
DOI: [10.1038/nmeth.1520](https://doi.org/10.1038/nmeth.1520).
- [78] C. Gosse and V. Croquette. “Magnetic tweezers: micromanipulation and force measurement at the molecular level.” *Biophysical Journal* 82 (2002), pp. 3314–3329.
- [79] J. A. Abels, F. Moreno-Herrero, T. van der Heijden, C. Dekker, and N. H. Dekker. “Single-molecule measurements of the persistence length of double-stranded RNA.” *Biophysical Journal* 88 (2005), pp. 2737–2744.  
DOI: [10.1529/biophysj.104.052811](https://doi.org/10.1529/biophysj.104.052811).
- [80] D. A. Koster, V. Croquette, C. Dekker, S. Shuman, and N. H. Dekker. “Friction and torque govern the relaxation of DNA supercoils by eukaryotic topoisomerase IB.” *Nature* 434 (2005), pp. 671–674.  
DOI: [10.1038/nature03395](https://doi.org/10.1038/nature03395).
- [81] A. H. B. de Vries, J. S. Kanger, B. E. Krenn, and R. van Driel. “Patterned electroplating of micrometer scale magnetic structures on glass substrates”. *Journal of Microelectromechanical Systems* 13 (2004), pp. 391–395.  
DOI: [10.1109/JMEMS.2004.828724](https://doi.org/10.1109/JMEMS.2004.828724).
- [82] A. H. B. de Vries, B. E. Krenn, R. van Driel, and J. S. Kanger. “Micro magnetic tweezers for nanomanipulation inside live cells.” *Biophysical Journal* 88 (2005), pp. 2137–2144.  
DOI: [10.1529/biophysj.104.052035](https://doi.org/10.1529/biophysj.104.052035).
- [83] W. Guan, S. Joseph, J. H. Park, P. S. Krstić, and M. A. Reed. “Paul trapping of charged particles in aqueous solution”. *Proceedings of the National Academy of Sciences of the United States of America* 108 (2011), pp. 9326–9330.  
DOI: [10.1073/pnas.1100977108](https://doi.org/10.1073/pnas.1100977108).
- [84] I. Alda, J. Berthelot, R. A. Rica, and R. Quidant. “Trapping and manipulation of individual nanoparticles in a planar Paul trap”. *Applied Physics Letters* 109 (2016), pp. 1–4.  
DOI: [10.1063/1.4965859](https://doi.org/10.1063/1.4965859).

- [85] R. Hölzel, N. Calander, Z. Chiragwandi, M. Willander, and F. F. Bier. “Trapping Single Molecules by Dielectrophoresis”. *Physical Review Letters* 95 (2005), p. 128102.  
DOI: [10.1103/PhysRevLett.95.128102](https://doi.org/10.1103/PhysRevLett.95.128102).
- [86] A. Jamshidi, P. J. Pauzauskie, P. J. Schuck, A. T. Ohta, P.-Y. Chiou, J. Chou, P. Yang, and M. C. Wu. “Dynamic manipulation and separation of individual semiconducting and metallic nanowires.” *Nature Photonics* 2 (2008), pp. 86–89.  
DOI: [10.1038/nphoton.2007.277](https://doi.org/10.1038/nphoton.2007.277).
- [87] G. Mernier, N. Piacentini, T. Braschler, N. Demierre, and P. Renaud. “Continuous-flow electrical lysis device with integrated control by dielectrophoretic cell sorting.” *Lab on a chip* 10 (2010), pp. 2077–2082.  
DOI: [10.1039/c000977f](https://doi.org/10.1039/c000977f).
- [88] A. E. Cohen and W. E. Moemer. “Method for trapping and manipulating nanoscale objects in solution”. *Applied Physics Letters* 86 (2005), pp. 1–3.  
DOI: [10.1063/1.1872220](https://doi.org/10.1063/1.1872220).
- [89] A. E. Cohen. “Control of Nanoparticles with Arbitrary Two-Dimensional Force Fields”. *Physical Review Letters* 94 (2005), pp. 1–4.  
DOI: [10.1103/PhysRevLett.94.118102](https://doi.org/10.1103/PhysRevLett.94.118102).
- [90] A. E. Cohen and W. E. Moerner. “Suppressing Brownian motion of individual biomolecules in solution”. *Proceedings of the National Academy of Sciences of the United States of America* 103 (2006), pp. 4362–4365.  
DOI: [10.1073/pnas.0509976103](https://doi.org/10.1073/pnas.0509976103).
- [91] Q. Wang, R. H. Goldsmith, Y. Jiang, S. D. Bockenhauer, and W. E. Moerner. “Probing Single Biomolecules in Solution Using the Anti-Brownian Electrokinetic (ABEL) Trap”. *Accounts of Chemical Research* 45 (2012), pp. 1955–1964.  
DOI: [10.1021/ar200304t](https://doi.org/10.1021/ar200304t).
- [92] Q. Wang and W. E. Moerner. “Single-molecule motions enable direct visualization of biomolecular interactions in solution”. *Nature Methods* 11 (2014), pp. 555–558.
- [93] K. H. Lam. “Recent Development of Single Beam Acoustic Tweezer”. *Austin J Biotechnol Bioeng* 2 (2015), pp. 1–2.
- [94] J. Shi, D. Ahmed, X. Mao, S.-C. S. Lin, A. Lawit, and T. J. Huang. “Acoustic tweezers: patterning cells and microparticles using standing surface acoustic waves (SSAW).” *Lab on a chip* 9 (2009), pp. 2890–2895.  
DOI: [10.1039/b910595f](https://doi.org/10.1039/b910595f).

- [95] X. Ding, S.-C. S. Lin, B. Kiraly, H. Yue, S. Li, I.-K. Chiang, J. Shi, S. J. Benkovic, and T. J. Huang. “On-chip manipulation of single microparticles, cells, and organisms using surface acoustic waves.” *Proceedings of the National Academy of Sciences of the United States of America* 109 (2012), pp. 11105–11109.  
DOI: [10.1073/pnas.1209288109](https://doi.org/10.1073/pnas.1209288109).
- [96] K. H. Lam, Y. Li, Y. Li, H. G. Lim, Q. Zhou, and K. K. Shung. “Multi-functional single beam acoustic tweezer for non-invasive cell/organism manipulation and tissue imaging”. *Scientific Reports* 6 (2016), pp. 1–7.  
DOI: [10.1038/srep37554](https://doi.org/10.1038/srep37554).
- [97] T. T. Perkins, D. E. Smith, and S. Chu. “Single Polymer Dynamics in an Elongational Flow”. *Science* 276 (1997), pp. 2016–2021.  
DOI: [10.1126/science.276.5321.2016](https://doi.org/10.1126/science.276.5321.2016).
- [98] E. M. Johnson-Chavarria, M. Tanyeri, and C. M. Schroeder. “A Microfluidic-based Hydrodynamic Trap for Single Particles”. *Journal of Visualized Experiments* 47 (2011).  
DOI: [10.3791/2517](https://doi.org/10.3791/2517).
- [99] F. M. Weinert and D. Braun. “An Optical Conveyor for Molecules”. *Nano Letters* 9 (2009), pp. 4264–4267.  
DOI: [10.1021/nl902503c](https://doi.org/10.1021/nl902503c).
- [100] D. Rings, R. Schachoff, M. Selmke, F. Cichos, and K. Kroy. “Hot Brownian Motion”. *Physical Review Letters* 105 (2010), pp. 1–4.  
DOI: [10.1103/PhysRevLett.105.090604](https://doi.org/10.1103/PhysRevLett.105.090604).
- [101] J. Chen, H. Cong, F.-C. Loo, Z. Kang, M. Tang, H. Zhang, S.-Y. Wu, S.-K. Kong, and H.-P. Ho. “Thermal gradient induced tweezers for the manipulation of particles and cells”. *Scientific Reports* 6 (2016), pp. 1–13.
- [102] M. Braun, A. P. Bregulla, K. Günther, M. Mertig, and F. Cichos. “Single Molecules Trapped by Dynamic Inhomogeneous Temperature Fields”. *Nano Letters* 15 (2015), pp. 5499–5505.  
DOI: [10.1021/acs.nanolett.5b01999](https://doi.org/10.1021/acs.nanolett.5b01999).
- [103] J. Tae Kim, S. Spindler, and V. Sandoghdar. “Scanning-aperture trapping and manipulation of single charged nanoparticles.” *Nature Communications* 5 (2014), pp. 1–6.  
DOI: [10.1038/ncomms4380](https://doi.org/10.1038/ncomms4380).
- [104] S. Fringes, M. Skaug, and A. W. Knoll. “In situ contrast calibration to determine the height of individual diffusing nanoparticles in a tunable confinement”. *Journal of Applied Physics* 119 (2016), pp. 1–28.  
DOI: [10.1063/1.4939070](https://doi.org/10.1063/1.4939070).

- [105] N. Mojarad. “Nanoparticles in Confined Optical and Electrostatic Fields: Theory and Experiment”. PhD thesis. ETH Zurich, 2011.
- [106] W. L. W. Hau, D. W. Trau, N. J. Sucher, M. Wong, and Y. Zohar. “Surface-chemistry technology for microfluidics”. *Journal of Micromechanics and Microengineering* 13 (2003), pp. 272–278. DOI: [10.1088/0960-1317/13/2/315](https://doi.org/10.1088/0960-1317/13/2/315).
- [107] S. H. Behrens and D. G. Grier. “The charge of glass and silica surfaces”. *The Journal of Chemical Physics* 115 (2001), pp. 6716–6721. DOI: [10.1063/1.1404988](https://doi.org/10.1063/1.1404988).
- [108] R. K. Iler. *The Chemistry of Silica*. New York: John Wiley & Sons, 1979.
- [109] O. Stern. “Zur Theorie der Elektrolytischen Doppelschicht”. *Zeitschrift für Elektrochemie* 30 (1924), pp. 508–516. DOI: [10.1002/bbpc.192400182](https://doi.org/10.1002/bbpc.192400182).
- [110] M. Gouy. “Sur la constitution de la charge électrique à la surface d’un électrolyte”. *Journal de Physique Théorique et Appliquée* 9 (1910), pp. 457–468. DOI: [10.1051/jphysap:019100090045700](https://doi.org/10.1051/jphysap:019100090045700).
- [111] D. L. Chapman. “A contribution to the theory of electrocapillarity”. *Philosophical Magazine Series 6* 25 (1913), pp. 475–481. DOI: [10.1080/14786440408634187](https://doi.org/10.1080/14786440408634187).
- [112] D. C. Grahame. “Diffuse Double Layer Theory for Electrolytes of Unsymmetrical Valence Types”. *The Journal of Chemical Physics* 21 (1953), pp. 1054–1060. DOI: [10.1063/1.1699109](https://doi.org/10.1063/1.1699109).
- [113] W. Sparreboom, A. van den Berg, and J. C. T. Eijkel. “Principles and applications of nanofluidic transport.” *Nature Nanotechnology* 4 (2009), pp. 713–720. DOI: [10.1038/nnano.2009.332](https://doi.org/10.1038/nnano.2009.332).
- [114] H. Daiguji. “Ion transport in nanofluidic channels”. *Chemical Society Reviews* 39 (2010), pp. 901–911. DOI: [10.1039/B820556F](https://doi.org/10.1039/B820556F).
- [115] R. Chantiwas, S. Park, S. A. Soper, B. C. Kim, S. Takayama, V. Sunkara, H. Hwang, and Y.-K. Cho. “Flexible fabrication and applications of polymer nanochannels and nanoslits.” *Chemical Society Reviews* 40 (2011), pp. 3677–3702. DOI: [10.1039/c0cs00138d](https://doi.org/10.1039/c0cs00138d).
- [116] M. Krishnan. “Electrostatic free energy for a confined nanoscale object in a fluid.” *The Journal of Chemical Physics* 138 (2013). DOI: [10.1063/1.4795087](https://doi.org/10.1063/1.4795087).



- [117] W. Reisner, N. B. Larsen, H. Flyvbjerg, J. O. Tegenfeldt, and A. Kristensen. “Directed self-organization of single DNA molecules in a nanoslit via embedded nanopit arrays.” *Proceedings of the National Academy of Sciences of the United States of America* 106 (2009), pp. 79–84.  
DOI: [10.1073/pnas.0811468106](https://doi.org/10.1073/pnas.0811468106).
- [118] A. R. Klotz, H. B. Brandão, and W. W. Reisner. “Diffusion resonance of nanoconfined polymers”. *Macromolecules* 45 (2012), pp. 2122–2127.  
DOI: [10.1021/ma202596j](https://doi.org/10.1021/ma202596j).
- [119] A. R. Klotz, M. Mamaev, L. Duong, H. W. De Haan, and W. W. Reisner. “Correlated Fluctuations of DNA between Nanofluidic Entropic Traps”. *Macromolecules* 48 (2015), pp. 4742–4747.  
DOI: [10.1021/acs.macromol.5b00961](https://doi.org/10.1021/acs.macromol.5b00961).
- [120] N. Mojarad, V. Sandoghdar, and M. Krishnan. “Measuring three-dimensional interaction potentials using optical interference.” *Optics Express* 21 (2013), pp. 9377–9389.
- [121] M. Celebrano, C. Rosman, C. Sönnichsen, and M. Krishnan. “Angular trapping of anisometric nano-objects in a fluid.” *Nano Letters* 12 (2012), pp. 5791–5796.  
DOI: [10.1021/nl303099c](https://doi.org/10.1021/nl303099c).
- [122] C. J. Myers, M. Celebrano, and M. Krishnan. “Information storage and retrieval in a single levitating colloidal particle.” *Nature Nanotechnology* 10 (2015), pp. 886–891.  
DOI: [10.1038/nnano.2015.173](https://doi.org/10.1038/nnano.2015.173).
- [123] G. Kokot, M. I. Bernalova, and M. Krishnan. “Measured electrical charge of SiO<sub>2</sub> in polar and nonpolar media”. *Journal of Chemical Physics* 145 (2016), pp. 1–8.  
DOI: [10.1063/1.4967401](https://doi.org/10.1063/1.4967401).
- [124] M. A. Gerspach, N. Mojarad, D. Sharma, T. Pfohl, and Y. Ekinici. “Nanofluidic lab-on-a-chip trapping devices for screening electrostatics in concentration gradients”. *Microelectronic Engineering* 175 (2017), pp. 17–22.  
DOI: [10.1016/j.mee.2016.12.017](https://doi.org/10.1016/j.mee.2016.12.017).
- [125] D. Sharma, M. A. Gerspach, T. Pfohl, R. Y. H. Lim, and Y. Ekinici. “Single positively charged particle trapping in nanofluidic systems”. *Microelectronic Engineering* 175 (2017), pp. 43–49.  
DOI: [10.1016/j.mee.2017.01.001](https://doi.org/10.1016/j.mee.2017.01.001).

- [126] T. Funatsu, Y. Harada, M. Tokunaga, K. Saito, and T. Yanagida. “Imaging of single fluorescent molecules and individual ATP turnovers by single myosin molecules in aqueous solution”. *Nature* 374 (1995), pp. 555–559.  
DOI: [10.1038/374555a0](https://doi.org/10.1038/374555a0).
- [127] T. Funatsu, Y. Harada, H. Higuchi, M. Tokunaga, K. Saito, Y. Ishii, R. D. Vale, and T. Yanagida. “Imaging and nano-manipulation of single biomolecules”. *Biophysical Chemistry* 68 (1997), pp. 63–72.  
DOI: [10.1016/S0301-4622\(97\)00008-2](https://doi.org/10.1016/S0301-4622(97)00008-2).
- [128] E. C. Jensen. “Types of Imaging, Part 2: An Overview of Fluorescence Microscopy”. *Anatomical Record* 295 (2012), pp. 1621–1627.  
DOI: [10.1002/ar.22548](https://doi.org/10.1002/ar.22548).
- [129] I. Rasnik, S. a. McKinney, and T. Ha. “Nonblinking and long-lasting single-molecule fluorescence imaging.” *Nature Methods* 3 (2006), pp. 891–893.  
DOI: [10.1038/nmeth934](https://doi.org/10.1038/nmeth934).
- [130] K. C. Mudumbi *et al.* “Single-point single-molecule FRAP distinguishes inner and outer nuclear membrane protein distribution”. *Nature Communications* 7 (2016), pp. 1–6.  
DOI: [10.1038/ncomms12562](https://doi.org/10.1038/ncomms12562).
- [131] S. Wennmalm, P. Thyberg, L. Xu, and J. Widengren. “Inverse-Fluorescence Correlation Spectroscopy”. *Analytical Chemistry* 81 (2009), pp. 9209–9215.  
DOI: [10.1021/ac9010205](https://doi.org/10.1021/ac9010205).
- [132] T. Sandén, R. Wyss, C. Santschi, G. Hassaïne, C. Deluz, O. J. F. Martin, S. Wennmalm, and H. Vogel. “A zeptoliter volume meter for analysis of single protein molecules.” *Nano Letters* 12 (2012), pp. 370–375.  
DOI: [10.1021/nl2036468](https://doi.org/10.1021/nl2036468).
- [133] T. Sugiura and T. Okada. “Gold-bead scanning near-field optical microscope with laser-force position control”. *Optics Letters* 22 (1997), pp. 1663–1665.
- [134] C. Sönnichsen, S. Geier, N. E. Hecker, G. von Plessen, J. Feldmann, H. Ditlbacher, B. Lamprecht, J. R. Krenn, F. R. Aussenegg, V. Z.-H. Chan, J. P. Spatz, and M. Moeller. “Spectroscopy of single metallic nanoparticles using total internal reflection microscopy”. *Applied Physics Letters* 77 (2000), pp. 2949–2951.  
DOI: [10.1063/1.1323553](https://doi.org/10.1063/1.1323553).

- [135] S. Schultz, D. R. Smith, J. J. Mock, and D. a. Schultz. “Single-target molecule detection with nonbleaching multicolor optical immunolabels.” *Proceedings of the National Academy of Sciences of the United States of America* 97 (2000), pp. 996–1001.  
DOI: [10.1073/pnas.97.3.996](https://doi.org/10.1073/pnas.97.3.996).
- [136] S. Fringes, F. Holzner, and A. W. Knoll. “The Nanofluidic Confinement Apparatus: Studying confinement dependent nanoparticle behavior and diffusion” (2017), pp. 1–20.
- [137] J. Ortega Arroyo, J. Andrecka, K. M. Spillane, N. Billington, Y. Takagi, J. R. Sellers, and P. Kukura. “Label-free, all-optical detection, imaging, and tracking of a single protein”. *Nano Letters* 14 (2014), pp. 2065–2070.  
DOI: [10.1021/nl500234t](https://doi.org/10.1021/nl500234t).
- [138] K. I. Mortensen, L. S. Churchman, J. a. Spudich, and H. Flyvbjerg. “Optimized localization analysis for single-molecule tracking and super-resolution microscopy.” *Nature Methods* 7 (2010), pp. 377–381.  
DOI: [10.1038/nmeth.1447](https://doi.org/10.1038/nmeth.1447).
- [139] R. E. Thompson, D. R. Larson, and W. W. Webb. “Precise nanometer localization analysis for individual fluorescent probes.” *Biophysical Journal* 82 (2002), pp. 2775–2783.  
DOI: [10.1016/S0006-3495\(02\)75618-X](https://doi.org/10.1016/S0006-3495(02)75618-X).
- [140] M. K. Cheezum, W. F. Walker, and W. H. Guilford. “Quantitative comparison of algorithms for tracking single fluorescent particles.” *Biophysical Journal* 81 (2001), pp. 2378–2388.  
DOI: [10.1016/S0006-3495\(01\)75884-5](https://doi.org/10.1016/S0006-3495(01)75884-5).
- [141] A. Kusumi, Y. Sako, and M. Yamamoto. “Confined lateral diffusion of membrane receptors as studied by single particle tracking (nanovid microscopy). Effects of calcium-induced differentiation in cultured epithelial cells”. *Biophysical Journal* 65 (1993), pp. 2021–2040.  
DOI: [10.1016/S0006-3495\(93\)81253-0](https://doi.org/10.1016/S0006-3495(93)81253-0).
- [142] H. A. Kramers. “Brownian motion in a field of force and the diffusion model of chemical reactions”. *Physica* 7 (1940), pp. 284–304.  
DOI: [http://dx.doi.org/10.1016/S0031-8914\(40\)90098-2](http://dx.doi.org/10.1016/S0031-8914(40)90098-2).
- [143] A. Libchaber and A. Simon. “Escape and Synchronization of a Brownian Particle”. *The American Physical Society* 68 (1992), pp. 3375–3378.
- [144] J. Howard. *Mechanics of Motor Proteins and the Cytoskeleton*. Springer Berlin Heidelberg, 2001.  
DOI: [10.1007/3-540-45701-1\\_2](https://doi.org/10.1007/3-540-45701-1_2).

- [145] G. Decher, J. Hong, and J. Schmitt. “Buildup of ultrathin multilayer films by a self-assembly process: III. Consecutively alternating adsorption of anionic and cationic polyelectrolytes on charged surfaces”. *Thin Solid Films* 210-211 (1992), pp. 831–835.  
DOI: [10.1016/0040-6090\(92\)90417-A](https://doi.org/10.1016/0040-6090(92)90417-A).
- [146] G. Decher. “Fuzzy Nanoassemblies: Toward Layered Polymeric Multicomposites”. *Science* 277 (1997), pp. 1232–1237.  
DOI: [10.1126/science.277.5330.1232](https://doi.org/10.1126/science.277.5330.1232).
- [147] R. Dootz, J. Nie, B. Du, S. Herminghaus, and T. Pfohl. “Raman and Surface Enhanced Raman Microscopy of Microstructured Polyethyleneimine / DNA Multilayers”. *Langmuir* 22 (2006), pp. 1735–1741.
- [148] W.-A. C. Bauer, M. Fischlechner, C. Abell, and W. T. S. Huck. “Hydrophilic PDMS microchannels for high-throughput formation of oil-in-water microdroplets and water-in-oil-in-water double emulsions.” *Lab on a chip* 10 (2010), pp. 1814–1819.  
DOI: [10.1039/c004046k](https://doi.org/10.1039/c004046k).
- [149] S. Köster, D. Steinhauser, and T. Pfohl. “Brownian motion of actin filaments in confining microchannels”. *Journal of Physics: Condensed Matter* 17 (2005), S4091–S4104.  
DOI: [10.1088/0953-8984/17/49/006](https://doi.org/10.1088/0953-8984/17/49/006).
- [150] S. Köster, J. Kierfeld, and T. Pfohl. “Characterization of single semiflexible filaments under geometric constraints.” *The European Physical Journal* 25 (2008), pp. 439–449.  
DOI: [10.1140/epje/i2007-10312-3](https://doi.org/10.1140/epje/i2007-10312-3).
- [151] J. O. Tegenfeldt, C. Prinz, H. Cao, S. Chou, W. W. Reisner, R. Riehn, Y. M. Wang, E. C. Cox, J. C. Sturm, P. Silberzan, and R. H. Austin. “The dynamics of genomic-length DNA molecules in 100-nm channels.” *Proceedings of the National Academy of Sciences of the United States of America* 101 (2004), pp. 10979–10983.  
DOI: [10.1073/pnas.0403849101](https://doi.org/10.1073/pnas.0403849101).
- [152] C. F. Bohren and D. R. Huffman. *Absorption and Scattering of Light by Small Particles*. Vol. 16. Wiley-VCH Verlag GmbH, 1998.
- [153] P. Mao and J. Han. “Fabrication and characterization of 20 nm planar nanofluidic channels by glass-glass and glass-silicon bonding.” *Lab on a chip* 5 (2005), pp. 837–844.  
DOI: [10.1039/b502809d](https://doi.org/10.1039/b502809d).

- [154] N. M. Mojarad, G. Zumofen, V. Sandoghdar, and M. Agio. “Metal nanoparticles in strongly confined beams: transmission, reflection and absorption”. en. *Journal of the European Optical Society: Rapid Publications* 4 (2009), pp. 1–6.  
DOI: [10.2971/jeos.2009.09014](https://doi.org/10.2971/jeos.2009.09014).
- [155] D. Jing and B. Bhushan. “Quantification of surface charge density and its effect on boundary slip.” *Langmuir* 29 (2013), pp. 6953–6963.  
DOI: [10.1021/la401168w](https://doi.org/10.1021/la401168w).
- [156] M. A. Gerspach, N. Mojarad, T. Pfohl, and Y. Ekinici. “Glass-based geometry-induced electrostatic trapping devices for improved scattering contrast imaging of nano-objects”. *Microelectronic Engineering* 145 (2015), pp. 43–48.  
DOI: [10.1016/j.mee.2015.02.035](https://doi.org/10.1016/j.mee.2015.02.035).
- [157] N. Strelnikova, F. Herren, C.-A. Schoenenberger, and T. Pfohl. “Formation of Actin Networks in Microfluidic Concentration Gradients”. *Frontiers in Materials* 3 (2016), pp. 1–9.  
DOI: [10.3389/fmats.2016.00020](https://doi.org/10.3389/fmats.2016.00020).
- [158] A. Fick. “Ueber Diffusion”. *Annalen der Physik* 170 (1855), pp. 59–86.  
DOI: [10.1002/andp.18551700105](https://doi.org/10.1002/andp.18551700105).
- [159] J. Tóthová, G. Vasziová, L. Glod, and V. Lisý. “Langevin theory of anomalous Brownian motion made simple”. *European Journal of Physics* 32 (2011), pp. 645–655.  
DOI: [10.1088/0143-0807/32/3/002](https://doi.org/10.1088/0143-0807/32/3/002).
- [160] C. D. Chin, V. Linder, and S. K. Sia. “Commercialization of microfluidic point-of-care diagnostic devices”. *Lab on a chip* 12 (2012), pp. 2118–2134.  
DOI: [10.1039/c2lc21204h](https://doi.org/10.1039/c2lc21204h).
- [161] M. L. Kovarik, P. C. Gach, D. M. Ornoff, Y. Wang, J. Balowski, L. Farrag, and N. L. Allbritton. “Micro total analysis systems for cell biology and biochemical assays”. *Analytical Chemistry* 84 (2012), pp. 516–540.  
DOI: [10.1021/ac202611x](https://doi.org/10.1021/ac202611x).
- [162] P. Neuzi, S. Giselbrecht, K. Länge, T. J. Huang, and A. Manz. “Revisiting lab-on-a-chip technology for drug discovery.” *Nature Reviews Drug Discovery* 11 (2012), pp. 620–632.  
DOI: [10.1038/nrd3799](https://doi.org/10.1038/nrd3799).
- [163] H. Schmidt and A. R. Hawkins. “The photonic integration of non-solid media using optofluidics”. *Nature Photonics* 5 (2011), pp. 598–604.  
DOI: [10.1038/nphoton.2011.163](https://doi.org/10.1038/nphoton.2011.163).

- [164] P. N. Nge, C. I. Rogers, and A. T. Woolley. “Advances in microfluidic materials, functions, integration, and applications”. *Chemical Reviews* 113 (2013), pp. 2550–2583.  
DOI: [10.1021/cr300337x](https://doi.org/10.1021/cr300337x).
- [165] C. Duan, W. Wang, and Q. Xie. “Review article: Fabrication of nanofluidic devices”. *Biomicrofluidics* 7 (2013), p. 26501.  
DOI: [10.1063/1.4794973](https://doi.org/10.1063/1.4794973).
- [166] C. Wu, T. G. Lin, Z. Zhan, Y. Li, S. C. Tung, W. C. Tang, and W. J. Li. “Fabrication of all-transparent polymer-based and encapsulated nanofluidic devices using nano-indentation lithography”. *Microsystems & Nanoengineering* 3 (2017), pp. 1–9.  
DOI: [10.1038/micronano.2016.84](https://doi.org/10.1038/micronano.2016.84).
- [167] S. Chung, J. H. Lee, M. W. Moon, J. Han, and R. D. Kamm. “Non-lithographic wrinkle nanochannels for protein preconcentration”. *Advanced Materials* 20 (2008), pp. 3011–3016.  
DOI: [10.1002/adma.200701715](https://doi.org/10.1002/adma.200701715).
- [168] D. Huh, K. L. Mills, X. Zhu, M. A. Burns, M. Thouless, and S. Takayama. “Tunable elastomeric nanochannels for nanofluidic manipulation.” *Nature Materials* 6 (2007), pp. 424–428.  
DOI: [10.1038/nmat1907](https://doi.org/10.1038/nmat1907).
- [169] S.-M. Park, Y. S. Huh, H. G. Craighead, and D. Erickson. “A method for nanofluidic device prototyping using elastomeric collapse.” *Proceedings of the National Academy of Sciences of the United States of America* 106 (2009), pp. 15549–15554.  
DOI: [10.1073/pnas.0904004106](https://doi.org/10.1073/pnas.0904004106).
- [170] H. Schiff, C. Spreu, M. Saidani, M. Bednarzik, J. Gobrecht, A. Klukowska, F. Reuther, G. Gruetzner, and H. H. Solak. “Transparent hybrid polymer stamp copies with sub-50-nm resolution for thermal and UV-nanoimprint lithography”. *Journal of Vacuum Science & Technology B: Microelectronics and Nanometer Structures Processing, Measurement, and Phenomena* 27 (2009), pp. 2846–2849.  
DOI: [10.1116/1.3250207](https://doi.org/10.1116/1.3250207).
- [171] H. Schiff, C. Spreu, A. Schleunitz, J. Gobrecht, A. Klukowska, F. Reuther, and G. Gruetzner. “Easy mask-mold fabrication for combined nanoimprint and photolithography”. *Journal of Vacuum Science & Technology B: Microelectronics and Nanometer Structures Processing, Measurement, and Phenomena* 27 (2009), pp. 2850–2853.  
DOI: [10.1116/1.3250260](https://doi.org/10.1116/1.3250260).

- [172] V. J. Cadarso, T. Kiefer, V. Auzelyte, H. Atasoy, G. Gruetzner, and J. Brugger. “Direct imprinting of organic–inorganic hybrid materials into high aspect ratio sub-100 nm structures”. *Microsystem Technologies* 20 (2014), pp. 1961–1966.  
DOI: [10.1007/s00542-013-2016-4](https://doi.org/10.1007/s00542-013-2016-4).
- [173] Y. Y. Huang, W. Zhou, K. J. Hsia, E. Menard, J. U. Park, J. A. Rogers, and A. G. Alleyne. “Stamp collapse in soft lithography”. *Langmuir* 21 (2005), pp. 8058–8068.  
DOI: [10.1021/la0502185](https://doi.org/10.1021/la0502185).
- [174] J. Lee, Y. K. Yun, Y. Kim, and K. Jo. “PDMS nanoslits without roof collapse”. *Bulletin of the Korean Chemical Society* 30 (2009), pp. 1793–1797.  
DOI: [10.5012/bkcs.2009.30.8.1793](https://doi.org/10.5012/bkcs.2009.30.8.1793).
- [175] Z. Wang, A. A. Volinsky, and N. D. Gallant. “Crosslinking effect on polydimethylsiloxane elastic modulus measured by custom-built compression instrument”. *Journal of Applied Polymer Science* 131 (2014), pp. 1–4.  
DOI: [10.1002/app.41050](https://doi.org/10.1002/app.41050).
- [176] J.-J. Kim, Y. Lee, H. G. Kim, K.-J. Choi, H.-S. Kweon, S. Park, and K.-H. Jeong. “Biologically inspired LED lens from cuticular nanostructures of firefly lantern.” *Proceedings of the National Academy of Sciences of the United States of America* 109 (2012), pp. 18674–18678.  
DOI: [10.1073/pnas.1213331109](https://doi.org/10.1073/pnas.1213331109).
- [177] M. Bender, U. Plachetka, J. Ran, A. Fuchs, B. Vratzov, H. Kurz, T. Glinsner, and F. Lindner. “High resolution lithography with PDMS molds”. *Journal of Vacuum Science & Technology B: Microelectronics and Nanometer Structures* 22 (2004), pp. 3229–3232.  
DOI: [10.1116/1.1824057](https://doi.org/10.1116/1.1824057).
- [178] A. L. Loeb, J. T. G. Overbeek, and P. H. Wiersema. *The electrical double layer around a spherical colloid particle: computation of the potential, charge density, and free energy of the electrical double layer around a spherical colloid particle*. Cambridge: Massachusetts Institute of Technology, 1961, p. 375.
- [179] H. Kalka. “Electrical Conductivity (EC)” (2015), Webpage, date accessed 2017-06-20.  
DOI: <http://www.aqion.de/site/130>.
- [180] G. Whitesides and A. Stroock. “Flexible methods for microfluidics”. *Physics Today* 54 (2001), pp. 42–48.  
DOI: [10.1063/1.1387591](https://doi.org/10.1063/1.1387591).

- [181] M. A. Unger, H. P. Chou, T. Thorsen, A. Scherer, and S. R. Quake. “Monolithic Microfabricated Valves and Pumps by Multilayer Soft Lithography”. *Science* 288 (2000), pp. 113–116.  
DOI: [10.1126/science.288.5463.113](https://doi.org/10.1126/science.288.5463.113).
- [182] J. W. Hong and S. R. Quake. “Integrated nanoliter systems.” *Nature Biotechnology* 21 (2003), pp. 1179–1183.  
DOI: [10.1038/nbt871](https://doi.org/10.1038/nbt871).
- [183] T. Thorsen, S. J. Maerkl, and S. R. Quake. “Microfluidic large-scale integration”. *Science* 298 (2002), pp. 580–584.  
DOI: [10.1126/science.1076996](https://doi.org/10.1126/science.1076996).
- [184] D. B. Weibel, M. Kruithof, S. Potenta, S. K. Sia, A. Lee, and G. M. Whitesides. “Torque-Actuated Valves for Microfluidics”. *Analytical Chemistry* 77 (2005), pp. 4726–4733.
- [185] S. E. Hulme, S. S. Shevkopyas, and G. M. Whitesides. “Incorporation of prefabricated screw, pneumatic, and solenoid valves into microfluidic devices.” *Lab on a chip* 9 (2009), pp. 79–86.  
DOI: [10.1039/b809673b](https://doi.org/10.1039/b809673b).
- [186] M. E. Brennich, J.-F. Nolting, C. Dammann, B. Nöding, S. Bauch, H. Herrmann, T. Pfohl, and S. Köster. “Dynamics of intermediate filament assembly followed in micro-flow by small angle X-ray scattering.” *Lab on a chip* 11 (2011), pp. 708–716.  
DOI: [10.1039/c0lc00319k](https://doi.org/10.1039/c0lc00319k).
- [187] R. Urbani, F. Westermeier, B. Banusch, M. Sprung, and T. Pfohl. “Brownian and advective dynamics in microflow studied by coherent X-ray scattering experiments”. *Journal of Synchrotron Radiation* 23 (2016), pp. 1401–1408.  
DOI: [10.1107/S1600577516012613](https://doi.org/10.1107/S1600577516012613).
- [188] D. C. Corporation. “Electronics Sylgard ® 184 Silicone Elastomer”. *Product Datasheet* (2013).  
DOI: [10.1017/CB09781107415324.004](https://doi.org/10.1017/CB09781107415324.004).
- [189] Malvern Instruments. *Surface Zeta Potential Cell (ZEN1020)*. 2011.
- [190] I. Heller, T. P. Hoekstra, G. A. King, E. J. G. Peterman, and G. J. L. Wuite. “Optical Tweezers Analysis of DNA - Protein Complexes”. *Chemical Reviews* 114 (2014), pp. 3087–3119.  
DOI: [10.1021/cr4003006](https://doi.org/10.1021/cr4003006).
- [191] I. Brouwer, G. Sitters, A. Candelli, S. J. Heerema, I. Heller, A. J. Melo de, H. Zhang, D. Normanno, M. Modesti, E. J. G. Peterman, and G. J. L. Wuite. “Sliding sleeves of XRCC4–XLF bridge DNA and connect fragments of broken DNA”. *Nature* 535 (2016), pp. 566–569.  
DOI: [10.1038/nature18643](https://doi.org/10.1038/nature18643).



- [192] U. F. Keyser, J. Van Der Does, C. Dekker, and N. H. Dekker. “Optical tweezers for force measurements on DNA in nanopores”. *Review of Scientific Instruments* 77 (2006), pp. 1–9.  
DOI: [10.1063/1.2358705](https://doi.org/10.1063/1.2358705).
- [193] D. C. Duffy, J. C. McDonald, O. J. A. Schueller, and G. M. Whitesides. “Rapid prototyping of microfluidic systems in poly(dimethylsiloxane)”. *Analytical Chemistry* 70 (1998), pp. 4974–4984.  
DOI: [10.1021/ac980656z](https://doi.org/10.1021/ac980656z).
- [194] J. C. McDonald and G. M. Whitesides. “Poly (dimethylsiloxane) as a Material for Fabricating Microfluidic Devices”. *Accounts of Chemical Research* 35 (2002), pp. 491–499.  
DOI: [10.1021/ac001132d](https://doi.org/10.1021/ac001132d).
- [195] J. C. McDonald, D. C. Duffy, J. R. Anderson, and D. T. Chiu. “Fabrication of microfluidic systems in poly (dimethylsiloxane)”. *Electrophoresis* 21 (2000), pp. 27–40.  
DOI: [10.1002/\(SICI\)1522-2683\(20000101\)21:1<27::AID-ELPS27>3.0.CO;2-C](https://doi.org/10.1002/(SICI)1522-2683(20000101)21:1<27::AID-ELPS27>3.0.CO;2-C).
- [196] I. Steinke, M. Walther, F. Lehmkuhler, P. Wochner, J. Valerio, R. Mager, M. A. Schroer, S. Lee, W. Roseker, A. Jain, M. Sikorski, S. Song, R. Hartmann, M. Huth, L. Strüder, M. Sprung, A. Robert, P. H. Fuoss, G. B. Stephenson, and G. Grübel. “A liquid jet setup for x-ray scattering experiments on complex liquids at free-electron laser sources”. *Review of Scientific Instruments* 87 (2016), pp. 1–6.  
DOI: [10.1063/1.4953921](https://doi.org/10.1063/1.4953921).
- [197] D. Wang, U. Weierstall, L. Pollack, and J. Spence. “Double-focusing mixing jet for XFEL study of chemical kinetics”. *Journal of Synchrotron Radiation* 21 (2014), pp. 1364–1366.  
DOI: [10.1107/S160057751401858X](https://doi.org/10.1107/S160057751401858X).
- [198] B. Pedrini, I. Martiel, E. Panepucci, and C. Pradervand. *SwissFEL ESB-MX instrument for fixed target protein crystallography at Swiss-FEL: Concept Design Report*. Tech. rep. 2016.
- [199] L. Isa, K. Kumar, M. Müller, J. Grolig, M. Textor, and E. Reimhult. “Particle lithography from colloidal self-assembly at liquid-liquid interfaces”. *ACS Nano* 4 (2010), pp. 5665–5670.  
DOI: [10.1021/nn101260f](https://doi.org/10.1021/nn101260f).
- [200] W. F. Lin, L. A. Swartz, J. R. Li, Y. Liu, and G. Y. Liu. “Particle lithography enables fabrication of multicomponent nanostructures”. *Journal of Physical Chemistry C* 117 (2013), pp. 23279–23285.  
DOI: [10.1021/jp406239d](https://doi.org/10.1021/jp406239d).

- [201] M. J. Levene, J. Korlach, S. W. Turner, M. Foquet, H. G. Craighead, and W. W. Webb. “Zero-Mode Waveguides for Single-Molecule Analysis at High Concentrations”. *Science* 299 (2003), pp. 682–686.  
DOI: [10.1126/science.1079700](https://doi.org/10.1126/science.1079700).
- [202] J. Eid *et al.* “Real-Time DNA Sequencing from Single Polymerase Molecules”. *Science* 323 (2009), pp. 133–138.  
DOI: [10.1126/science.1162986](https://doi.org/10.1126/science.1162986).
- [203] P. D. N. Hebert, A. Cywinska, S. L. Ball, and J. R. DeWaard. “Biological identifications through DNA barcodes”. *Proceedings of the Royal Society B: Biological Sciences* 270 (2003), pp. 313–321.  
DOI: [10.1098/rspb.2002.2218](https://doi.org/10.1098/rspb.2002.2218).
- [204] S. W. Kowalczyk, L. Kapinos, T. R. Blosser, T. Magalhães, P. van Nies, R. Y. H. Lim, and C. Dekker. “Single-molecule transport across an individual biomimetic nuclear pore complex”. *Nature Nanotechnology* 6 (2011), pp. 433–438.  
DOI: [10.1038/nnano.2011.88](https://doi.org/10.1038/nnano.2011.88).
- [205] T. Jovanovic-Taliman, J. Tetenbaum-Novatt, A. S. McKenney, A. Zilman, R. Peters, M. P. Rout, and B. T. Chait. “Artificial nanopores that mimic the transport selectivity of the nuclear pore complex”. *Nature* 457 (2009), pp. 1023–1027.  
DOI: [10.1038/nature07600](https://doi.org/10.1038/nature07600).
- [206] B. Schäfer, H. Gemeinhardt, V. Uhl, and K. O. Greulich. “Single Molecule DNA Restriction Analysis in the Light Microscope”. *Single Molecules* 1 (2000), pp. 33–40.  
DOI: [10.1002/\(SICI\)1438-5171\(200004\)1:1<33::AID-SIM033>3.0.CO;2-Y](https://doi.org/10.1002/(SICI)1438-5171(200004)1:1<33::AID-SIM033>3.0.CO;2-Y).
- [207] T. E. Harris. “Diffusion with ”Collisions” between Particles”. *Journal of Applied Probability* 2 (1965), pp. 323–338.  
DOI: [10.2307/3212197](https://doi.org/10.2307/3212197).
- [208] R. I. Macey and R. M. Oliver. “The Time Dependence of Single File Diffusion”. *Biophysical Journal* 7 (1967), pp. 545–554.
- [209] D. G. Levitt. “Dynamics of a Single-File Pore: Non-Fickian Behavior”. *Physical Review A* 8 (1973), pp. 3050–3054.  
DOI: [10.1103/PhysRevA.8.3050](https://doi.org/10.1103/PhysRevA.8.3050).
- [210] J. Sane, J. T. Padding, and A. A. Louis. “The crossover from single file to Fickian diffusion”. *Faraday Discussions* 144 (2010), pp. 285–299.  
DOI: [10.1039/B905378F](https://doi.org/10.1039/B905378F).

- [211] A. V. A. Kumar. “Crossover from normal diffusion to single-file diffusion of particles in a one-dimensional channel: LJ particles in zeolite zsm-22”. *Molecular Physics* 113 (2015), pp. 1306–1310.  
DOI: [10.1080/00268976.2014.989929](https://doi.org/10.1080/00268976.2014.989929).



## Optical detection system

### A.1. Optical setup

The scaled built up of the optical system and its components, including the iSCAT detection system and the pressure control system is shown in Fig. A.1. The scanning mirrors are synchronized with the triggering of the camera using an analog output LabView controller and a custom built LabView software. The laser intensity can be adjusted with a motorized OD 0 – 2 filter wheel. This can be either done analog with a hand-held control knob or digital by using the LabView software. The pressure applied in the pneumatic PDMS devices is detected by the digital manometer. The data are digitalized, recorded and transferred to the computer during the exposure using an Arduino microcontroller.

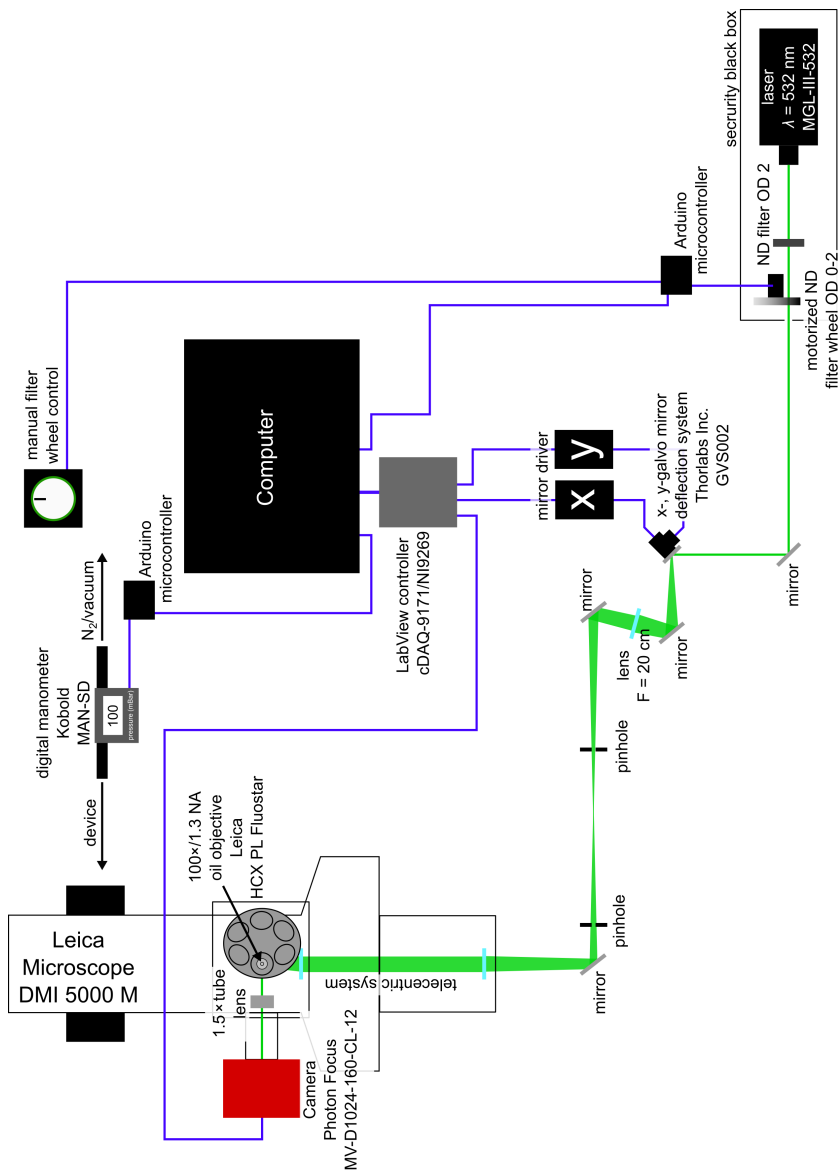


Figure A.1.: Schematic of the iSCAT system including the pressure reading system

## A.2. Software and performance of the system

The software which controls the iSCAT setup and reads the pressure values was written in LabView. It consists of four sub-windows as showed in Fig. A.2 – A.5.

### Main control

In the main control window, the LabView controller is selected and imaging parameters, such as exposure time, image size, or frame rate can be set. This control window triggers the camera by 5V rectangular electric pulses. The time (width) of the pulse defines the exposure time. Further it allows to select microscope parameters, which are saved after each acquisition together with the imaging and mirror parameters and the date and time. A comment field allows to write further observations during the acquisition or to write further information such as the particle size or trap dimensions. The comments can be saved together with all other parameters after each acquisition.

### Mirror control

In the mirror control window, the parameters for each scanning mirror ( $x$  and  $y$ ) are set individually. Scanning mirror parameters are the signal type (triangle, sine, rectangle or sawtooth), scanning frequency, amplitude, phase and offset. The amplitudes are set as a voltage in mV. From the manufacturer guideline, the highest voltage that can be set is 110 mV, which results in a scanned field of view of  $25\ \mu\text{m} \times 25\ \mu\text{m}$  on the sample. The highest frequency that can be set is 1 kHz (manufacturer guideline). For an uniform illumination, at least 10 scans per exposure time of each mirror should be made and the frequency of the two mirrors should slightly differ to obtain a rectangular illuminated field. This results in a minimum exposure time of 10 ms and a frame time of 11.1 ms (exposure time + readout time) and thus highest acquisition rate of 90 Hz. However, the scanning of the mirrors can be turned of, or only one mirror can be used for scanning to achieve shorter exposure times down to 1 ms. The maximum acquisition rate however is limited to 111 Hz (duty cycle of the LabView controller).

### Neutral density filter wheel

The neutral density (ND) filter wheel (OD 0-2) is used to adjust the intensity of the laser beam. It is equipped with a  $360^\circ$  servo motor connected to an Arduino Uno microcontroller. The filter wheel can be turned either manually by a potentiometer or digital with the control software, which is connected over a serial RS232 communication to the microcontroller.

## Pressure control

The pressure control window records the pressure values of the manometer during an acquisition and saves the data into a text file. Additionally to each value, the image frame and time (from start zero) is saved. The data can be afterwards imported into MATLAB or another statistical software. The analog pressure values of the manometer are first digitalized by a second Arduino Uno microcontroller and then transferred to the LabView software over a serial RS232 communication.

## A.3. Two-dimensional sub-diffraction localization

The localization accuracy  $\delta x_0$  and  $\delta y_0$  can be derived from the deviation of a perfect Gaussian fit over an imaged particle. The measured values for all three device systems used in this work and for several sizes of Au NPs are summarized in Tab. A.1. Comparing the results to the measured SNR obtained for the different systems and particle sizes, it is clear that larger SNR result in higher tracking precision as expected from Eq. 2.20.

Device material	Particle diameter $d$ (nm)	$\delta x_0$ (nm)	$\delta y_0$ (nm)
Silicon	40	42	30
	60	22	21
	80	19	17
Glass	40	18	17
	60	9	8
	80	6	5
PDMS	60	7	6
	80	5	4
	100	5	4

**Table A.1.:** Localization accuracy of tracked Au NPs in silicon-, glass- and PDMS-based GIE trapping devices.



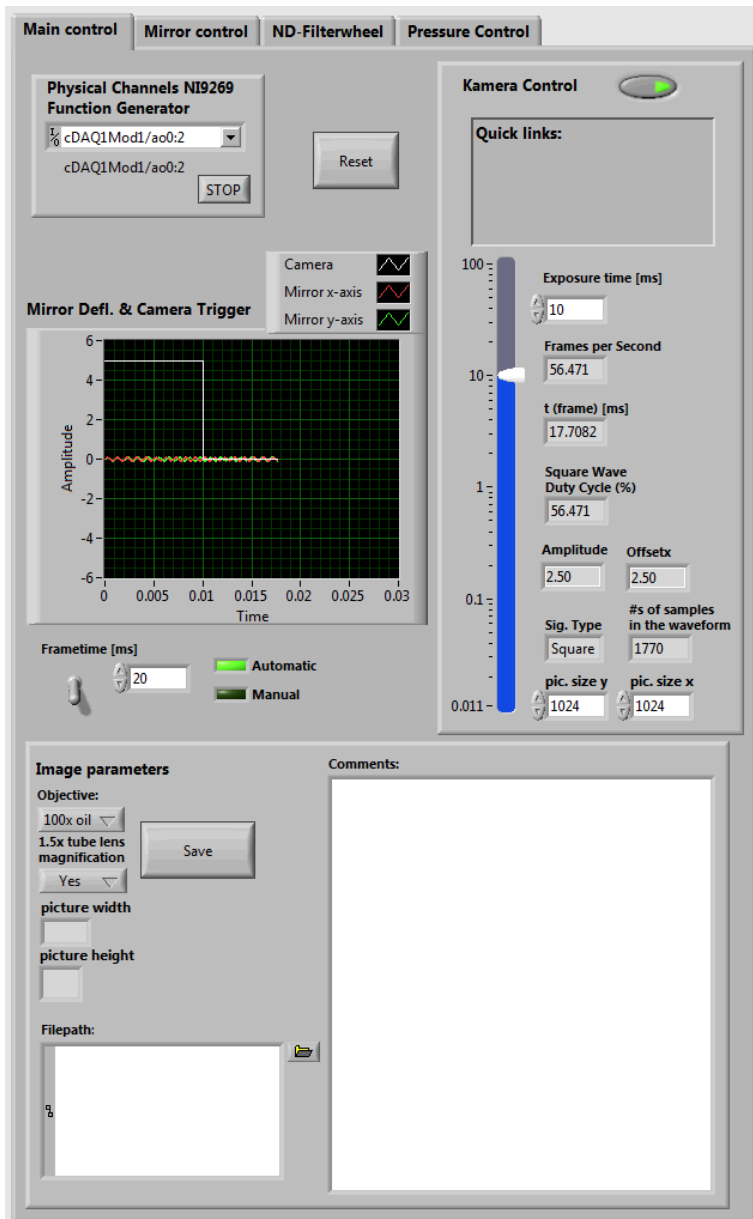


Figure A.2.: iSCAT software with the "Main control" window active



Figure A.3.: iSCAT software with the "Mirror control" window active

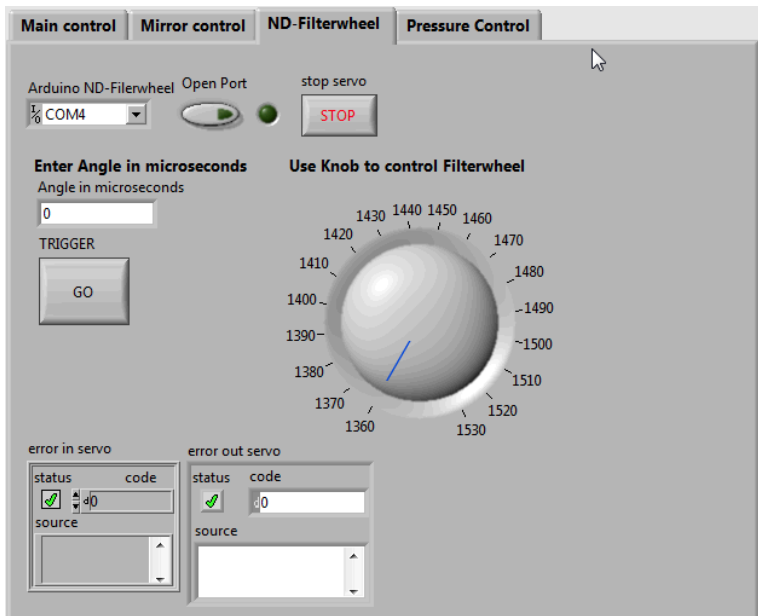


Figure A.4.: iSCAT software with the "ND-Filterwheel" window active

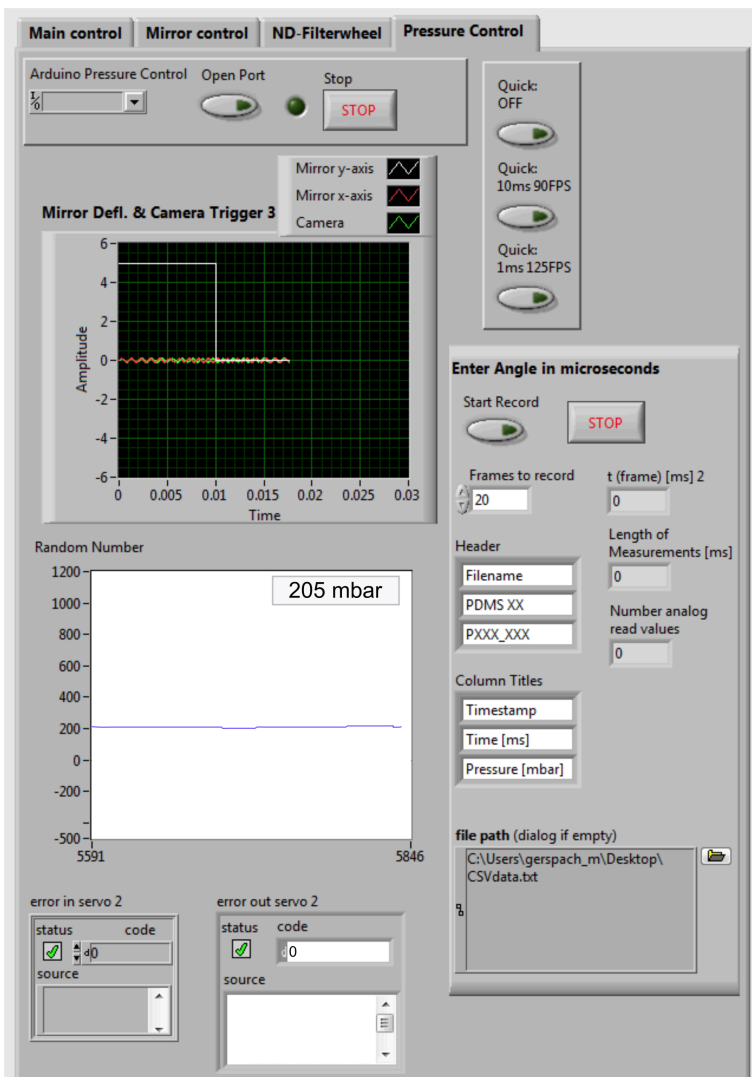


Figure A.5.: iSCAT software with the "Pressure control" window active



## Nanofabrication protocols

### B.1. Silicon wafer properties

- 100 mm diameter boron p-doped Si wafer, one side polished
- resistivity  $\sim 10 - 30 \Omega \text{ cm}$
- thickness  $525 \pm 25 \mu\text{m}$
- 400 nm thick thermally grown  $\text{SiO}_2$  top layer on polished side

### B.2. Glass wafer properties

- 100 mm diameter Borofloat<sup>®</sup> 33 glass wafer (Plan Optik AG)
- Expansion coefficient  $3.25 \times 10^{-6} \text{ K}^{-1}$  (adapted to silicon)
- thicknesses used:  $150 \pm 25 \mu\text{m} - 500 \pm 25 \mu\text{m}$

### B.3. Ormostamp glass wafer properties

- 100 mm diameter Borofloat<sup>®</sup> 33 glass wafer (Schott AG)
- thickness  $700 \mu\text{m}$

## B.4. Silicon device fabrication

### Supply microchannel fabrication – only for PDMS-based GIE trapping devices

1. Cleaning of wafer – first in IPA and second in DI water, dry under nitrogen stream
2. Evaporation of Cr layer – 120 nm, 0.1 nm/s (Univex 450, Leybold)
3. Spin-coating of UV resist – Microposit S1813, Shipley Company; 2000 rpm, 500 rpm/s, 40 s
4. UV exposure of microfluidic channels and alignment markers – Suess MA 6,  $\lambda = 365$  nm, 120 mJ/cm<sup>2</sup>, 12 s
5. Development – Megaposit MF-24A, Shipley Company for 40 s
6. Cr etching – BMP Plasmatechnology GmbH, O<sub>2</sub>:Cl<sub>2</sub> with a ratio of 5:1 for  $\sim 300$  s
7. SiO<sub>2</sub> RIE etching – 400 nm deep, Ar 38 sccm, CHF<sub>3</sub> 12 sccm, 100 W (Oxford 100)
8. Si RIE etching – 3  $\mu$ m deep, SF<sub>6</sub> 4 sccm, CHF<sub>3</sub> 30 sccm, O<sub>2</sub> 3 sccm, 100 W (Oxford 100)
9. Resist stripping and cleaning – piranha bath (H<sub>2</sub>SO<sub>4</sub>(%):H<sub>2</sub>O<sub>2</sub>(%) = 2:1) for 20 min at 90°C, cleaning in DI water, drying under nitrogen stream
10. Cr removal – Chrome ETCH No. 1, Technic, for 15 min
11. Cleaning of wafer – intensive cleaning in DI water and drying under nitrogen stream

### Nanofluidic channel fabrication

1. Evaporation of Cr layer – 25 nm, 0.1 nm/s (Univex 450, Leybold)
2. Spin-coating of e-beam resist – PMMA 950k, 4 % ethylacetate; 4000 rpm, 1000 rpm s<sup>-1</sup>, 60 s
3. E-beam exposure – Vistec EBPG 5000 Plus  
acceleration voltage: 100 kV  
dose: 800  $\mu$ C cm<sup>-1</sup>  
beam spot size: 129 nm  
beam current: 220 nA  
aperture: 400  $\mu$ m
4. Development – MIBK:IPA = 1:2 (v/v), 60 s
5. Cr etching – BMP Plasmatechnology GmbH, O<sub>2</sub>:Cl<sub>2</sub> with a ratio of 5:1 for  $\sim 60$  s
6. Channel height SiO<sub>2</sub> RIE etching – Ar 38 sccm, CHF<sub>3</sub> 12 sccm, 100 W (Oxford 100)
7. Resist stripping and cleaning – Acetone sonication for 10 min, cleaning

- in IPA and DI water, drying under nitrogen stream
8. Cr removal – Chrome ETCH No. 1, Technic, for 5 min
  9. Cleaning of wafer – intensive cleaning in DI water and drying under nitrogen stream

### **Nano-trap fabrication**

1. Evaporation of Cr layer – 20 nm, 0.1 nm/s (Univex 450, Leybold)
2. Spin-coating of e-beam resist – PMMA 950k, 4 % ethylacetate; 4000 rpm, 1000 rpm s<sup>-1</sup>, 60 s
3. E-beam exposure – Vistec EBPG 5000 Plus
  - acceleration voltage: 100 kV
  - dose: 850  $\mu\text{C cm}^{-1}$
  - beam spot size: 19 nm
  - beam current: 10 nA
  - aperture: 400  $\mu\text{m}$
4. Development – MIBK:IPA = 1:3 (v/v), 60 s
5. Cr etching – BMP Plasmatechnology GmbH, O<sub>2</sub>:Cl<sub>2</sub> with a ratio of 5:1 for ~ 50 s. It is essential to perform etching rate tests before etching the nano traps. Since BMP etching is isotropic, overetching will result in larger trap diameters.
6. Trap depth SiO<sub>2</sub> RIE etching – Ar 38 sccm, CHF<sub>3</sub> 12 sccm, 100 W (Oxford 100)
7. Resist stripping and cleaning – Acetone sonication for 10 min, cleaning in IPA and DI water, drying under nitrogen stream

### **Dicing into chips – only for Si-based GIE trapping devices**

1. Spin-coating of protection resist – Microposit S1813, Shipley Company; 3000 rpm, 500 rpm/s, 40 s
2. Dicing of the silicon master into chips
3. Cr removal – Chrome ETCH No. 1, Technic, for 5 min
4. Cleaning of chips – Acetone sonication for 10 min followed by a piranha bath (H<sub>2</sub>SO<sub>4</sub>(%):H<sub>2</sub>O<sub>2</sub>(%) = 2:1) for 20 min at 90°C, intensive cleaning in DI water, drying under nitrogen stream
5. Cleaning of Borofloat<sup>®</sup> 33 cover glasses with a thickness of 150  $\mu\text{m}$  – piranha bath (H<sub>2</sub>SO<sub>4</sub>(%):H<sub>2</sub>O<sub>2</sub>(%) = 2:1) for 20 min at 90°C, intensive cleaning in DI water, drying under nitrogen stream

### **Anodic bonding – only for Si-based GIE trapping devices**

Anodic bonding of the devices was accomplished at the BRNC-cleanroom facility at IBM Switzerland

- wafer bonder – SUSS MicroTech BA6/8
- bonding temperature: 450°C
- chamber pressure:  $5 \cdot 10^{-4}$  mBar
- bonding voltage: -600 V
- bonding force: 465 N
- bonding time: 10 min
- heat up/cool down: stepwise  $\sim 5^\circ\text{C}/\text{min}$

### **Silanization – only for PDMS-based GIE trapping devices**

1. Activation and cleaning of the wafer in an O<sub>2</sub> plasma – O<sub>2</sub> 20 sccm, 150 W (Oxford 80)
2. Silanization in an evacuation chamber – mixture of trichloro(1H, 1H, 2H 2H-perfluorooctyl)-silane and (tridecafluoro- 1,1,2,2-tetrahydrooctyl) di-methylchloro-silane with a ratio of 1:1 (v/v), 10 min



## B.5. Glass device fabrication

### Supply microchannel fabrication

The following steps are all particular crucial to achieve 10  $\mu\text{m}$  deep and high quality supply microchannels as seen in Fig. B.1B-C. Using thinner gold protection layers or removing the resist before BOE etching will result in cracks and unwanted etching in the nanofluidic areas as (Fig. B.1E).

1. Cleaning of glass Borofloat<sup>®</sup> 33 wafer with a thickness of 500  $\mu\text{m}$  – first in IPA and second in DI water, dry under nitrogen stream
2. Evaporation of Cr layer and Au layer on both wafer sides – Cr: 5 nm, 0.1 nm/s; Au: 150 nm, 0.1 nm/s; (Univex 450, Leybold)
3. Spin-coating of UV resist on both wafer sides – Microposit S1813, Shipley Company; 2000 rpm, 500 rpm/s, 40 s
4. UV exposure of microfluidic channels and alignment markers on one wafer side – Suess MA 6,  $\lambda = 365 \text{ nm}$ , 120  $\text{mJ}/\text{cm}^2$ , 12 s
5. Development – Microposit MF-24A, Shipley Company, for 40 s
6. Au etching – gold etchant (200 g KI + 50 g I, dissolved in 5 l DI water) for 45 s
7. Cr etching – chromium mask etchant (Chrome ETCH No 1, Technic) for 10 s
8. Glass etching – buffered oxide etch (BOE) bath (BOE 7:1, General Chemical Corporation) for 6 h to etch the structures 10  $\mu\text{m}$  deep into the glass wafer
9. Resist stripping and cleaning – piranha bath ( $\text{H}_2\text{SO}_4(\%)$ : $\text{H}_2\text{O}_2(\%) = 2:1$ ) for 20 min at 90°C, cleaning in DI water, drying under nitrogen stream
10. Au and Cr removal – first in gold etchant, subsequently in chromium etchant
11. Cleaning of wafer – intensive cleaning in DI water and drying under nitrogen stream

### Nanofluidic channel fabrication

1. Evaporation of Cr layer – 25 nm, 0.1 nm/s (Univex 450, Leybold)
2. Spin-coating of e-beam resist – PMMA 950k, 4 % ethylacetate; 4000 rpm, 1000  $\text{rpm s}^{-1}$ , 60 s
3. E-beam exposure – Vistec EBPG 5000 Plus  
 Acceleration voltage: 100 kV  
 Dose: 800  $\mu\text{C cm}^{-1}$   
 Beam spot size: 129 nm  
 Beam current: 220 nA  
 Aperture: 400  $\mu\text{m}$

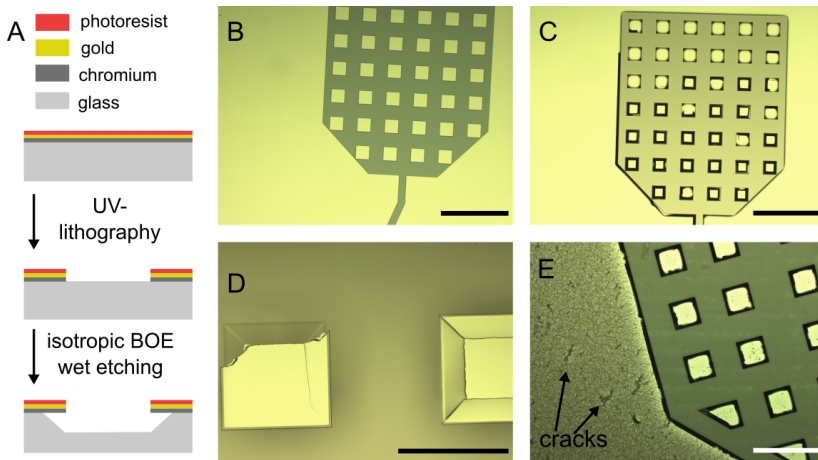


**Figure B.1.:** A) Sketch of UV-lithography and isotropic BOE wet-etching fabrication steps. B) Optical image of UV-exposed, developed and metal etched inlet and microfluidic channel structure before BOE etching, scale bar 1 mm. C) Optical image of structures etched into the glass wafer after 6 h BOE bath, scale bar 1 mm. D) Magnified image of C), highlighting the isotropic etching in the BOE bath, scale bar 200  $\mu\text{m}$ . E) Optical image after 2 h BOE etching using a only chromium and gold as a protection layer, scale bar 500  $\mu\text{m}$ .

4. Development – MIBK:IPA = 1:2 (v/v), 60 s
5. Cr etching – BMP Plasmatechnology GmbH,  $\text{O}_2:\text{Cl}_2$  with a ratio of 5:1 for  $\sim 60$  s
6. Channel height  $\text{SiO}_2$  RIE etching – Ar 38 sccm,  $\text{CHF}_3$  12 sccm, 100 W (Oxford 100)
7. Resist stripping and cleaning – Acetone sonication for 10 min, cleaning in IPA and DI water, drying under nitrogen stream
8. Cr removal – Chrome ETCH No. 1, Technic, for 5 min
9. Cleaning of wafer – intensive cleaning in DI water and drying under nitrogen stream

### Nano-trap fabrication

1. Evaporation of Cr layer – 20 nm, 0.1 nm/s (Univex 450, Leybold)
2. Spin-coating of e-beam resist – PMMA 950k, 4 % ethylacetate; 4000 rpm, 1000 rpm  $\text{s}^{-1}$ , 60 s
3. E-beam exposure – Vistec EBPG 5000 Plus  
 acceleration voltage: 100 kV  
 dose: 850  $\mu\text{C cm}^{-1}$   
 beam spot size: 19 nm

- beam current: 10 nA  
aperture: 400  $\mu\text{m}$
4. Development – MIBK:IPA = 1:3 (v/v), 60 s
  5. Cr etching – BMP Plasmatechnology GmbH,  $\text{O}_2:\text{Cl}_2$  with a ratio of 5:1 for  $\sim 50$  s
  6. Trap depth  $\text{SiO}_2$  RIE etching – Ar 38 sccm,  $\text{CHF}_3$  12 sccm, 100 W (Oxford 100)
  7. Resist stripping and cleaning – Acetone sonication for 10 min, cleaning in IPA and DI water, drying under nitrogen stream

### **Dicing and hole drilling – only for Glass-based GIE trapping devices**

1. Spin-coating of protection resist – Microposit S1813, Shipley Company; 3000 rpm, 500 rpm/s, 40 s
2. Dicing of the glass master into chips
3. Hole drilling for microfluidic inlets and outlets – 1 mm diameter diamond drill bit
4. Resist stripping – Acetone sonication for 10 min followed by intensive cleaning in DI water and drying under nitrogen stream
5. Cr removal – Chrome ETCH No. 1, Technic, for 5 min
6. Cleaning of chips – intensive cleaning in DI water, drying under nitrogen stream

### **Thermal bonding – only for glass-based GIE trapping devices**

The following steps are all particular crucial to achieve a high quality bonding. Shorter pressing or not pressing at all will result in bad quality bonding and leakage of the devices.

1. Cleaning of the chips and Borofloat<sup>®</sup> 33 cover glasses – piranha bath ( $\text{H}_2\text{SO}_4(\%):\text{H}_2\text{O}_2(\%) = 2:1$ ) for 20 min at  $90^\circ\text{C}$ , intensive cleaning in DI water, drying under nitrogen stream
2. Activation of the chips and Borofloat<sup>®</sup> 33 cover glasses – 29% ammonium hydroxide solution at  $35^\circ\text{C}$  for 40 min, intensive rinsing in DI water, drying under nitrogen stream
3. Alignment – instantly align and press one chip and one cover glass together with a tweezer
4. Pressing – Pressing of the aligned chip/cover glass multilayer with weights to reach a pressure of  $390 \text{ kN/m}^2$  for about 24 h
5. Thermal bonding – bonding in a controllable furnace (Process Products Corporation) without applying any pressure by annealing at  $630^\circ\text{C}$  for 4 h at the ramp rate and time cycle shown in Fig. 3.3C.

### **Silanization – only for PDMS-based GIE trapping devices**

1. Activation and cleaning of the wafer in an O<sub>2</sub> plasma – O<sub>2</sub> 20 sccm, 150 W (Oxford 80)
2. Silanization in an evacuation chamber – mixture of trichloro(1H, 1H, 2H 2H-perfluorooctyl)-silane and (tridecafluoro- 1,1,2,2-tetrahydrooctyl) di-methylchloro-silane with a ratio of 1:1 (v/v), 10 min

### **B.6. Ormostamp<sup>®</sup> fabrication**

1. Cleaning of the 700  $\mu\text{m}$  Borofloat<sup>®</sup> 33 glass wafer – rinsing in IPA and DI water, drying under nitrogen stream
2. Plasma activation of the 700  $\mu\text{m}$  Borofloat<sup>®</sup> 33 glass wafer – O<sub>2</sub> 20 sccm, 20 W (Oxford 80)
3. Spin-coating of adhesion layer on the 700  $\mu\text{m}$  Borofloat<sup>®</sup> 33 glass wafer – OrmoPrime<sup>®</sup> (micro resist technology GmbH), 4000 rpm, 45 sec
4. Ormostamp<sup>®</sup> molding – place a 2 ml droplet of OrmoStamp<sup>®</sup> hybrid polymer in the middle of a silanized silicon or glass wafer. Align the 700  $\mu\text{m}$  Borofloat<sup>®</sup> 33 glass wafer upside down onto the droplet and leave the multilayer for about 30 min.
5. Curing of the hybrid polymer – UV lamp (ELC-500, Electro-Lite) for 10 min
6. Hard bake – 30 min on a hotplate at 130°C.
7. Detaching – detach the two wafers using razor blades
8. Activation of the Ormostamp<sup>®</sup> wafer in an O<sub>2</sub> plasma – O<sub>2</sub> 20 sccm, 150 W (Oxford 80)
9. Silanization in an evacuation chamber – mixture of trichloro(1H, 1H, 2H 2H-perfluorooctyl)-silane and (tridecafluoro- 1,1,2,2-tetrahydrooctyl) di-methylchloro-silane with a ratio of 1:1 (v/v), 10 min

### **B.7. PDMS pneumatic silicon master fabrication**

1. Cleaning of silicon wafer – first in IPA and second in DI water, dry under nitrogen stream
2. Spin-coating of photoresist – 20  $\mu\text{m}$  thick, SU-8 2025, Microchem: first 500 rpm, 100 rpm/s, 10 s, second 4000 rpm, 300 rpm/s, 30 s
3. Soft bake – 6 min at 95°C
4. UV exposure – Suess MA 6,  $\lambda = 365 \text{ nm}$ , 200 mJ/cm<sup>2</sup>, 20 s
5. Post bake – 7 min at 95°C
6. Development – AZ EBR solvent (Clariant) for 6 min and subsequent cleaning in IPA
7. Hard bake – 25 min at 150°C

## Publications

### Peer-Reviewed Journal Publications

*Glass-based geometry-induced electrostatic trapping devices for improved scattering contrast imaging of nano-objects,*

M. A. Gerspach, N. Mojarad, T. Pfohl and Y. Ekinici, *Microelectronic Engineering* **145**, 01679317 (2015).

*Nanofluidic lab-on-a-chip trapping devices for screening electrostatics in concentration gradients,*

M. A. Gerspach, N. Mojarad, D. Sharma, T. Pfohl and Y. Ekinici, *Micro-electronic Engineering* **175**, 01679317 (2017).

*Single Positively Charged Particle Trapping in Nanofluidic Systems,*

D. Sharma, M. A. Gerspach, T. Pfohl, R. Y. H. Lim and Y. Ekinici, *Micro-electronic Engineering* **175**, 01679317 (2017).

*Soft electrostatic trapping in nanofluidics,*

M. A. Gerspach, N. Mojarad, D. Sharma, T. Pfohl and Y. Ekinici, accepted in *Microsystems & Nanoengineering*

*Pneumatic nanofluidic devices for controlled manipulation and contact-free trapping of nanoparticles,*

M. A. Gerspach, N. Mojarad, D. Sharma, Y. Ekinici and T. Pfohl, in preparation

## Annual Reports

*Nanofluidic devices for biomolecules,*

M. A. Gerspach, N. Mojarad, T. Pfohl and Y. Ekinici, SNI Annual Report 2013

*Nanofluidic trapping devices with increased trapping and detection performance,*

M. A. Gerspach, N. Mojarad, T. Pfohl and Y. Ekinici, SNI Annual Report 2014

*Nanofluidic trapping devices for detecting critical reaction concentrations of reactants,*

M. A. Gerspach, N. Mojarad, T. Pfohl and Y. Ekinici, SNI Annual Report 2015

*PDMS-based nanofluidic trapping devices for high-throughput fabrication and screening of nano-objects,*

M. A. Gerspach, N. Mojarad, T. Pfohl and Y. Ekinici, SNI Annual Report 2016

## Oral Contributions

*Towards nanofluidic devices for biomolecules,*

International Nanoscience Student Conference (INASCON) 2014, Middlefart, August 2014.

*High-throughput and passive trapping of nano-objects using electrostatic forces,*

SNI Annual Meeting, Lenzerheide, September 2014.

*High-throughput and passive trapping of nano-objects using electrostatic forces,*

SLS Symposium, Villigen, September 2014.

*High-throughput and passive trapping of nano-objects using electrostatic forces,*

DPG Spring Meeting, Berlin, March 2015.

*Nanofluidic trapping devices for detecting critical reaction concentrations of reactants on single nano-objects,*

NIS Winter School 2016, Zinal, January 2016.

*Nanofluidic trapping devices for detecting critical reaction concentrations of reactants on single nano-objects,*

MNE 2016, Vienna, September 2016.

---

*Highly flexible PDMS-based devices for high-throughput trapping of nano-objects,*

SNI Annual Meeting, Lenzerheide, September 2016.

*Nanofluidic trapping devices for detecting critical reaction concentrations,*  
SLS Symposium, Villigen, October 2016.

## Poster Contributions

*Towards trapping of biomolecules using nanofluidic devices,*

M. A. Gerspach, N. Mojarad, T. Pfohl and Y. Ekinici. NIS Winter School 2014, Kandersteg, January 2014.

*Towards trapping of biomolecules using nanofluidic devices,*

M. A. Gerspach, N. Mojarad, T. Pfohl and Y. Ekinici. Swiss NanoConvention, Neuchâtel, May 2014.

*Towards nanofluidic devices for biomolecules,*

M. A. Gerspach, N. Mojarad, T. Pfohl and Y. Ekinici. Swiss Soft Days 2014, Basel, June 2014.

*High throughput and passive trapping of nano-objects using electrostatic forces,*

M. A. Gerspach, N. Mojarad, T. Pfohl and Y. Ekinici. MNE Conference 2014, Lausanne, September 2014.

*Geometry-induced electrostatic trapping devices made from glass substrate for improved scattering contrast imaging of nano-objects,*

M. A. Gerspach, N. Mojarad, T. Pfohl and Y. Ekinici. NIS Winter School 2015, Belalp, January 2015.

*Geometry-induced electrostatic trapping devices made from glass substrate for improved scattering contrast imaging of nano-objects,*

M. A. Gerspach, N. Mojarad, T. Pfohl and Y. Ekinici. Swiss NanoConvention, Brugg, May 2015.

*Nanofluidic trapping devices for studying biomolecules and Brownian dynamics in confinement,*

M. A. Gerspach, N. Mojarad, T. Pfohl and Y. Ekinici. SNI Annual Meeting, Lenzerheide, September 2015.

*Nanofluidic trapping devices for detecting critical reaction concentrations,*

M. A. Gerspach, N. Mojarad, T. Pfohl and Y. Ekinici. Swiss NanoConvention, Basel, May 2016.

*Highly flexible PDMS-based devices for high-throughput trapping of nano-objects,*

M. A. Gerspach, N. Mojarad, T. Pfohl and Y. Ekinici. NIS Winter School 2017, Zermatt, January 2017.



*Every successful individual knows that his or her achievement depends on a community of persons working together.*

Paul Ryan

## **Acknowledgements**

This PhD thesis would have been not possible without the help, guidance and support from many scientists, technicians, colleagues, friends and my family. Hence, I would like to thank all, who contributed to this work.

First, I would like to express my sincere gratitude to my three PhD advisors and supervisors, Dr. Yasin Ekinci, Dr. Thomas Pfohl and Dr. Nassir Mojarad for giving me the opportunity to realize my PhD in their groups. They have guided me throughout this thesis with a never ending drive and enthusiasm for nanofabrication and nanofluidic science. I am thankful for the continuous support and that I could always discuss and ask my questions at any time, even at weekends. Further I am thankful for the trust and opportunity to present my scientific work at several meetings and various international conferences, which was a great experience for me. It has truly been a pleasure to work in the two groups and having you all as supervisors.

Especially I want to thank Yasin for his continuous support during my PhD studies and that his door was always open for us when we had a scientific or personal question. I admire his endless drive to write and publish new papers, which lead to a great amount of publications of this work. I also gratefully acknowledge that I could work on several small projects at the same time and for the given freedom to develop my own ideas. I am thankful that he shared his vast scientific expertise and new ideas on nanofabrication processes from which I could learn and benefit a lot. Further I especially admire his clear-sighted view on projects and his skill to immediately pinpoint to the critical problem. Finally I would like to thank Yasin for his trust that, beside my PhD work, I could organize two international conferences in London and Basel during my PhD, which was a great experience for me.

I especially like to thank Thomas for his strong support and guidance through all the projects during my PhD work, although I only spent one day a week in Basel. He fully integrated me into his group such that I could completely benefit from the vast knowledge and scientific expertise on nanofluidic devices and microscopy methods. Especially I acknowledge the Friday bilateral discussions, which resulted always in a great conclusion of the current week and new drive for the following Monday. I also thank him for his trust that I could lecture his chemistry lesson in front of 400 students which was a great experience for me. I am grateful for his endless, endless patient in test talks and his drive to advance our scientific presentations for perfection. I truly admire his persistence of great ideas, even if such an idea did not work out at all in first experiments. Only by his enthusiasm and motivation to find new solutions, some projects could be completed. But finally I would like to express my sincere gratitude to Thomas that, despite his working change in the last two year, he always still supported me strongly in all, scientific and personal matters.

I especially want to thank Nassir for his clear introduction, patient and supervising at the beginning of my PhD thesis. Although he has left PSI already two years ago, he still supported and guided me through this thesis at any time. Only by sharing his great expertise in the field of nanotrapping and optics, he enabled me to successfully start the project and tackle various challenging experiments. I thank him for all the patient and time he had, if I faced problems in the lab or cleanroom or if I had one of my thousand questions. I especially admire his great motivational skills. I left all meetings that I had with Nassir, even when the work stagnated, highly motivated and with new ideas to try in the lab, which always helped me to drive this work further. Finally I would like to thank him for all his great support on writing my publications and improve of my scientific writing. Thank you Nassir for being such a great supervisor and friend.

I am very grateful to Prof. Roderick Lim for being my examiner and the faculty representative of this thesis and to Dr. Thomas Braun for being the Co-Referee of this PhD thesis. I thank them for their commitment to read this thesis and to care about all administrative issues. Without them, my PhD would not have been accomplished.

I would like to thank Prof. Jens Gobrecht for giving me the opportunity to perform my PhD work at the Laboratory for Micro and Nanotechnology (LMN). Further, I strongly want to thank all the technicians and scientific staff at PSI, especially LMN. Without the help and support of Stefan Stutz, Eugen Deckardt, Konrad Vogelsang, Dario Marty, Thomas Neiger, Christopher Wild, Anja Weber, Jana Lehmann, Martin Bednarzik, Markus Kropf and Michaela

---

Vockenhuber this thesis would have been not possible. For all scientific input, critical questions and new ideas and suggestions I thank Vitalli Guzenko, Hans Sigg, Celestino Padeste and Victor Cadarso. Further I would like to thank Nachiappan Chidambaram for his help on imaging PDMS with SEM. I really enjoyed working at LMN. For me it is a unique place where people from very diverse topics work strongly together to drive scientific research in the nanoworld to the next level. The great teamwork and communication between the different groups makes LMN a working place where you always find an answer to a problem you are facing.

I am grateful to Roland German and Steffen Reidt from IBM Research Laboratory Zürich for giving me the possibility to work at the BRNC clean-room facility. Especially to Steffen Reidt, who helped and supported me to anodically bind my silicon chips to glass at the beginning of my thesis.

I also would like to thank all my colleagues at PSI and at the University of Basel for the friendly and always cooperative time we had together. At PSI I thank Elizabeth (Liz) Buitrago, Tero Kulmala, Roberto Fallica, Simon Tschupp, Patrick Helfenstein, Dimitrios Kazazis, Rajeev Rajendran, Iacopo Mochi, Mathias Dübner, Claire Donnelly, Dipanwita Dutta and Robert Kirchner. Particular I am grateful to all current and former villa mates with whom I could share the office (villa) every day and always had a lot of fun. Thank you Kristine Bedner, Deepika Sharma, Waiz Karim, Nadja Opara and Daniel Fan. I especially enjoyed my close friendship with Dan at work but even more outside of PSI. At the University of Basel I strongly want to thank Nora Sauter, Natalja Strelnikova, Michael Göllner, Raphael Urbani, Siddharth Deshpande, Axel Hochstetter und Cora-Ann Schönenberger. Although I only spend one day of the week in Basel, I always felt as a real member of the group. Thank you all for being such good friends and colleagues.

I would like to thank Claudia Wirth, Audrey Fischer and Edith Meisel for all the administrative and financial tasks during my PhD and all non-scientific questions I had. Particular I am very grateful to Claudia and Audrey for their help and guidance during the organization of the International Nanoscience Student Conference (INASCON) 2009 and 2015. Organizing these conferences were assuredly one of my greatest experience I had and I could learn and benefit a lot from your experiences.

Further, I am grateful to all members of the SNI. In particular to Prof. Christian Schönenberger for giving me the opportunity to be one of the first student in the new SNI PhD Graduate School and for his support and guidance during my nanoscience study during the last ten years. I thank him for all the great events that were organized for the SNI PhD students.

Additionally I thank Christian for his trust, guidance and financial support in the organization of the INASCON and that we could represent the SNI with these conferences. Further I would like to thank Michel Calame for organizing all the SNI PhD Graduate School events and conferences where we always learned a lot from a variety of research fields. Beside all the scientific work, joining a SNI event felt always like coming to a family event to meet, chat and have fun with friends and colleagues. A special thanks goes to Meret Hornstein, who unfortunately left the SNI during my PhD. I thank her for giving me the opportunity to perform outreach work on behalf of the SNI at TecDays in schools or at the Science Days in the Europa-Park. From her I learned, how to present my own, but as well others scientific work to a non-scientific community and young students and pupils.

Finally, I am greatly thankful to all people who reminded me that there still exists a life outside the lab. Here, I want to thank especially all my close friends who I certainly slighted in the last months. You all helped me to put my work aside, recover and to find new motivation and inspiration.

My deepest thanks and many love, however, go to my family and my girlfriend who supported me throughout the years and without whom I wouldn't be where I am today. Thank you mum and dad from the bottom of my heart for all your financial, but especially mental and physical support in all the years. You have enabled me so much and I could always count on you. Peter and Anne, my siblings, I am so proud on you being the best friends I can ever imagine. I thank you and your partners Emilia and Mischa for all the great time we have together and all the support you gave me during the last years. Especially I would like to thank you all for the huge support and to give me a moral uplift during the difficult time after 2008. Last but not least, I would like to express my deep sense of gratitude to my girlfriend Verena and her family. Being at my side now for eight years I thank you Verena from the bottom of my heart for your support, motivation and especially love. Although we have lived together for the last four years, the time we have spend together was little, certainly because of my commuting to PSI and your double load with your work and financial study. Nevertheless, I am truly thankful for your endless support and patient of all my night and weekend work shifts. Now it is on me, to give you all my support, energy, motivation, and love in the next months that you can finish your study successfully. I am looking very much forward to the wonderful time ahead of us.

# Curriculum Vitae

## Michael Adrian Gerspach

### Personal Information

Date of birth	October 5, 1986
Place of birth	Freiburg im Breisgau, Germany
Nationality	German
Hometown	Basel, BS, Switzerland

### Education

2012–present	<b>PhD Researcher – Nanosciences</b> Paul Scherrer Institut, Villigen, Switzerland University of Basel, Basel, Switzerland <b>Topic:</b> <i>Development of high-throughput nanofluidic trapping devices for detecting and screening of single nano-objects</i> Supervisors: Dr. Yasin Ekinici Dr. Thomas Pfohl Dr. Nassir Mojarad
03/2012–09/2012	<b>Master's thesis</b> , University College London (UCL), UK <b>Topic:</b> <i>Development of low-cost microfluidic chips to monitor HIV in resource-limited settings</i> Supervisor: Prof. Dr. Rachel McKendry, LCN, London, UK

- 10/2010–12/2012 **Master of Science in Nanosciences – Major in Physics**, University of Basel, Switzerland  
**Research topic I:** *Designed and built up a cell lysis system using microfluidic channels and ultrasound*  
Supervisor: Dr. Thomas Braun, C–CINA, Basel, Switzerland  
**Research topic II:** *Designed, fabricated and characterized silicon nanowire based ISFET sensors*  
Supervisor: Dr. Sebastian Gautsch, University of Lausanne, Neuchâtel, Switzerland
- 10/2006–09/2010 **Bachelor of Science – Major in Nanosciences**, University of Basel, Switzerland
- 09/2003–06/2006 **Abitur (high school diploma)**, Biotechnologisches Gymnasium, Lörrach, Germany
- 09/1997–08/2003 **High school**, Lise Meitner Gymnasium, Grenzach-Wyhlen, Germany

### Professional Experience

- 10/2013–03/2015 **Research and Teaching Assistant**, Chemistry Department, University of Basel
- 05/2008–10/2015 **Member of the organization committee “International Nanoscience Student Conference” (INASCON)**  
07/2014–10/2015 INASCON 2015, Basel, Switzerland  
05/2012–10/2013 INASCON 2013, London, UK  
05/2008–10/2009 INASCON 2009, Sursee, Switzerland
- 09/2004–02/2012 **Software supporter**, part-time 10%  
University of Basel, Basel, Switzerland  
Department of dental medicine, division PZMOM

### Scholarships and Awards

- 01/2015 **Best Poster Award**, Nanoscience in the Snow 2015, Belalp, Switzerland
- 02/2012 **Nanoscience Argovia Travel Grant**, Swiss Nanoscience Institute, University of Basel